Axonal Transport of Lysosomes and Its Relevance to Axonal Homeostasis in Niemann-Pick Disease Type C

Joseph Roney

A thesis presented for the degree of

Doctor of Philosophy



Nuffield Department of Medicine

Experimental Medicine Division

Lincoln College

University of Oxford

Abstract

Neurons face unique challenges in maintaining cellular homeostasis in axons far removed from the cell body where lysosomes are enriched. Niemann-Pick disease type C (NPC) is a neurodegenerative lysosomal storage disorder characterized by lipid accumulation in endolysosomes. An early pathologic hallmark of NPC is axonal dystrophy with bulbous swellings that contain accumulated organelles at presymptomatic stages prior to neuron loss in NPC mice. However, the mechanisms underlying these axonal pathologic changes remain obscure. Here, we demonstrate that organelles of the endocytic and autophagic pathways accumulate in NPC dystrophic axons. Using STED super-resolution and live-neuron imaging, we reveal that elevated cholesterol on NPC lysosome membranes in the soma leads to the sequestration of Arl8 and kinesin-1, resulting in impaired anterograde transport of mature degradative lysosomes to distal axons, contributing to axonal autophagosome accumulation. Pharmacologic reduction of lysosomal membrane cholesterol with 2-hydroxypropyl-β-cyclodextrin (HPCD) or elevated expression of Arl8b rescues lysosome transport into axons, thereby reducing axonal autophagic stress and neuron death in NPC. Collectively, these findings suggest a new pathological mechanism by which altered membrane lipid composition impairs lysosome delivery into axons of NPC neurons and provide biological insights into the translational application of HPCD in restoring axonal homeostasis at early stages of NPC disease.

Acknowledgements

I would like to thank my supervisors Fran Platt and Zu-Hang Sheng for their excellent mentorship and guidance throughout my time in the program. Thank you for always being so generous with your time and allowing me to grow both personally and professionally throughout this experience. I could not have asked for better mentors. I would also like to thank all members of the Sheng lab, with special thanks to Tamar Farfel-Becker and Xiu-Tang Cheng for their continued support, which would have made things a lot more difficult without it. I am also very grateful to all members of the Platt lab for making my time in Oxford such an enjoyable and rewarding experience that I will never forget. I would also like to thank the NIH OxCam Program and International Biomedical Research Alliance, with special thanks to Katie Stagliano and Randi Balletta for their strong support and advocacy for students in the program. Thank you also to the Intramural Research Program of the National Institute of Neurological Disorders and Stroke, NIH for funding this research. Finally, I am extremely grateful for my family and friends for their unwavering support, encouragement, and always being there for me.

TABLE OF CONTENTS

Abstract ii
Acknowledgements iii

LIST OF FIGURES VII
Chapter 1 vii
Chapter 2 vii
Chapter 3 viii
Chapter 4 ix
Chapter 5 ix

ABBREVIATIONS X

CHAPTER 1 – INTRODUCTION 1
1.1 – Lysosomal Storage Diseases 2
1.2 – Niemann-Pick Disease Type C 3
1.3 – *Npc1* Null Mouse Model 5
1.3.1 – Overview and Disease Progression 5
1.3.2 – Neuropathology 6
1.4 – Overview of the Lysosome 9
1.4.1 – Endocytic Pathway 11
1.4.2 – Autophagic Pathway 12
1.4.3 – Biosynthetic Pathway 12
1.4.4 – Phagocytic Pathway 14
1.5 – Lysosome Positioning and Motility 14
1.5.1 – Anterograde Transport 15
1.5.2 – Retrograde Transport 19
1.6 – Neuronal Lysosome Transport and Neurodegeneration 22
1.6.1 – Neuronal Lysosomes 23
1.6.2 – Dendritic Lysosome Transport 25
1.6.3 – Axonal Lysosome Transport 28
1.6.4 – Lysosome Dysfunction, Mistrafficking, and Axonal Dystrophy 33
1.7 – Hypothesis and Specific Aims 36

CHAPTER 2 – CHARACTERIZATION OF AXONAL ORGANELLE TRANSPORT AND DISTRIBUTION IN NPC 37
2.1 – Introduction 38
2.2 – Materials and Methods 40
2.2.1 – *Npc1* Mouse Model and Care 40
2.2.1.1 – *Npc1* Mouse Genotyping 41

2.2.1.2 – Agarose Gel Electrophoresis 42
2.2.2 – Antibodies and Probes 43
2.2.2.1 – Labeling Lysosomes with Activity-Based Lysosome Probes 43
2.2.2.1.1 – Active Glucocerebrosidase 43
2.2.2.1.2 – Active Cathepsin D 44
2.2.3 – Plasmids 44
2.2.3.1 – Cloning 44
2.2.3.1.1 – Cloning Strategy 44
2.2.3.1.2 – Generation of Insert 45
2.2.3.1.3 – Gel Extraction 46
2.2.3.1.4 – Restriction Digestion of Insert and Vector 47
2.2.3.1.5 – Ligation 48
2.2.3.1.6 – Bacterial Transformation 48
2.2.3.1.7 – Colony Screening 49
2.2.3.1.8 – Plasmid Sequencing 49
2.2.3.1.9 – Plasmid Purification 50
2.2.3.2 – Plasmids Table 51
2.2.4 – Western Blotting 51
2.2.4.1 – Protein Extraction 51
2.2.4.2 – SDS-PAGE 52
2.2.4.3 – Transfer 53
2.2.4.4 – Chemiluminescent Detection 53
2.2.4.5 – Membrane Stripping and Re-probing 54
2.2.4.6 – Densitometry Analysis 54
2.2.5 – Primary Neuronal Cultures 54
2.2.5.1 – Embryonic Cortical 54
2.2.5.2 – Adult Dorsal Root Ganglion 55
2.2.6 – Basic Neuron Nucleofection 55
2.2.7 – Microfluidic Device Preparation and Culture 56
2.2.8 – Immunostaining 57
2.2.9 – Transmission Electron Microscopy 57
2.2.10 – Image Acquisition and Analysis 58
2.2.11 – Live-neuron Imaging and Motility Analysis 58
2.2.12 – Statistical Analyses 59

2.3 – Results 60
2.3.1 – Axonal Autophagic Stress in *Npc1*$^{-/-}$ Mice at Presymptomatic Stages 60
2.3.2 – Reduced Lysosome Density in *Npc1*$^{-/-}$ Distal Axons 63
2.3.3 – Lysosomes Accumulate in Cell Bodies of *Npc1*$^{-/-}$ Cortical Neurons 68

2.4 – Discussion 72

CHAPTER 3 – MECHANISMS CONTRIBUTING TO IMPAIRED AXONAL LYSOSOME POSITIONING IN NPC 76

3.1 – Introduction 77

3.2 – Materials and Methods 80
3.2.1 – Lentivirus Production and Transduction 80
3.2.2 – Super-resolution STED Imaging 80
3.2.3 – Recombinant GST-D4H*-mCherry Protein Purification 81
3.2.4 – Detecting Luminal and Membrane Cholesterol with Filipin and D4H* 82
3.2.5 – Magnetic Isolation of Lysosomes 83

3.2.6 – Image Acquisition and Analysis 84

3.3 – Results 85
3.3.1 – Impaired Anterograde Transport and Delivery of Lysosomes to Distal Axons in *Npc1*$^{-/-}$ Cortical Neurons 85
3.3.2 – Aberrant Sequestration of Arl8 and kinesin-1 on *Npc1*$^{-/-}$ Lysosome Membranes 91
3.3.3 – Elevated Lysosomal Membrane Cholesterol Sequesters Kinesin-1 and Arl8 94

3.4 – Discussion 101

CHAPTER 4 – GENETIC AND PHARMACOLOGICAL RESCUE OF AXONAL LYSOSOME DELIVERY AND ITS IMPACT ON AXONAL HOMEOSTASIS IN NPC 105

4.1 – Introduction 106

4.2 – Materials and Methods 108
4.2.1 – siRNA Knockdown 108
4.2.2 – TUNEL Assay and Analysis 108
4.2.3 – Image Acquisition and Analysis 109

4.3 – Results 110
4.3.1 – Pharmacologic Rescue of Axonal Lysosome Delivery Reduces Autophagic Stress in *Npc1*$^{-/-}$ Neuronal Axons 110
4.3.2 – Elevated Expression of Kinesin-lysosome Adaptor Arl8b Facilitates Lysosome Transport into Axons and Reduces Axonal Autophagic Stress and Neuron Death in Presymptomatic *Npc1*$^{-/-}$ Neurons 116

4.4 – Discussion 122

CHAPTER 5 – DISCUSSION 124

5.1 – Concluding Remarks 125
5.1.1 – Coordinated Bidirectional Transport Maintains Axonal Homeostasis 126
5.1.2 – Altered Membrane Lipid Composition Impairs Lysosome Delivery to NPC Axons 128
5.1.3 – Lysosomal Dysfunction and Axonal Autophagic Stress in NPC Neurons 129

5.2 – Future Studies 130

APPENDICES 132

Appendix 1 133
Genotyping Primer Sequences 133
Cloning Primer Sequences 133
siRNA Oligonucleotide Sequences 133

Appendix 2 134
Primary Antibodies 134
Secondary Antibodies 135

PEER-REVIEWED PUBLICATIONS 136

REFERENCES 138

List of Figures

Chapter 1

Figure 1.1	Schematic diagram of the pathogenic cascade in LSDs
Figure 1.2	Schematic diagram of clinical features observed in NPC patients
Figure 1.3	Symptoms of disease progression in *Npc1*$^{-/-}$ mice
Figure 1.4	Axonal dystrophy in Purkinje neurons of the cerebellum in *Npc1*$^{-/-}$ mice at 4 weeks
Figure 1.5	Ultrastructural image of a dystrophic axon from the *Npc1*$^{-/-}$ feline model
Figure 1.6	Properties of lysosomes
Figure 1.7	Membrane trafficking routes to the lysosome
Figure 1.8	Schematic diagram of the BORC/Arl8/SKIP/Kinesin-1 complex for lysosome movement towards microtubule-plus ends
Figure 1.9	Schematic diagram of the Rab7/FYCO1/Kinesin-1 complex for lysosome movement towards microtubule-plus ends
Figure 1.10	Schematic diagram of the Rab7/RILP/ORP1L/Dynein-Dynactin complex for lysosome movement towards microtubule-minus ends
Figure 1.11	Schematic diagram of the TRPML1/ALG2/Dynein-Dynactin complex for lysosome movement towards microtubule-minus ends
Figure 1.12	Schematic diagram of the TMEM55B/JIP4/Dynein-Dynactin complex for lysosome movement towards microtubule-minus ends
Figure 1.13	Schematic diagram showing LAMP1/2 distributed among a heterogeneous population of endocytic and autophagic organelles in neurons
Figure 1.14	Schematic diagram of axonal lysosome maturation
Figure 1.15	Ultrastructural image of a dystrophic axon from a post-mortem cortex of a patient with Alzheimer's disease

Chapter 2

Figure 2.1	Schematic diagram showing lysosome labeling using activity-based lysosome probes
Figure 2.2	Axonal organelle accumulation in symptomatic *Npc1*$^{-/-}$ mice
Figure 2.3	Axonal autophagic stress in presymptomatic *Npc1*$^{-/-}$ mice

Figure 2.4	No change in autophagosome motility in presymptomatic *Npc1*$^{-/-}$ axons
Figure 2.5	Reduced density of endolysosomes and degradative lysosomes in DRG axons from presymptomatic *Npc1*$^{-/-}$ mice
Figure 2.6	Reduced density of endolysosomes and degradative lysosomes in axons from *Npc1*$^{-/-}$ cortical neurons
Figure 2.7	Lysosomes accumulate in cell bodies of *Npc1*$^{-/-}$ cortical neurons
Figure 2.8	No change in total lysosome protein levels in cultured *Npc1*$^{-/-}$ cortical neurons
Figure 2.9	Cholesterol storage in *Npc1*$^{-/-}$ cortical neurons
Figure 2.10	Schematic diagram showing altered lysosome distribution in axons of *Npc1*$^{-/-}$ neurons

Chapter 3

Figure 3.1	Schematic diagram of neuronal lysosome distribution
Figure 3.2	Schematic diagram of the Arl8-SKIP-kinesin-1 axonal lysosome transport complex
Figure 3.3	Schematic diagram of *in situ* cholesterol labeling assay
Figure 3.4	Schematic diagram of magnetic isolation of lysosomes
Figure 3.5	Schematic diagram of soma-restricted labeling of degradative lysosomes and their delivery to distal axons using a microfluidic device
Figure 3.6	Impaired lysosome delivery to distal axons in *Npc1*$^{-/-}$ neurons
Figure 3.7	Impaired anterograde lysosome transport in *Npc1*$^{-/-}$ distal axons
Figure 3.8	Altered axonal autophagosome density over time in *Npc1*$^{-/-}$ cortical neurons
Figure 3.9	No change in axonal autophagosome motility in DIV10 *Npc1*$^{-/-}$ cortical neurons
Figure 3.10	STED super-resolution imaging reveals aberrant sequestration of Arl8 and kinesin-1 on lysosome membranes in *Npc1*$^{-/-}$ neurons
Figure 3.11	Elevated cholesterol on lysosome membranes in *Npc1*$^{-/-}$ neurons
Figure 3.12	Pharmacologic treatment with 2-hydroxyproyl-β-cyclodextrin (HPCD) reduces cholesterol from lysosome membranes in *Npc1*$^{-/-}$ neurons
Figure 3.13	STED imaging reveals that reducing membrane cholesterol with HPCD releases sequestration of Arl8 and kinesin-1 from *Npc1*$^{-/-}$ lysosome membranes
Figure 3.14	Endolysosomal membrane isolations show that HPCD treatment releases sequestration of Arl8 and kinesin-1 from *Npc1*$^{-/-}$ lysosome membranes
Figure 3.15	Schematic diagram showing lipid-mediated sequestration of motor-adaptor proteins impairs axonal lysosome delivery in *Npc1*$^{-/-}$ neurons

Chapter 4

Figure 4.1	Schematic diagram of axonal autophagosome maturation coupled to their retrograde transport
Figure 4.2	Pharmacologic rescue of axonal lysosome distribution with HPCD in DRG neurons from presymptomatic *Npc1*$^{-/-}$ mice
Figure 4.3	HPCD treatment enhances axonal lysosome delivery in *Npc1*$^{-/-}$ neurons
Figure 4.4	Arl8 siRNA knockdown efficiency
Figure 4.5	Impaired axonal lysosome delivery induces autophagic stress in axons
Figure 4.6	HPCD treatment facilitates axonal autophagic flux in *Npc1*$^{-/-}$ neurons
Figure 4.7	Elevated expression of kinesin-lysosome adaptor Arl8b rescues axonal lysosome density in DRG neurons from presymptomatic *Npc1*$^{-/-}$ mice
Figure 4.8	Elevated Arl8b expression reduces lysosome accumulation in the soma of *Npc1*$^{-/-}$ neurons
Figure 4.9	Excessively high levels of Arl8b overexpression leads to organelle accumulation in *Npc1*$^{-/-}$ axons
Figure 4.10	Elevated expression of kinesin-lysosome adaptor Arl8b reduces axonal autophagic stress in DRG neurons from presymptomatic *Npc1*$^{-/-}$ mice
Figure 4.11	Elevated expression of kinesin-lysosome adaptor Arl8b rescues cell death in neurons from presymptomatic *Npc1*$^{-/-}$ mice

Chapter 5

Figure 5.1	Proposed model showing lipid-mediated sequestration of motor-adaptor proteins impairs axonal lysosome delivery, leading to autophagic stress in *Npc1*$^{-/-}$ axons

Abbreviations

AD: Alzheimer's disease
AIS: axon initial segment
ALG2: apoptosis-linked gene 2
ALS: amyotrophic lateral sclerosis
AMPA: alpha-amino-3-hydroxy-5-methyl-4-isoxazolepropionic acid
Arp1: actin-related protein 1
AV: autophagic vacuole
AVd: degradative autophagic vacuole
AVi: initial autophagic vacuole
BORC: BLOC-1-related complex
BSA: bovine serum albumin
CLEAR: coordinated lysosomal expression and regulation
CNS: central nervous system
CPT1C: carnitine palmitoyltransferase 1C
CTSD: cathepsin D
DIV: days *in vitro*
DLIC: dynein light intermediate chain
DRG: dorsal root ganglion
F-actin: filamentous actin
FTLD: frontotemporal lobar degeneration
FYCO1: FYVE- and coiled-coil-domain-containing protein
GCase: glucocerebrosidase
GEF: guanine nucleotide exchange factor
GPN: glycyl-L-phenylalanine 2-naphthylamide
HD: Huntington's disease
HPCD: 2-hydroxypropyl-β-cyclodextrin
HPLC: high performance liquid chromatography
JIP: JNK-interacting protein
KHC: kinesin heavy chain
KIF5: kinesin-1 family
KLC: kinesin light chain
KO: knockout
LAMP1: lysosome associated membrane protein 1
LAMP2: lysosome associated membrane protein 2
LSD: lysosomal storage disorder
M6PR: mannose 6-phosphate receptor
MHC: major histocompatibility complex
MLIV: Mucolipidosis type IV
MTOC: microtubule-organizing center
mTORC1: mechanistic target of rapamycin complex 1

MVB: multivesicular body
Ncr1: Niemann-Pick C related 1
NMDA: N-methyl-D-aspartate
NPC: Niemann-Pick disease type C
NPC1: Niemann-Pick Type C1
NPC2: Niemann-Pick Type C2
Nsg1: neuronal vesicle trafficking-associated protein 1
Nsg2: neuronal vesicle trafficking-associated protein 2
ORP1L: oxysterol-binding protein-related protein 1L
OSBP: oxysterol-binding protein
P30: post-natal day 30
P40: post-natal day 40
PtdIns3P: phosphatidylinositol 3-phosphate
RILP: Rab7-interacting lysosomal protein
SKIP: SifA and kinesin-interacting protein
SNARE: soluble NSF attachment protein receptor
STED: stimulated emission and depletion
TEM: transmission electron microscopy
TFE3: transcription factor E3
TFEB: transcription factor EB
TGN: *trans*-Golgi network
TRPML1: transient receptor potential mucolipin 1
TUNEL: terminal deoxynucleotidyl transferase dUTP nick end labeling
VAPA: vesicle-associated membrane protein-associated ER protein A
v-ATPase: vacuolar ATPase
WT: wild type

CHAPTER 1 – INTRODUCTION

1.1 – Lysosomal Storage Diseases

Lysosomal storage diseases (LSDs) comprise a group of over 70 monogenic disorders caused by mutations in genes critical for lysosome function (1-3). While most LSDs result from mutations in lysosomal enzymes, others are due to defects in lysosomal membrane proteins, non-enzymatic soluble lysosomal proteins, or enzyme activators (1, 4). The resulting cellular effect is the gradual accumulation of storage material within the lysosome, leading to altered lysosome function that triggers a complex pathogenic cascade and ultimately cell death (**Figure 1.1**) (5-7).

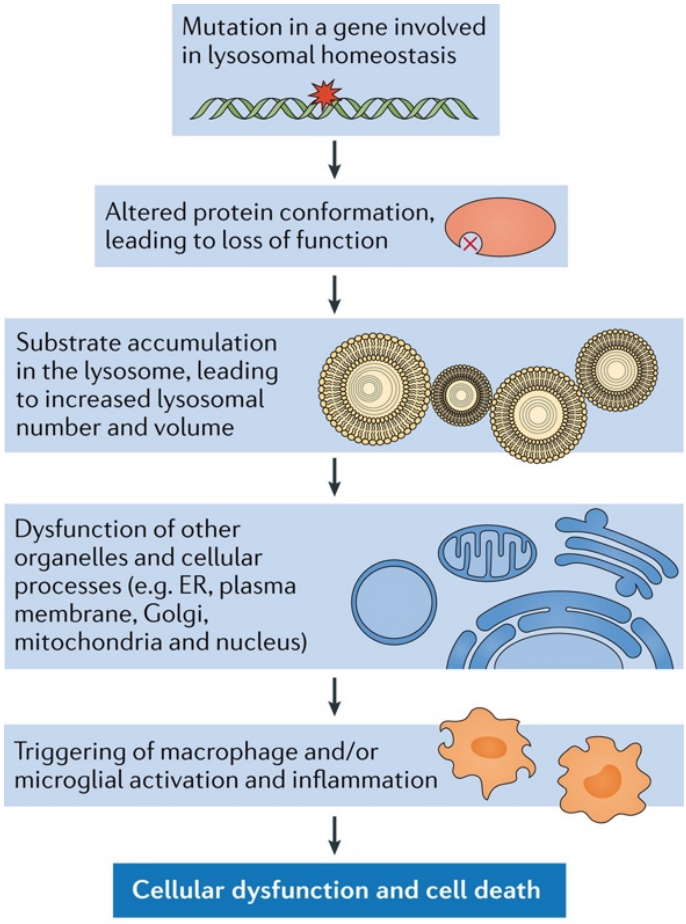


Figure 1.1 – Schematic diagram of the pathogenic cascade in LSDs. *Mutations in genes involved in lysosomal homeostasis cause LSDs. Depending on the mutation, this results in either no protein being expressed or the expression of mutant proteins with residual activity and function, leading to substrate accumulation within the lysosome.*

Primary lysosome dysfunction triggers dysfunction in other organelles, further disrupting cellular homeostasis. Together, these cascading events lead to progressive cellular dysfunction and cell death. Taken directly from Platt FM, 2018 (5).

While LSDs are individually rare, collectively they are estimated to have a combined incidence of around 1 in 5,000 live births (8, 9). Clinically, LSDs exhibit phenotypic heterogeneity with perinatal, late-infantile, juvenile, and adult-onset presentations (1, 10, 11). Progressive neurodegeneration is a common feature, but multiple organ systems are often affected (1, 12). Studies using cell and animal models have greatly advanced our understanding of LSD pathogenesis and helped reveal underlying pathogenic pathways and avenues for therapy (13-15). Defining the downstream cellular consequences of the primary defect that contribute to disease progression remains an active area of ongoing research (5, 16). Indeed, investigations into LSDs have uncovered new aspects of normal lysosome biology and function, and how dysfunction contributes to both rare and common neurodegenerative diseases.

1.2 – Niemann-Pick Disease Type C

Niemann-Pick disease type C (NPC; OMIM #257220) is a lysosomal storage disorder characterized by the accumulation of sphingosine, glycosphingolipids, sphingomyelin, and cholesterol in late endosomes and lysosomes (17, 18). The estimated incidence of NPC is around 1 in 120,000 live births (19) but may be more prevalent (20). NPC patients present clinically at variable ages with heterogeneous systemic involvement and progressive neurodegeneration leading to premature death (**Figure 1.2**) (10, 19, 21). Neurologic features define disease severity and commonly include motor dysfunction, developmental delay, and cognitive decline (10, 21). NPC has an autosomal recessive mode of inheritance with approximately 95% of cases caused by

mutations in *NPC1* (22, 23) and the remainder due to mutations in *NPC2* (24), though the two forms are clinically indistinguishable (10, 21).

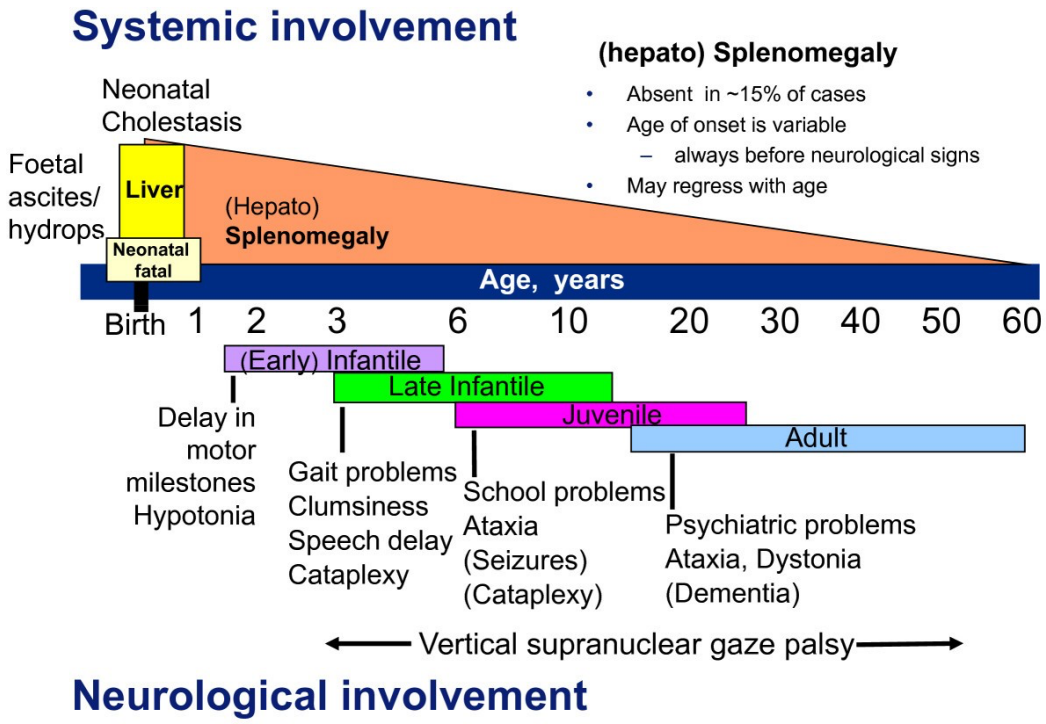


Figure 1.2 – Schematic diagram of clinical features observed in NPC patients. *NPC patients show remarkable clinical heterogeneity. Note that the age of onset of neurological symptoms designates disease groups and correlates with lifespan. Taken directly from Vanier MT, 2010 (10).*

NPC1 maps to chromosome 18q11-12 and encodes a 1278 amino acid protein (22, 25) that localizes to the lysosome membrane (26, 27), while *NPC2* maps to chromosome 14q24.3 and encodes a 132 amino acid protein that localizes to the lysosomal lumen (24). Because both NPC1 and NPC2 bind cholesterol, it has been suggested that they may act cooperatively to facilitate lysosomal cholesterol egress (28). In addition, given that NPC1 shows homology to bacterial proteins belonging to the RND permease family, it has also been suggested that NPC1 may function as a multiple substrate

transporter out of the lysosome (29, 30), consistent with the complex pattern of storage observed in NPC1-deficient lysosomes.

Notably, sphingosine was found to be the first metabolite to accumulate inside the lysosome following application of U18666A (31), a pharmacologic inhibitor of NPC1 (32). This increase in lysosomal sphingosine triggered a decrease in lysosomal calcium, leading to altered sphingolipid trafficking and secondary accumulation of cholesterol, sphingomyelin, and glycosphingolipids (31). Given that lysosomes function as calcium stores and signaling centers (33-35), this decrease in lysosomal calcium and reduced calcium release alters endolysosomal trafficking and fusion events in NPC (31, 36). NPC1-deficient cells show reduced rates of lysosomal fusion (31, 36, 37), while NPC2-deficient cells show defects in lysosomal fission required for the reformation of lysosomes (36). Elevating cytosolic calcium with calcium-modulating agents corrected NPC1-associated cellular phenotypes and improved function and lifespan in a mouse model of NPC disease, highlighting the importance of lysosomal calcium signaling to cellular homoestasis in NPC (31).

1.3 – *Npc1* Null Mouse Model

1.3.1 – Overview and Disease Progression

The *Npc1* null (*Npc1*$^{-/-}$) mouse represents a widely used animal model to study human NPC disease. This mouse model arose spontaneously with homozygous nonsense mutations in *Npc1*, resulting in a significant reduction in *Npc1* mRNA levels and absence of Npc1 protein expression (23). *Npc1*$^{-/-}$ mice model acute forms of NPC disease and recapitulate many biochemical, pathological, and neurological features (38-41). The lifespan of *Npc1*$^{-/-}$ mice ranges between 10-12 weeks, where their disease

progression can be divided into presymptomatic (3-4 weeks), symptomatic (6-7 weeks), and late symptomatic (9-10 weeks) stages (**Figure 1.3**) (42). Starting at around 6 weeks, *Npc1*$^{-/-}$ mice develop symptoms, which include a tremor and ataxic gait. At around 7-8 weeks, loss of coordination becomes more apparent, and *Npc1*$^{-/-}$ mice reach their maximum weight. At 9-12 weeks, *Npc1*$^{-/-}$ mice approach their humane end point as behavioral symptoms worsen, making feeding and drinking difficult, leading to severe weight loss (42).

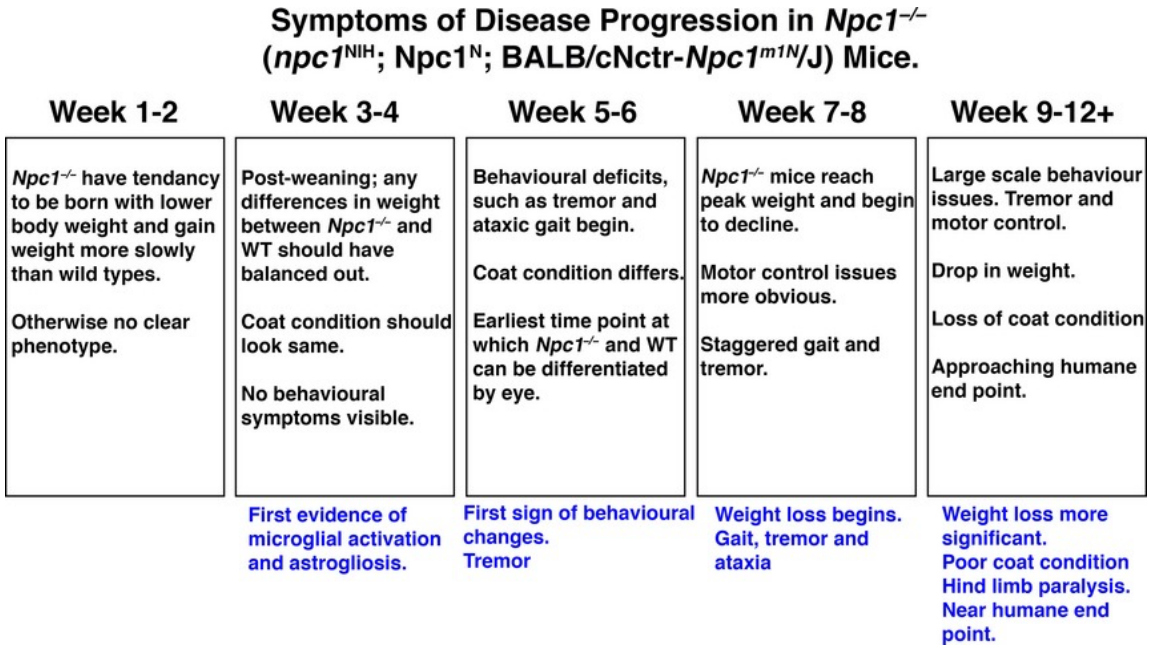


Figure 1.3 – Symptoms of disease progression in Npc1*$^{-/-}$ *mice. *Disease manifestations occur at defined ages in Npc1*$^{-/-}$ *mice, which can be divided into presymptomatic (3-4 weeks), symptomatic (6-7 weeks), and late symptomatic (9-10 weeks) stages. Taken directly from Platt N et al., 2016 (42).*

1.3.2 – Neuropathology

Approximately 70% of LSDs affect the brain, highlighting the importance of the lysosomal system to nervous system health (5). LSDs including NPC commonly show a specific spatial and temporal pattern of early neuropathology, which occurs before

global neurodegeneration in multiple brain regions (3, 43). These unique, region-specific changes are thought to be due in part to the dependence of certain neuronal populations on stored metabolite(s), the varying degrees of specific macromolecule syntheses among neuronal subtypes, and/or a differential neuronal vulnerability to storage (3).

In NPC patients, neuropathological abnormalities include widespread neuronal lipid storage, reactive gliosis, neuroinflammation, axonal dystrophy, and neurodegeneration, most notably in Purkinje cells of the cerebellum (39). In *Npc1*$^{-/-}$ mice, neuronal storage, axonal spheroids, and neurodegeneration are also major neuropathological features (39, 44, 45). Sensory thalamic pathways are particularly vulnerable, with early activation of astrocytes and microglia as well as the presence of aggregated presynaptic markers located within axonal spheroids in white matter tracks (43). Biochemical analyses of the brain revealed significant accumulation of GM2 and GM3 gangliosides as well as several neutral glycolipids including glucosylceramide and lactosylceramide (46, 47). Intraneuronal storage was most apparent in pyramidal neurons, Purkinje cells, and neurons of the thalamus and brain stem (39). Interestingly, total cholesterol levels in the brain were not changed but rather found to be redistributed to the cell body with a corresponding reduction in distal axons (48).

Axonal dystrophy is one major pathological feature observed in several LSDs including NPC, which is characterized by the formation of bulbous swellings along axons that contain membranous organelles (44, 45). Because the incidence and distribution of these axonal alterations (termed axonal spheroids) correlates closely with neurological symptoms and severity, it is thought that they may actively contribute to neuronal dysfunction (44, 49). In *Npc1*$^{-/-}$ mice, axonal spheroids appear early before the onset of

symptoms and gradually increase in size and number with disease progression (49, 50). Dystrophic axons occur in multiple regions of the nervous system including axonal processes of the substantia nigra and dorsal root ganglia, and are especially evident in cerebellar Purkinje cells (**Figure 1.4**) (44).

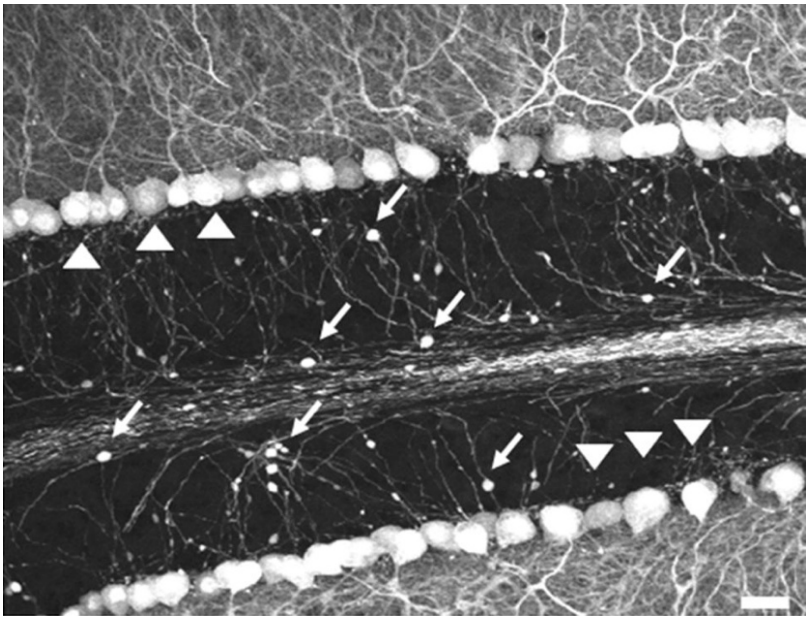


Figure 1.4 – Axonal dystrophy in Purkinje neurons of the cerebellum in Npc1$^{-/-}$ mice at 4 weeks. *Confocal image from transgenic Npc1$^{-/-}$ mice with L7 promoter-driven GFP expression to enable visualization of GFP-labeled neuronal morphology. Note the presence of many bulbous swellings in Purkinje cell axons (arrows). While axonal spheroids are readily observed, Purkinje cells are still abundant (arrowheads). Purkinje cell death does not occur until around 6 weeks in Npc1$^{-/-}$ mice. Cropped image taken directly from Walkley SU et al., 2010 (44).*

Ultrastructural examination of axonal swelling pathology demonstrated that they contain heterogenous collections of membranous organelle profiles and tubulovesicular elements related to the endo-lysosomal-autophagic pathways (**Figure 1.5**) (39, 44, 51). Interestingly, among several LSDs, the organelles that accumulate within dystrophic axons are ultrastructurally distinct from the lysosome inclusions observed in the neuronal cell body, which are often representative of a specific lysosomal storage class

(44). Instead, these accumulated axonal organelles resemble each other, suggesting they may result from or converge on a common cellular defect that lead to impairments in axonal transport and the removal of these organelles from axons (39, 44).

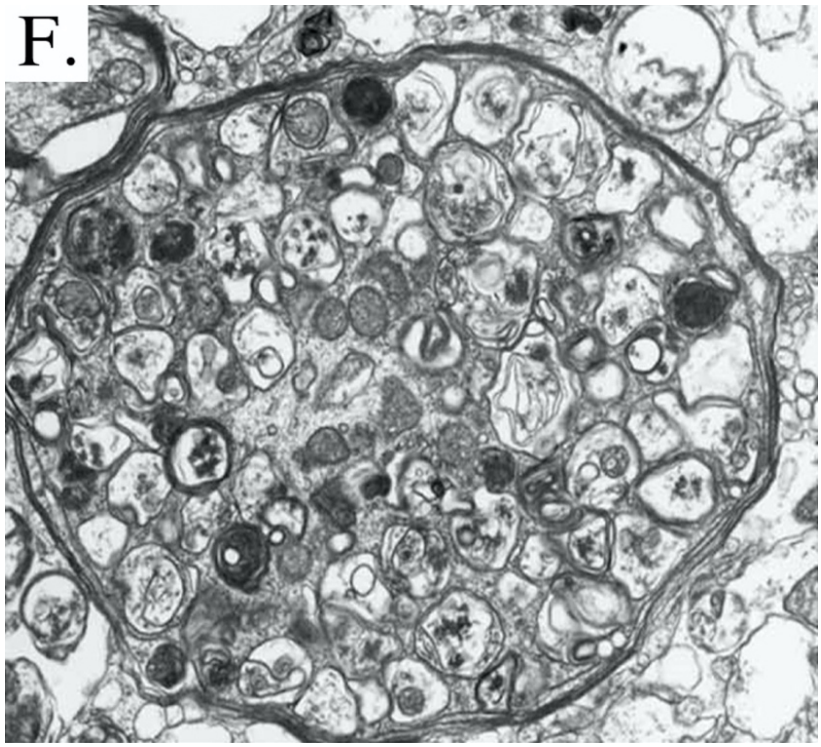


Figure 1.5 – Ultrastructural image of a dystrophic axon from the Npc1$^{-/-}$ feline model. *Note the heterogenous accumulation of endo-lysosomal-autophagic cargo within axonal swellings. Cropped image taken directly from Boland B and Platt FM, 2015 (51).*

1.4 – Overview of the Lysosome

Lysosomes are dynamic, membrane-bound, acidic organelles that play a central role in the degradation of intracellular and extracellular cargo. They contain more than 60 hydrolytic enzymes that facilitate breakdown of complex biological macromolecules, which include nucleic acids, proteins, lipids, and carbohydrates (52, 53). This degradative process generates small metabolites that are re-utilized by the cell as they feed into various metabolic and biosynthetic pathways. In addition, lysosomes contain

more than 200 integral membrane proteins with diverse and cooperative functions, which include vacuolar ATPases (v-ATPases) and ion channels that help maintain an acidic pH for optimal hydrolase activity, permeases that mediate transfer of molecules across the lysosome membrane, glycosylated lysosome associated membrane proteins (LAMPs) that protect the membrane from degradation, and soluble NSF attachment protein receptors (SNAREs) that promote membrane contact and fusion events (**Figure 1.6**) (54).

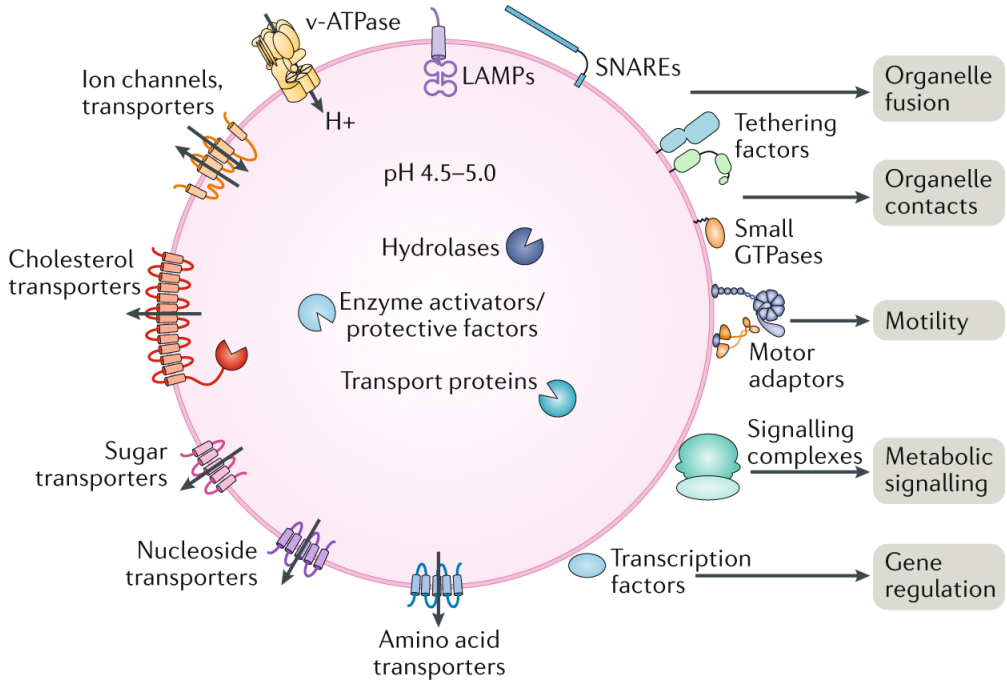


Figure 1.6 – Properties of lysosomes. *Lysosomes are composed of both luminal and integral membrane proteins. Note that protein complexes also assemble on the lysosome membrane to support critical lysosome functions including organelle fusion and contact, motility, metabolic signaling, and gene regulation. Taken directly from Ballabio A and Bonifacino JS, 2020 (54).*

Lysosomes receive and degrade macromolecules from multiple membrane trafficking routes including the endocytic, autophagic, biosynthetic, and phagocytic pathways (**Figure 1.7**) (55).

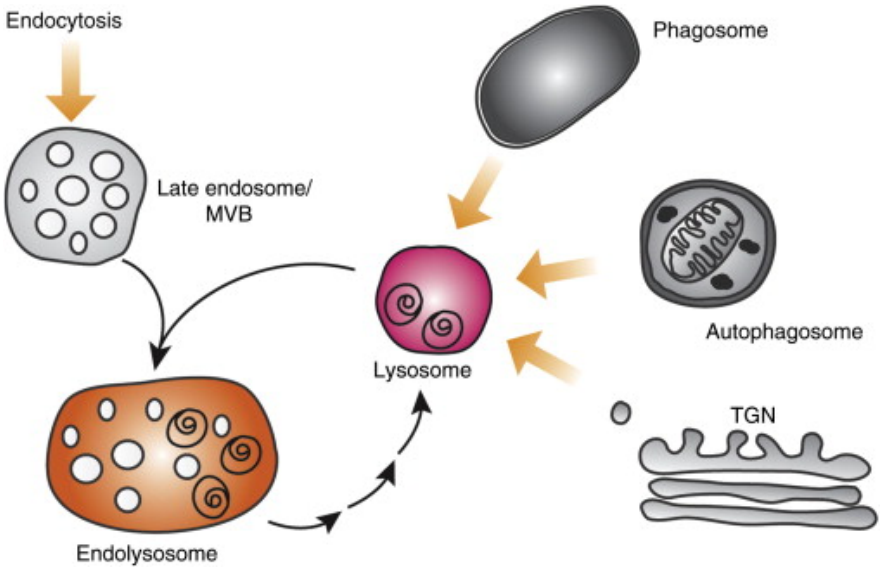


Figure 1.7 – Membrane trafficking routes to the lysosome. *Lysosomes serve as terminal degradation hubs for endocytic, autophagic, and phagocytic cargo. Newly synthesized lysosomal proteins are delivered from the trans-Golgi network (TGN) to endosomes and lysosomes through the biosynthetic route (not shown in detail). Lysosomes fuse with late endosomes/multivesicular bodies (MVBs) to form endolysosomes, the principal site of hydrolase activity and where lysosomes can be reformed (56). Taken directly from Wartosh L et al., 2015 (55).*

1.4.1 – Endocytic Pathway

Extracellular materials internalized by endocytosis at the plasma membrane are delivered to the lysosome through the endocytic pathway. Once endocytosed, cargos first transit through the early endosome, which serves as a sorting station where cargos either recycle back to the plasma membrane or continue to the lysosome for degradation (57-59). In their journey to the lysosome, endocytosed cargos continually transition between a range of endosomal intermediates involving multiple transient and complete fusion events (60-65). This process enables cargo delivery to lysosomal hydrolases, which entails transitioning between early endosomes to late endosomes and finally to lysosomes for cargo degradation (60, 61). Endocytosed cargos destined for clearance by the lysosome are progressively sorted into intraluminal vesicles as they

mature into multivesicular bodies/late endosomes (61, 66). Late endosomes are distinguished from early endosomes in part due to their low levels of endocytosed recycling cargos and elevated levels of newly synthesized lysosomal proteins from the *trans*-Golgi network (TGN) (61, 66). In addition, the transition from early to late endosomes is marked by replacement of the small GTPase Rab5 with Rab7, mediated by guanine nucleotide exchange factors (GEFs) (67, 68). Transient and direct fusion events between late endosomes and lysosomes create hybrid organelles called endolysosomes, which contain active lysosomal hydrolases for substrate degradation (56).

1.4.2 – Autophagic Pathway

Intracellular components targeted for degradation are delivered to the lysosome through the autophagic pathway. Autophagy is a quality control process that removes damaged organelles and aggregated proteins from the cell (69, 70). In delivering autophagic cargos to the lysosome for degradation, a stepwise maturation process occurs. Intracellular materials are sequestered within double-membrane organelles called autophagosomes, which subsequently fuse with late endosomes to form hybrid organelles called amphisomes or directly with lysosomes to form autolysosomes (71, 72). This dynamic process (termed autophagic flux) results in an equilibrium between autophagosome formation and clearance by the lysosome (73).

1.4.3 – Biosynthetic Pathway

Lysosomal hydrolases and integral membrane proteins traffic to the lysosome through the biosynthetic pathway. The biogenesis of many lysosomal proteins is under the

transcriptional control of transcription factors EB (TFEB) and E3 (TFE3), which can be activated under conditions of lysosomal stress (74, 75). Newly synthesized lysosomal proteins are delivered to the lysosome via multiple, highly regulated, complex routes within the biosynthetic pathway (60-62, 76, 77).

Most lysosomal hydrolase precursors are synthesized in the ER, then transported through the Golgi complex, where they acquire M6PR tags (60-62, 77). Once at the TGN, hydrolase precursors are recruited by their M6PR into TGN-derived clathrin-coated vesicles, which are then carried to endosomes (61). Following entry into endolysosomal compartments with acidic pH, lysosomal hydrolase precursors dissociate from their M6PR tags, and further modifications in late endosomes and lysosomes lead to hydrolase enzyme activation (61, 62). In addition, M6PR-independent routes for lysosomal hydrolase targeting have also been described, mediated by sortilin or the lysosomal integral membrane protein LIMP2 (78, 79). In the absence of a functional M6PR pathway, lysosomal hydrolase precursors may also enter the secretory pathway and be re-uptaked into the cell via mannose receptor-mediated endocytosis, then subsequently trafficked to the lysosome through the endocytic pathway (61, 80).

For lysosomal membrane proteins, lysosomal targeting occurs via direct or indirect routes (61, 62, 76, 81). In the direct route, membrane proteins containing a targeting sequence motif are recruited at varying steps within the TGN into clathrin-coated vesicles for direct delivery into the endocytic pathway. However, in the indirect route, lysosome membrane proteins enter the secretory pathway, then reach the lysosome via endocytic membrane trafficking.

1.4.4 – Phagocytic Pathway

Internalized particles (such as bacteria and apoptotic cells) target to the lysosome through the phagocytic pathway. Once internalized at the plasma membrane, pathogen-containing phagosomes mature through crosstalk with the endocytic pathway (82, 83). Following multiple transient and complete fusion events, a hybrid organelle called a phagolysosome is formed to facilitate phagosome clearance (82). Degradation of ingested particles results in the formation of antigenic peptides that are presented on major histocompatibility complex (MHC) class II molecules (83, 84). These peptide-loaded MHC-II complexes are transported via tubular lysosomes to the cell surface for antigen presentation to potentially elicit an immune resposne (85-88). In addition, endolysosomes positioned at the plasma membrane were recently discovered to serve as initiators of a phagocytosis signaling cascade that is activated upon pathogen recognition, revealing an upstream role for lysosomes in promoting phagocytosis and pathogen clearance (89).

1.5 – Lysosome Positioning and Motility

To efficiently coordinate events throughout the cell, lysosomes move as a function of regulated transport mechanisms (90). They transport along cytoskeletal tracks (91) through the activities of motor proteins (92, 93), which hydrolyze ATP to generate the force necessary to propel movement (94). Microtubule-based kinesin and dynein motors drive long-distance lysosome transport between the centrally located microtubule-organizing center (MTOC) and periphery of the cell. In general, lysosomes couple to motor proteins through interactions with adaptor proteins that enable recruitment and assembly of transport machineries at the lysosomal surface (95).

These adaptor proteins regulate cargo-specific transport and include small GTPases and their effectors as well as phospholipids (90).

Lysosome positioning throughout the cytoplasm changes in response to various cellular and environmental conditions, including the nutrient status of the cell. The mechanistic target of rapamycin complex 1 (mTORC1) is a protein kinase that regulates cellular metabolism and is recruited to the lysosomal surface upon activation by amino acids (96, 97). Redistributing lysosomes to the cell periphery correlates with increased mTORC1 activity, whereas collapsing lysosomes to the cell center has been shown to correlate with reduced mTORC1 activity (98). This distribution pattern is thought to be attributed to the proximity of peripheral lysosomes to upstream activators of mTORC1, and to facilitate autophagosome-lysosome fusion for perinuclear lysosomes located at the cell center, driven by changes in cytoplasmic pH (98, 99). Interestingly, the pH within the lysosomal lumen has also been shown to correlate with its cellular location, where peripheral lysosomes are less acidic than centrally-localized lysosomes (100). This is thought to be due in part to the location of perinuclear lysosomes closer to the biosynthetic pathway and therefore preferentially receive newly synthesized proteins as well as the balance between effectors of lysosome transport (100). Indeed, the subcellular distribution of lysosomes is regulated through anterograde and retrograde transport mechanisms to efficiently coordinate events throughout the cell.

1.5.1 – Anterograde Transport

The kinesin superfamily is composed of at least 45 genes grouped into 15 families, designated as kinesin-1 to kinesin-14B (101, 102). In general, kinesin motor proteins contain a motor domain that attaches to microtubules and a tail domain that interacts

directly with cargos or their adaptors to mediate cargo loading (103). Most kinesin superfamily proteins (KIFs) transport organelles toward microtubule-plus ends to facilitate anterograde movement, with the exception of kinesin-14 members (104).

Members of the kinesin-1 family have been well-characterized in their role in facilitating anterograde lysosome transport. Kinesin-1 is a heterotetrametric protein composed of two kinesin heavy chains (KIF5) and two kinesin light chains (KLCs). The motor domain of KIF5 is located at its N-terminus, whereas its C-terminus interacts with KLCs or directly with specific cargos or their adaptors (104). Mammals express three different KIF5 isoforms, denoted as KIF5A, KIF5B, and KIF5C. While KIF5B is expressed in most cell types, KIF5A and KIFC show neuron-specific expression (105).

Kinesin-1 loading onto endolysosome membranes depends on a series of interactions between the octameric BLOC-1-related complex (BORC), Arf-like small GTPase Arl8, and SifA and kinesin-interacting protein (SKIP) (**Figure 1.8**) (106). Myristoylation of the myrlysin subunit of BORC in part triggers its association with lysosome membranes, which is required for recruitment of Arl8 from the cytoplasm (106). SKIP then interacts with both Arl8 and KLC, linking endolysosomal organelles to kinesin-1 motors (107). Overexpression of either Arl8 or SKIP leads to the accumulation of lysosomes in the cell periphery (107), and this process was revealed to be BORC-dependent, as no such effects were observed in myrlysin KO cells (106). Knockdown of multiple BORC subunits results in juxtanuclear lysosome clustering without noticeably affecting the distribution of other organelles such as mitochondria and the ER, suggesting that BORC specifically regulates the distribution of lysosomes throughout the cytoplasm (106). In addition, SKIP only binds Arl8 in its active GTP-bound form, and knockdown of either Arl8 or SKIP prevents the peripheral lysosome accumulation induced by

overexpression of the other, suggesting they act together to promote plus-end directed lysosome motility (107).

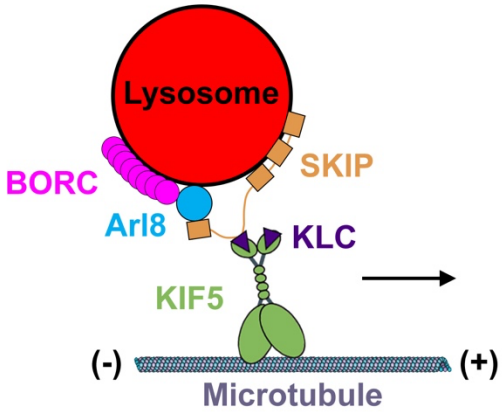


Figure 1.8 – Schematic diagram of the BORC/Arl8/SKIP/Kinesin-1 complex for lysosome movement towards microtubule-plus ends. *Model adapted from Rosa-Ferreira C and Munro S, 2011 (107) and Pu J et al., 2015 (106).*

Interestingly, the interaction between BORC and Arl8 was shown to depend on the nutrient status of the cell, representing a mechanism that integrates lysosome metabolic signaling with a coordinated response in lysosome positioning (108, 109). The amino acid sensing Ragulator complex inhibits BORC through binding of LAMTOR2 to lyspersin, and this interaction is strengthened by amino acid depletion. This enhanced interaction impairs kinesin recruitment to lysosome membranes, leading to reduced anterograde transport and juxtanuclear lysosome clustering in an mTOR-independent manner. However, under nutrient-replete conditions, the association between Ragulator and BORC is weakened, thereby promoting BORC- and Arl8-dependent lysosome movement towards the periphery of the cell (108, 109).

In addition, kinesin-1 coupling to endolysosomes can also be achieved across ER-endosome contact sites, a process mediated by the ER protein protrudin. Importantly, mutations in protrudin cause a form of hereditary spastic paraplegia (110), a length-

dependent axonopathy affecting fibers of the cortico-spinal tract (111). In this anterograde lysosome transport mechanism, ER-anchored protrudin forms contacts with late endosomes through interaction with Rab7 and phosphatidylinositol 3-phosphate (PtdIns3P) on the lysosome membrane. Protrudin then transfers kinesin-1 onto FYVE- and coiled-coil-domain-containing protein 1 (FYCO1)-positive late endosomes, thus facilitating endolysosome transport towards microtubule-plus ends (**Figure 1.9**) (112-114). Amino acid depletion was observed to reduce PtdIns3P levels, disrupting protrudin/FYCO1-mediated anterograde transport, leading to perinuclear lysosome localization (115). Interestingly, overexpression of KIF5A results in protrusion formation in HeLa cells in a protrudin-dependent manner, suggesting a role for late endosomes in neurite outgrowth (112-114). In addition, under normal nutrient conditions, sensing of the fatty acid precursor malonyl CoA by the enzyme carnitine palmitoyltransferase 1C (CPT1C) was observed to enhance protrudin transfer of kinesin-1 to late endosomes through FYCO1 (116). However, under conditions of metabolic stress, this process was found to be largely prevented, representing a lysosome positioning mechanism regulated in response to changes in the cellular environment (116).

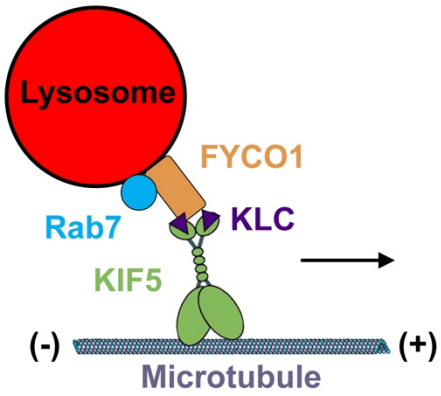


Figure 1.9 – Schematic diagram of the Rab7/FYCO1/Kinesin-1 complex for lysosome movement towards microtubule-plus ends. *Model adapted from Raiborg C et al., 2015 (114).*

1.5.2 – Retrograde Transport

Cytoplasmic dynein is the major motor protein that drives organelle transport towards microtubule-minus ends. It is composed of two heavy chains with ATPase activity, four intermediate light chains, and several light chains (117). In addition, an associated protein complex called dynactin interacts with dynein and is required for dynein association with lysosomes (118). Similar to the mechanisms for kinesin-1 loading, lysosome coupling to dynein motors is also mediated by several adaptor protein complexes recruited to the lysosome surface under various conditions.

One mechanism for dynein attachment to endolysosome membranes involves a series of interactions between Rab7, the Rab7-interacting lysosomal protein (RILP), and the oxysterol-binding protein-related protein 1L (ORP1L) (**Figure 1.10**) (119). RILP links late endosomes to dynein-dynactin through interactions with Rab7 and the $p150^{Glued}$ subunit of the dynactin complex. Late endosome-localized ORP1L then facilitates transfer of Rab7-RILP-dynein-dynactin to the membrane-associated receptor βIII spectrin through interaction with the dynactin subunit actin-related protein 1 (Arp1) (119), which is required for dynein motor anchoring and activation (120). Interestingly, ORP1L was subsequently identified as a cholesterol sensor that changes conformation in response to endosomal cholesterol levels, representing a retrograde transport mechanism regulated in response to a form of lysosomal stress (121). Under low endosomal cholesterol conditions, late endosome localized ORP1L binds the ER protein VAPA (vesicle-associated membrane protein (VAMP)-associated ER protein A), which interacts with Rab7-RILP to remove dynein-dynactin from late endosomes. However, under high endosomal cholesterol conditions, ORP1L changes conformation

and is released from VAPA interaction, allowing association of late endosomes with dynein-dynactin for retrograde transport (121).

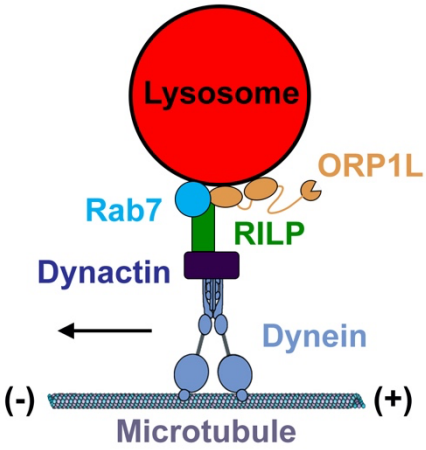


Figure 1.10 – Schematic diagram of the Rab7/RILP/ORPL1/Dynein-Dynactin complex for lysosome movement towards microtubule-minus ends. *Model adapted from Johansson M et al., 2007 (119).*

In addition, the TRPML1/ALG2 complex was also described to mediate retrograde endolysosome movement (**Figure 1.11**) (122). Transient receptor potential mucolipin 1 (TRPML1, also known as MCOLN1) is a lysosomal calcium channel that facilitates calcium release from the lysosome. Importantly, mutations in TRPML1 cause Mucolipidosis type IV (MLIV), a neurodegenerative lysosomal storage disorder (123, 124). In this retrograde lysosome transport mechanism, TRPML1 activation releases lysosomal calcium and increases TRPML1-mediated lysosome association of apoptosis-linked gene 2 (ALG2), an EF-hand containing protein that acts as both a lysosomal calcium sensor (125, 126) and adaptor protein to the dynein-dynactin complex (122). Therefore, lysosomal calcium release facilitates dynein-dynactin recruitment through TRPML1/ALG2. This pathway was described to provide an on-demand mechanism for lysosome transport towards the cell center in response to acute

starvation, and therefore was suggested to be distinct from the Rab7-RILP cholesterol-dependent mechanism for retrograde lysosome movement (122).

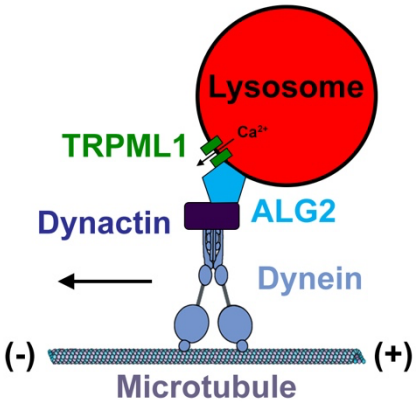


Figure 1.11 – Schematic diagram of the TRPML1/ALG2/Dynein-Dynactin complex for lysosome movement towards microtubule-minus ends. *Model adapted from Li X et al., 2016 (122).*

Furthermore, the recently described TMEM55B/JIP4 pathway represents an additional mechanism driving retrograde endolysosome movement towards microtubule-minus ends (**Figure 1.12**) (127). TMEM55B is a lysosomal integral membrane protein that contains several CLEAR (coordinated lysosomal expression and regulation) motifs in its promoter region, suggesting it is under the transcriptional control of TFEB/3 (74). Overexpression of TMEM55B repositions lysosomes tightly around the cell center, whereas TMEM55B depletion increases lysosome localization at the cell periphery (127). TMEM55B recruits dynein adaptor JNK-interacting protein 4 (JIP4) to the lysosome surface, facilitating dynein-dynactin association with endolysosomes. Intriguingly, conditions of lysosomal stress activate TFEB/3, resulting in TMEM55B upregulation, leading to JIP4-dependent retrograde lysosome transport. Importantly, RILP overexpression induces perinuclear lysosome clustering in cells depleted of either TMEM55B or JIP4, and TMEM55B overexpression similarly induces lysosome

accumulation near the cell center in TRPML1-depleted cells (127). These results suggest that the TMEM55B/JIP4 mechanism for retrograde lysosome transport functions independently of the Rab7/RILP/ORP1L and TRPML1/ALG2 pathways. Indeed, it will be particularly interesting to further determine why the cell has adapted multiple mechanisms regulating retrograde lysosome movement.

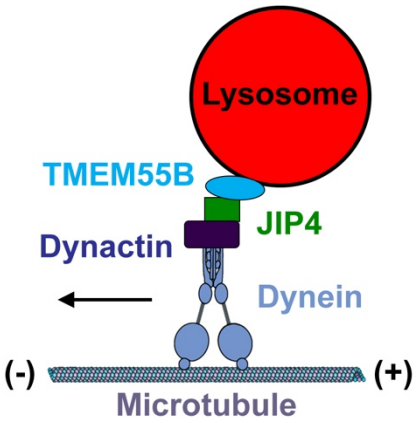


Figure 1.12 – Schematic diagram of the TMEM55B/JIP4/Dynein-Dynactin complex for lysosome movement towards microtubule-minus ends. *Model adapted from Willet R et al., 2017 (127).*

1.6 – Neuronal Lysosome Transport and Neurodegeneration

Neurons are highly polarized cells consisting of a cell body, branched dendrites, and a single axon that can span up to one meter in length. Given this extended morphology, neurons require efficient transport mechanisms to coordinate movement of organelles and synaptic components to sites in high demand (128-130). Microtubule-based kinesin and dynein motors drive long distance transport, whereas actin-based myosin motors mediate short range movement (104, 128). Efficient transport is critically important in maintaining neuronal growth, survival, and function but is particularly challenging in distal regions of the neuron.

1.6.1 – Neuronal Lysosomes

Lysosomes are essential for proper neuron function and survival. Primary lysosome dysfunction results in progressive neurodegeneration in the majority of LSDs (5), and numerous studies have implicated declining lysosome function in the pathogenesis of aging-related neurodegenerative diseases (131). Neurons are particularly vulnerable to various defects in lysosome positioning and function, in part due to their size and longevity (132). Indeed, their highly polarized morphology and post-mitotic state pose exceptional challenges in maintaining cellular homeostasis in regions far removed from the cell body, where biosynthesis and degradation are enriched. Anterograde transport supplies new materials and organelles to distal regions to support growth and synaptic transmission (133-135), whereas retrograde transport removes aged proteins and defective organelles from the periphery of the cell (136-138). Therefore, neurons require coordinated intracellular transport mechanisms to maintain quality control throughout their extended architecture over the course of a lifetime.

Notably, the endolysosomal system shows a degree of spatial compartmentalization in neurons. Neuronal lysosomes are enriched in the cell body (135, 137, 139-141), representing a distribution pattern thought to facilitate coordination between degradation and biogenesis pathways in the soma. However, lysosomes and lysosome-like organelles have also been detected in dendrites and axons (135, 140, 142-146), an observation that may reflect the existence of lysosome sub-populations with distinct functions and/or lysosomes at varying degrees of maturation.

Recent studies highlight the importance of using a combination of endogenous endolysosomal markers to study neuronal lysosomes (141, 147), which may show even greater heterogeneity than observed in non-neuronal cells (141). The commonly used

lysosome marker LAMP1 (lysosome associated membrane protein 1) was found to be distributed among a diverse population of degradative and nondegradative endolysosomal and autophagic organelles in neurons (**Figure 1.13**) (147). In line with this observation, many LAMP1-labeled organelles in medial/distal dendrites lacked cathepsins B/D (141), and lysosomes labeled with LAMP1 displayed reduced acidity at axon terminals compared to their acidity in dendrites and proximal axons (143). These studies demonstrate the heterogeneity of LAMP1-labeled compartments and help clarify criteria that may be used to monitor neuronal lysosomes, which can be defined as acidic LAMP1-positive organelles containing active lysosomal hydrolases and degraded substrates (141, 147).

Nonetheless, as in non-neuronal cells, lysosomes (and their intermediates) are distributed throughout the neuron via regulated transport mechanisms. Long-range lysosome transport to peripheral regions of dendrites and axons depends in part on their ability to engage in motor-adaptor interactions as well as the organization of the microtubule cytoskeleton within these domains. In axons, microtubules are uniformly polarized with plus-ends oriented outward and minus-ends directed inward (148). Therefore, kinesin motors mediate anterograde transport toward distal axon terminals, whereas dynein motors mediate retrograde transport from distal axons towards the cell soma. However, dendritic microtubules exhibit mixed polarity (149). Therefore, depending on the orientation of the microtubule track a motor-adaptor complex is engaged on, kinesin and dynein motors may drive lysosome transport in either direction in dendrites.

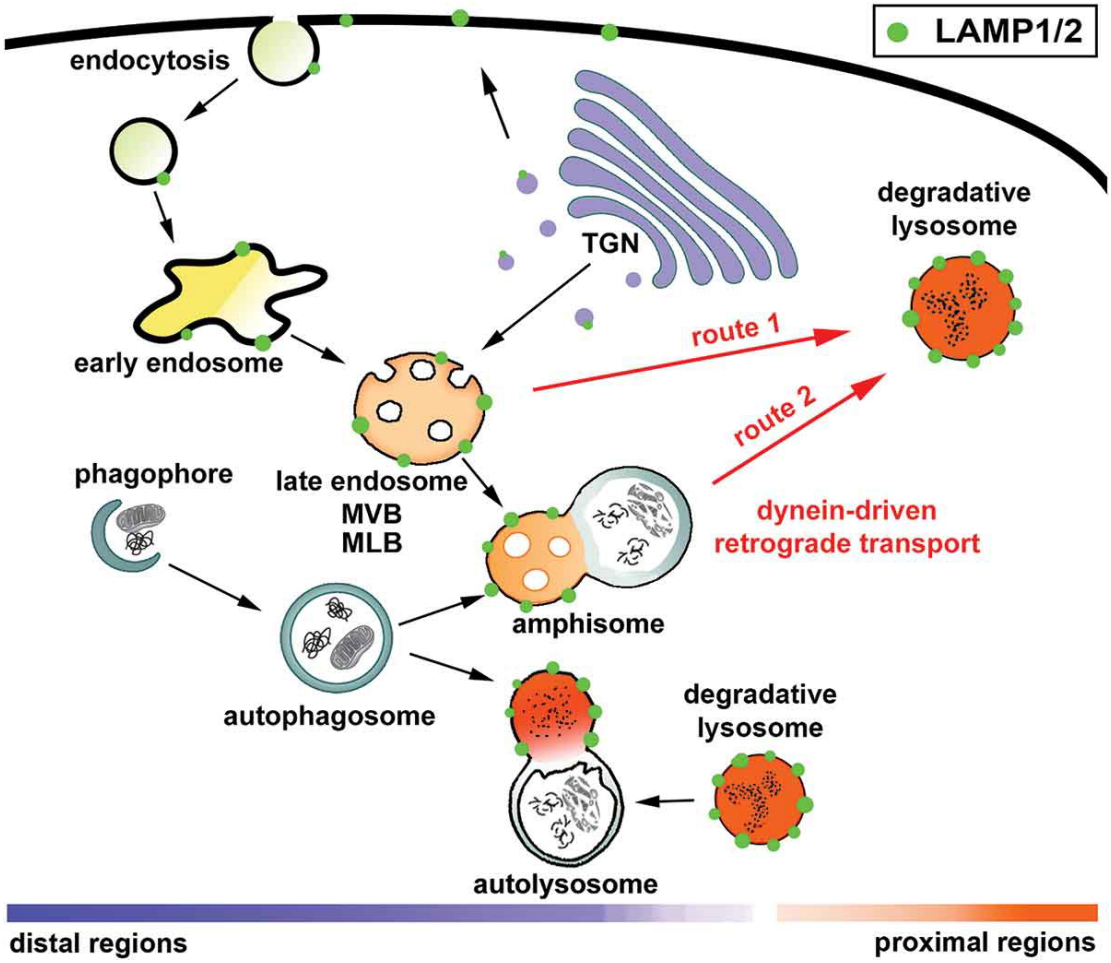


Figure 1.13 – Schematic diagram showing LAMP1/2 distributed among a heterogenous population of endocytic and autophagic organelles in neurons. *Endocytic (route 1) and autophagic (route 2) pathways deliver cargo to lysosomes. Intermediates along these membrane trafficking routes also contain LAMP1 at varying degrees. Model taken directly from Cheng XT et al., 2018 (147).*

1.6.2 – Dendritic Lysosome Transport

Lysosomes and their intermediates have been observed in dendrites. A recent study investigating the distribution of endosomes and lysosomes in the somadendritic region demonstrated a spatially compartmentalized organization (141). While early and late endosomes were found throughout the length of dendrites, degradative lysosomes positive for LAMP1 and cathepsins B/D were enriched in the soma. This spatial gradient

of degradative activity was further revealed using DQ-BSA, a fluorogenic substrate that traffics to the lysosome through the endocytic pathway and fluoresces upon hydrolysis by multiple lysosomal proteases. Interestingly, interference with Rab7 caused dendritic accumulation of short-lived membrane proteins Nsg1 and Nsg2, suggesting that terminal degradation of these dendritic cargos requires Rab7-dependent late endosome transport to somatic lysosomes (141).

However, several studies also observed acidic lysosomes distributed throughout dendrites and dendritic spines (145, 146). These lysosomes were positive for LysoTracker, a fluorescent pH-sensitive probe that labels acidic compartments. LysoTracker signal in dendritic lysosomes was sensitive to treatment with GPN (145, 146), a cell-permeable substrate that induces osmotic lysis following cleavage by the lysosomal hydrolase cathepsin C (150). These studies suggest a population of lysosomes with some functionality located in dendrites and dendritic spines.

Time-lapse live cell imaging of dendritic lysosomes revealed a bidirectional motility pattern that accounted for more than half of the total dendritic lysosome pool, while the rest remained stationary (143, 145, 151). Inhibition of lysosome proteolytic function with leupeptin treatment resulted in an increase in the population of stationary lysosomes and a decrease in dendritic spine density, suggesting that lysosomal degradation capacity is linked to their trafficking and function in dendrites (145). Consistent with these findings, promoting a balance between anterograde and retrograde lysosome transport restored dendrite loss in neurons with knockdown of TMEM106B, a major risk factor for frontotemporal lobar degeneration (FTLD) with TDP-43 pathology (152). Together, these results support a role for dendritic lysosome transport in the maintenance of dendritic branching and spine density (145, 152).

Interestingly, the microtubule and actin cytoskeletons were observed to inversely affect lysosome trafficking in dendrites. While microtubule disruption by nocodazole treatment significantly decreased lysosome movement, disruption of the actin cytoskeleton by latrunculin A increased lysosome motility (145, 151). Notably, these opposing effects on dendritic lysosome dynamics in response to cytoskeleton-disrupting agents were also observed for axonal mitochondria near actin-enriched presynaptic terminals (153). Further studies revealed that lysosome stalling at actin patches of dendritic spines is mediated by the actin-based motor myosin Va (151). Remarkably, lysosome positioning at dendritic spines was also found to be regulated by synaptic activity, where stimulation of NMDA and AMPA receptors triggered an increase in the number of lysosome-containing dendritic spines (145). Local glutamate uncaging at an individual spine resulted in lysosome recruitment and increased pausing at its base, indicating a role for F-actin in positioning lysosomes near spines and synapses in response to neuronal activity (145, 151).

Dendritic lysosomes were also observed to regulate the structural plasticity of spines in an activity-dependent manner (146). Lysosomal calcium release evoked by back-propagating action potentials triggered lysosome fusion with the plasma membrane, resulting in the release of cathepsin B through lysosomal exocytosis. Local release of cathepsin B activated metalloproteinase 9, which remodeled the extracellular matrix to regulate dendritic spine plasticity and morphology. Inhibition of lysosomal calcium signaling or cathepsin B release prevented this activity-dependent remodeling, highlighting the importance of lysosome positioning and function to synaptic homeostasis (146).

1.6.3 – Axonal Lysosome Transport

Early studies measuring the pH of endocytically-derived cargos in axons demonstrated an increasing frequency of acidified organelles as cargos moved from distal to proximal regions, suggesting a retrograde model of axonal endosome maturation (**Figure 1.14**) (154). This observation was speculated to result from an increased likelihood of endosomes to fuse with Golgi-derived vesicles in the proximal axon region, or an increased probability of proton pump activation as cargos move closer to the soma (154). Similar observations for endosome maturation were later noted, as endocytic substrates transited through early and late endosomes as they progressed along a retrograde transport route toward the soma (155).

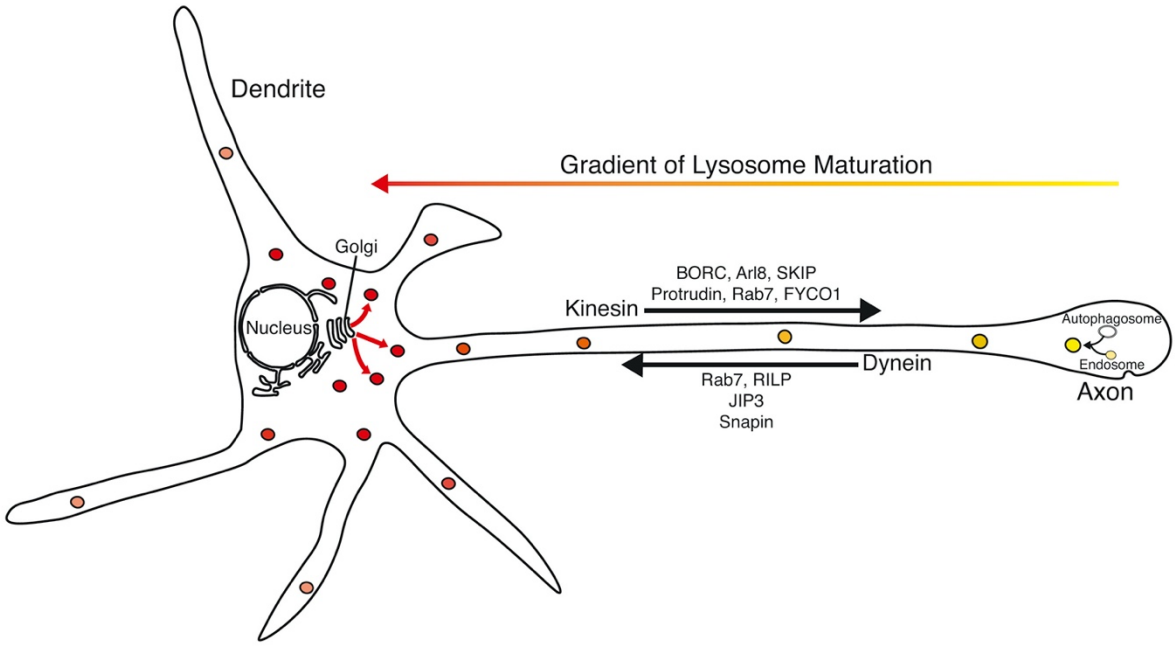


Figure 1.14 – Schematic diagram of axonal lysosome maturation. *Endosomes and autophagosomes located at distal axon terminals mature as they move retrogradely toward the cell body. Model taken directly from Ferguson SM, 2018 (156).*

Recent studies into autophagy in axons provided further insights in support of a retrograde maturation model. While some cell types show autophagosome formation in

seemingly random locations in peripheral regions of the cell (157), autophagosomes in axons form constitutively at distal terminals (158). Once formed, autophagosomes display short, bidirectional, oscillatory movements, followed by robust retrograde transport towards the cell body, driven by dynein motors (142, 158-160). Scaffolding proteins including JNK-interacting protein 1 (JIP1) and Huntington were shown to regulate autophagosome motor activity to ensure their retrograde processivity (161, 162), a feature observed in many neuronal systems (142, 161-165). This retrograde motility pattern was linked to their maturation in part using the dual color fluorescent autophagosome reporter mCherry-EGFP-LC3 (158), which monitors autophagosome maturation based on preferential EGFP quenching at acidic pH following fusion(s) with lysosomes (166). This reporter revealed more acidified autolysosomes in proximal axons compared to distal regions (158), consistent with previous observations showing that axonal autophagosomes mature during their retrograde transport route (142).

Dynein-dependent movement of autophagosomes mediates efficient encounters with lysosomes to facilitate cargo degradation (159). Mutations in dynein or alterations in its function disrupt retrograde transport, leading to autophagic cargo buildup and degeneration of motor neurons in mice (157, 167-169). Therefore, to maintain effective autophagic clearance capacity in axons, proper retrograde autophagosome transport is required. Axonal autophagosomes acquire dynein motors through fusion with late endosomes in a motor-adaptor sharing model (136). The majority of axonal autophagosomes colocalize with late endosome marker Rab7, and therefore amphisomes were observed to be moving retrogradely in axons (136, 142, 158). Disrupting autophagosome-late endosome fusion by knockdown of autophagosomal SNARE protein syntaxin 17 impaired autophagosome trafficking in axons, suggesting a role for amphisome formation in autophagosome motility (136). Interestingly, blocking

amphisome formation reduced dynein motor recruitment to axonal autophagosomes, leading to their accumulation in distal axons (136). Alternatively, disrupting dynein recruitment to late endosomes through interference with the late endosome-associated dynein adaptor Snapin also retained autophagosomes in distal axons, highlighting the importance of autophagosome-late endosome fusion and retrograde transport for autophagosome clearance from distal axons (136, 170).

Snapin acts as an adaptor protein that couples dynein motors to late endosomes to facilitate their retrograde movement (137). Deleting *snapin* reduces dynein association with late endosomes, whereas *snapin* overexpression enhances tubular lysosome formation through interactions with the dynein subunit DIC (dynein intermediate chain) (137). Consistently, *snapin*$^{-/-}$ neurons exhibit phenotypes linked to impairments in retrograde late endosome transport, including aberrant accumulation of immature lysosomes, reduced lysosomal proteolysis, and impaired autolysosome clearance (137). These phenotypes were rescued by reintroducing *snapin*, indicating a role for Snapin in autophagy-lysosomal function (137). Consistent with its role in late endocytic trafficking in axons, Snapin was also observed to promote synaptic vesicle sorting to the endolysosomal pathway (171) and endosome-to-Golgi retrieval of cation independent M6PRs to support lysosome biogenesis in the soma (172). Together, these studies highlight the importance of retrograde late endosome transport to the maintenance of neuronal homeostasis.

Dynein loading onto lysosome membranes was also observed to be mediated by JNK-interacting protein 3 (JIP3). JIP3 associates with lysosomes (140, 173) and interacts with dynein subunits including p150^{Glued} (174) and dynein light intermediate chain (DLIC) (175). JIP3 colocalizes with lysosomes moving bidirectionally along axons, and

loss of JIP3 was shown to reduce lysosome association with dynein motors (173). Interestingly, JIP3 loss-of-function mutants display lysosome accumulations in axon terminal swellings, consistent with defects observed in retrograde lysosome movement (173). This was further supported by the observation that JIP3 knockout (KO) dystrophic axons contain immature lysosomes with low levels of cathepsins, representing a population of lysosomal intermediates distinct from lysosomes in the cell body (140). However, because JIP3 also interacts with components of the kinesin-1 motor to mediate anterograde cargo transport (176, 177), it was proposed that JIP3 may serve as a scaffolding protein regulating vesicular cargo transport (175, 176, 178, 179), highlighting how anterograde and retrograde pathways may be integrated to coordinate events throughout the axon (180).

Several recent studies revealed new insights into the endolysosomal system in axons. Live observation of axon terminals in intact *Drosophila* brains showed two parallel pathways for membrane protein sorting and degradation (144). To monitor these events, various membrane protein cargos were fused with a dual color mCherry-pHluorin tag, whose green fluorescent signal is quenched at acidic pH (181). Interestingly, distinct molecular machineries were found to be involved in cargo-specific sorting and degradation at axon terminals. While synaptic vesicle proteins were sorted for local degradation, plasma membrane proteins required Rab7-dependent sorting and transport toward the soma, where degradation started at axon terminals and was fulfilled *en route* to the cell body (144). Intriguingly, cathepsin-L-like protease 1 (CP1) showed specificity for executing local degradation of synaptic vesicle proteins at axon terminals, indicating the presence of lysosome subpopulations in axons with distinct functions (144).

In addition, the BORC/Arl8/SKIP/Kinesin-1 complex (**Figure 1.8**), previously identified in non-neuronal cells, was recently demonstrated to drive lysosome transport into axons (143). Interference with multiple components of this multiprotein complex selectively impaired axonal lysosome positioning, whereas overexpression promoted lysosome transport into axons and axon terminals but not dendrites (143). Interestingly, kinesin-1 requires SKIP to drive axonal lysosome transport, and both Arl8 and SKIP were observed to be limiting factors in coupling lysosomes to kinesin-1 in neurons (143). Reduced lysosome transport into axons resulted in reduced growth cone dynamics and stationary autophagosomes in axons (143), consistent with a role for anterograde lysosome transport in supporting axonal autophagosome maturation (135, 143). Interestingly, mice with spontaneous mutations in *Borcs7* (a subunit of BORC) showed progressive axonal dystrophy and impairments in motor function, indicating a requirement for BORC-dependent axonal lysosome positioning to proper neuronal function (182). In addition, BORC and Arl8 were also shown to mediate the anterograde transport of synaptic vesicle precursors in axons of *C. elegans*, suggesting that lysosomes and synaptic vesicles share common transport machinery (183, 184). However, a subsequent study demonstrated that BORC was dispensable for the axonal transport of synaptic vesicle precursors in mammalian neurons, an observation that may suggest species-specific differences in coupling kinesin-1 motors to lysosomes and synaptic vesicle precursors (185).

Notably, our recent study expanded on previous observations reporting lysosome transport into axons by showing a population of active lysosomes that are continuously delivered to distal axons from soma-derived pools (135). These lysosomes were labeled using a set of endogenous activity-based lysosome probes specific to active forms of several lysosomal hydrolases including cathepsins B, D, L, and

glucocerebrosidase (GCase). These soma-derived degradative lysosomes were rapidly transported into axons and targeted to growth cones and axonal autophagic cargo (135). Disrupting axonal lysosome delivery by knockdown of kinesin-lysosome adaptor Arl8 resulted in the accumulation of autophagosomes and mutant alpha-synuclein cargos in distal axons, highlighting a role for anterograde lysosome transport in the maintenance of axonal homeostasis (135).

1.6.4 – Lysosome Dysfunction, Mistrafficking, and Axonal Dystrophy

Axonal dystrophy and autophagic stress are two major pathological features of common neurodegenerative diseases and LSDs associated with lysosome dysfunction (44, 139, 142, 186-193). In several of these diseases, dystrophic axons contain accumulated organelles related to the endo-lysosomal-autophagic pathways, reflecting defects in their maturation and/or clearance. Because these membrane trafficking routes are dynamic and span the length of axons, defects at various steps have been described to contribute to the buildup of lysosome-like and autophagic organelles within swollen axons in these diseases.

Genetic variants in TMEM106B have been linked to several neurodegenerative diseases including FTLD (194). TMEM106B deficiency results in lysosome acidification defects, leading to a reduction in the activities of multiple lysosomal hydrolases (195). TMEM106B-deficient mice develop axonal swellings at the axon initial segment (AIS), resulting in functional motor deficits (196). These axonal alterations were found to contain large lysosome-like vacuoles that were positive for LAMP1 and negative for LysoTracker and cathepsin D, representing a population of immature lysosomal intermediates (196). TMEM106B deficiency was observed to result in axonal lysosome

transport defects and impaired degradation of lysosomal substrates, suggesting a link between TMEM106B-associated lysosomal deficits and retrograde sorting at the AIS (196).

In Alzheimer's disease (AD), defects in lysosome acidification and proteolysis have also been linked to the characteristic axonal dystrophy of AD (142). Studies into AD brain pathology in post-mortem samples (197) as well as mouse models of AD (139) revealed striking accumulations of degradative, lysosome-like organelles within AD dystrophic axons (**Figure 1.15**). These aberrantly accumulated organelles were predominantly characterized as autophagic vacuoles (AVs), multivesicular bodies, multilamellar bodies, and autolysosomes (197). Studies in mouse models of AD revealed that these organelles are positive for LAMP1 and deficient in multiple lysosomal proteases including cathepsins B, D, L, and asparaginyl endopeptidase (139).

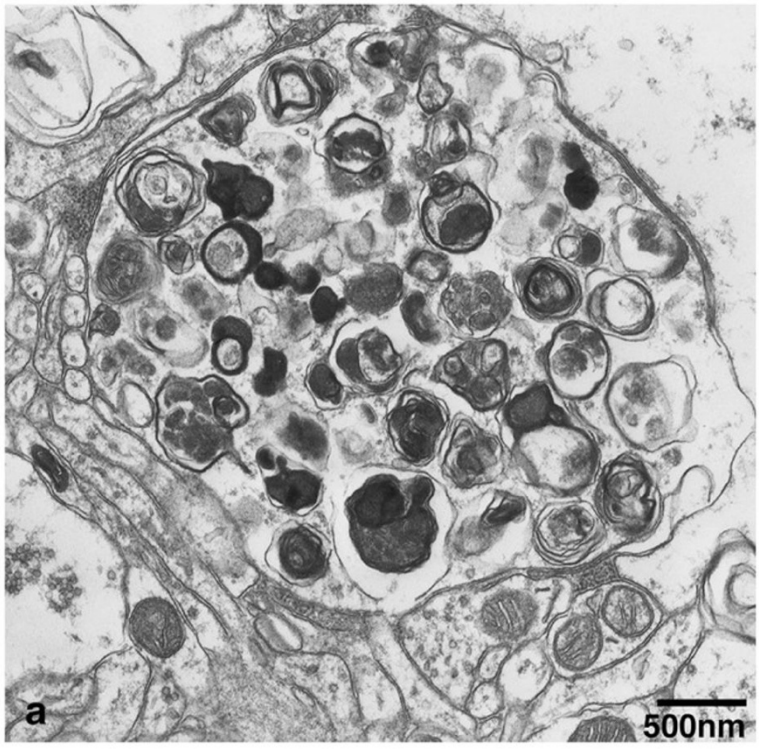


Figure 1.15 – Ultrastructural image of a dystrophic axon from a post-mortem cortex of a patient with Alzheimer's disease. *Note the heterogeneous accumulation*

of endo-lysosomal-autophagic cargo within axonal swellings in AD. Cropped image taken directly from Nixon RA et al., 2005 (197).

Interestingly, inhibition of lysosomal proteolytic function by leupeptin or bafilomycin A1 treatment slowed the axonal transport of both autophagosomes and endolysosomes, leading to their selective accumulation within dystrophic axons characteristic of AD (142). These results indicate that a block in the retrograde transport of degradative organelles contributes to their axonal accumulation and impaired maturation in AD axonal swellings. Similar organelle accumulations were also observed in JIP3 KO neurons, which were characterized as lamellar, multivesicular, and electron-dense organelles with lysosome morphology (140). Because these accumulated lysosome-like organelles in JIP3 KO neurons resemble a population derived from distal endocytic and autophagic pathways, they are thought to result from a block in retrograde transport, leading to impaired maturation of lysosome precursors (140).

Pathogenic proteins associated with AD, as well as amyotrophic lateral sclerosis (ALS) and Huntington's disease (HD), were observed to disrupt dynein-mediated coupling to late endosomes and autophagosomes, thereby providing mechanistic insight underlying impaired retrograde transport in these diseases. In an AD-linked mouse model, amyloid beta oligomers were found to associate with axonal AVs and competitively disrupt dynein-Snapin coupling, leading to impaired recruitment of dynein motors and accumulation of axonal AVs (170). Similarly, in a familial ALS-linked mouse model with the G93A mutation in human SOD1 ($hSOD1^{G93A}$), mutant SOD1 was observed to interact with DIC (198) and interfere with dynein loading onto late endosomes, resulting in impaired retrograde transport and autophagy-lysosomal deficits that underlie mitochondrial pathology in ventral root axons (186). In addition,

pathogenic polyglutamine expansions in Huntington that cause HD were observed to disrupt retrograde axonal autophagosome transport, leading to a defect in autophagosome maturation and cargo clearance in axons (161).

Together, these observations highlight the importance of understanding the relationship between altered lysosome function, mistrafficking, and axonal pathology, and their contribution to the pathogenesis of neurodegenerative diseases.

1.7 – Hypothesis and Specific Aims

Our overall research goal is to uncover mechanisms that contribute to altered axonal homeostasis in NPC using live-neuron imaging combined with genetic and pharmacologic approaches. Our central hypothesis is that defects in the axonal transport of lysosomes disrupt maturation and progression of the autophagy-lysosomal pathway and contribute to NPC pathogenesis. To test this hypothesis, we aimed to (1) characterize axonal autophagosome-lysosome transport and distribution in NPC; (2) investigate mechanisms underlying impairment of this process; and (3) genetically and/or pharmacologically rescue transport defects in NPC axons using glycosphingolipid biosynthesis inhibitors, cholesterol-mobilizing agents, and/or calcium-modulating drugs.

CHAPTER 2 – CHARACTERIZATION OF AXONAL ORGANELLE TRANSPORT AND DISTRIBUTION IN NPC

2.1 – Introduction

Lysosomes play key roles in maintaining cellular homeostasis by degrading and recycling substrates received from multiple routes including the endocytic and autophagic pathways (58, 69, 70). Degradation of endocytic and autophagic cargos depend on their dynamic interactions with lysosomes, which provide the acid hydrolases required for substrate degradation (60). To carry out this function efficiently, lysosomes depend on their ability to move bidirectionally along microtubules throughout the cytoplasm (90, 95). However, this process is particularly challenging in neurons due to their highly polarized morphology with axons that can extend up to one meter in length. Neurons are therefore highly vulnerable to various defects in lysosome trafficking, positioning and function, which are associated with both rare and common neurodegenerative diseases (1, 199-201). While enzymatically active degradative lysosomes are enriched in the cell body (137, 139-141), mature lysosomes and lysosome-like organelles are also found in distal axons (135, 140, 142-144). However, the impact of lysosome anterograde trafficking and positioning on axonal pathology in neurodegenerative diseases remains largely elusive.

Niemann-Pick disease type C (NPC) is a neurodegenerative lysosomal storage disorder (LSD) characterized by the accumulation of multiple lipids in the endolysosomal compartment (31). Loss of function mutations in the lysosomal membrane protein NPC1 account for approximately 95% of NPC cases (22), while the other 5% are caused by mutations in the lysosomal luminal protein NPC2 (24), though the two forms are clinically indistinguishable (10, 21). One major pathologic feature observed in NPC patients and recapitulated in mouse models of NPC disease is axonal dystrophy, which consists of bulbous swellings that contain accumulated organelles

(39, 44, 45, 51). These axonal changes precede symptom onset and neurodegeneration in NPC mice, suggesting that defects in the trafficking and degradation of these axonal organelles contribute to early NPC pathology. These clinical implications highlight the importance of understanding the cellular events that precede axonal organelle accumulation and their contribution to neurodegeneration. However, the mechanisms underlying these early pathologic events in NPC neurons remain obscure.

The goal of this study was to identify cellular and pathological mechanisms underlying organelle accumulation in NPC dystrophic axons using live-neuron imaging combined with genetic and pharmacologic approaches. In this chapter, we work towards this goal by first characterizing the organelles that accumulate within NPC dystrophic axons and defining the axonal distribution and trafficking pattern of autophagosomes and lysosomes in NPC neuronal axons cultured from mice at presymptomatic stages.

2.2 – Materials and Methods

2.2.1 – *Npc1* Mouse Model and Care

Npc1$^{-/-}$ (BALB/cNctr-Npc1^{m1N}/J; *Npc1* null) and WT (*Npc1*$^{+/+}$) mice were generated from heterozygote (*Npc1*$^{+/-}$) matings, and breeder pairs were kindly provided by Dr. William Pavan (23). Animals were maintained in the NINDS Animal Facility, and all animal procedures were performed in accordance with NIH guidelines and approved by the NINDS/NIDCD Animal Care and Use Committee.

In this study, both cortical and dorsal root ganglion (DRG) neurons were used, representing two regions vulnerable to neurodegeneration in *Npc1*$^{-/-}$ mice (43, 50). Cortical neurons were obtained from mouse embryos, whereas DRG neurons were obtained from young adult mice. Cortical neurons isolated from embryonic mouse brains represent a widely used model to study intracellular organelle transport, but isolation and culture from adult mice remains cumbersome (202, 203). Because cortical neurons were cultured from mouse embryos, these neurons were used to monitor early stages of disease development. However, DRG neurons represent an ideal model system amenable to isolation and culture from adult mice in our previous studies (135, 136, 138, 186). Therefore, DRG neurons were used to monitor disease progression at presymptomatic stages in young adult mice at postnatal day 30-40 (P30-40) and were referred to as isolated from presymptomatic *Npc1*$^{-/-}$ mice throughout the text. DRG neurons were cultured for 3-4 days *in vitro* (DIV) because they display robust axon outgrowth and reach approximately 1000 μm in length at DIV2 (158). Therefore, culturing for longer time periods may hinder analyses of axonal organelle transport due to axon overcrowding. Embryonic cortical neurons were cultured for 7-10 days *in vitro*,

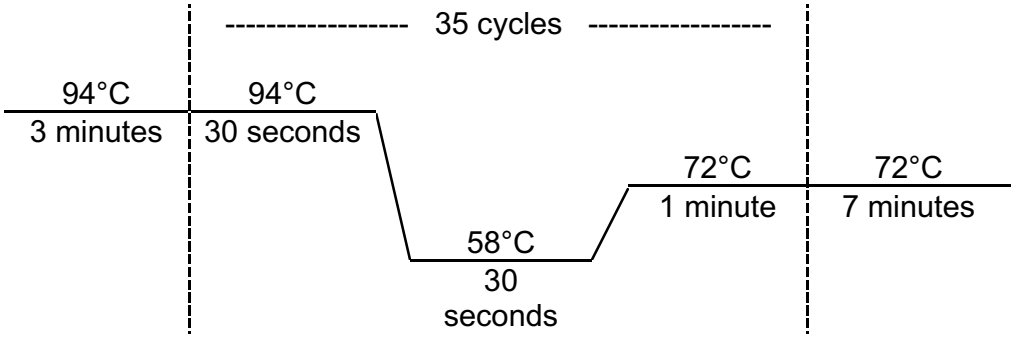
representing the time it takes for an adequate number of axons to grow into the axon chamber of a microfluidic device to monitor axonal organelle transport and distribution.

2.2.1.1 – *Npc1* Mouse Genotyping

The polymerase chain reaction (PCR) was carried out to identify *Npc1* mouse genotypes as previously described (23) with minor modifications. Mouse tail genomic DNA (gDNA) was extracted with 72.5 µl DirectPCR Lysis Reagent (Viagen Biotech) and 2.5 µl proteinase K (Viagen Biotech) for each 0.5 cm tail sample. Tails were digested at 56°C while shaking at 1300 revolutions per minute (rpm) for 1 hour followed by 95°C for 12 minutes to inactivate proteinase K. Mouse tail gDNA was then used as a template to amplify the region between Exon 9 and Exon 10 of *Npc1* using PCR. This region contains the 824-base pair (bp) retroposon-like sequence insertion resulting in a stop codon and premature truncation of NPC1 in *Npc1*$^{-/-}$ mice (23). The reagents and volumes for each reaction are given below, and primer sequences used for *Npc1* mouse genotyping are located in Appendix 1.

Reagent	Volume per reaction (µl)
PCR buffer (10X)	2
dNTPs (2.5 mM)	2
Forward primer (10 µM)	1
Reverse primer (10 µM)	1
GoTaq enzyme	0.2
Nuclease free water	11.8
TOTAL	**20**

A no template control was run with every reaction to ensure primer specificity, and the following amplification conditions were used.



2.2.1.2 – Agarose Gel Electrophoresis

After PCR reactions were complete, agarose gel electrophoresis was then applied to assess *Npc1* mouse genotypes. A 2% agarose gel was made by dissolving 2% w/v agarose (Bioline) in 1X Tris Acetate Buffer (TAE; Quality Biological), followed by addition of SYBR Safe DNA Gel Stain (Thermo Fisher Scientific) to visualize DNA fragments. An equal volume of 2X DNA Loading Dye Solution (Crystalgen) was added to each PCR product, then loaded on the agarose gel. A 1 kilobase (kb) pair ladder (Thermo Fisher Scientific) was included as a base pair (bp) size reference standard, and electrophoresis was carried out at 120 volts for 30-45 minutes. The DNA gel was visualized using a G:BOX gel doc imaging system (Syngene). In the *Npc1*$^{-/-}$ allele, 703 bp of WT sequence (44 bp of exon 9 and 659 bp of intron 9-10) is replaced by 824 bp of the MalR retroposon-like sequence (23). Therefore, using the primer combination listed in Appendix 1, the WT allele is 1048 bp while the *Npc1*$^{-/-}$ allele is 1209 bp.

2.2.2 – Antibodies and Probes

Antibodies used in this study are detailed in Appendix 2. BODIPY-FL-pepstatin A (P12271) was obtained from Thermo Fisher Scientific. Filipin (F9765) and 2-hydroxypropyl-β-cyclodextrin (H107) were obtained from Sigma-Aldrich. MDW933 and MDW941 were generous gifts from Dr. Ellen Sidransky (NHGRI, NIH). The EGFP-LC3 plasmid used in DRG neurons was generated as previously described (136). The Arl8b-mCh plasmid was a kind gift from Dr. Juan Bonifacino (NICHD, NIH) and was either used directly or subcloned into the pLEX lentiviral vector with a PGK promoter to produce lentivirus. The pGEX-KG-D4H*-mCh plasmid (134604) was purchased from Addgene. The psPAX2 and pMD2.G plasmids were gifts from Dr. Didier Trono (Swiss Federal Institute of Technology Lausanne; EPFL).

2.2.2.1 – Labeling Lysosomes with Activity-Based Lysosome Probes

2.2.2.1.1 – Active Glucocerebrosidase

For labeling active glucocerebrosidase (GCase) (**Figure 2.1A**), green (MDW933) and red (MDW941) fluorescent activity-based probes specific for GCase (135, 204) were kindly provided by Dr. Ellen Sidransky (205). Live neurons were incubated with 500 nM MDW933 or 100 nM MDW941 for 30 minutes at 37°C and 5% CO_2 followed by fixation in Bouin's solution (Millipore Sigma) with 4% sucrose for immunostaining as in Section 2.2.8 or live-neuron imaging as in Section 2.2.11.

2.2.2.1.2 – Active Cathepsin D

For labeling active cathepsin D (CTSD) (**Figure 2.1B**), live neurons were incubated with 1 µM BODIPY-FL-pepstatin-A (Thermo Fisher Scientific) for 30 minutes at 37°C and 5% CO_2 followed by live-neuron imaging as in Section 2.2.11.

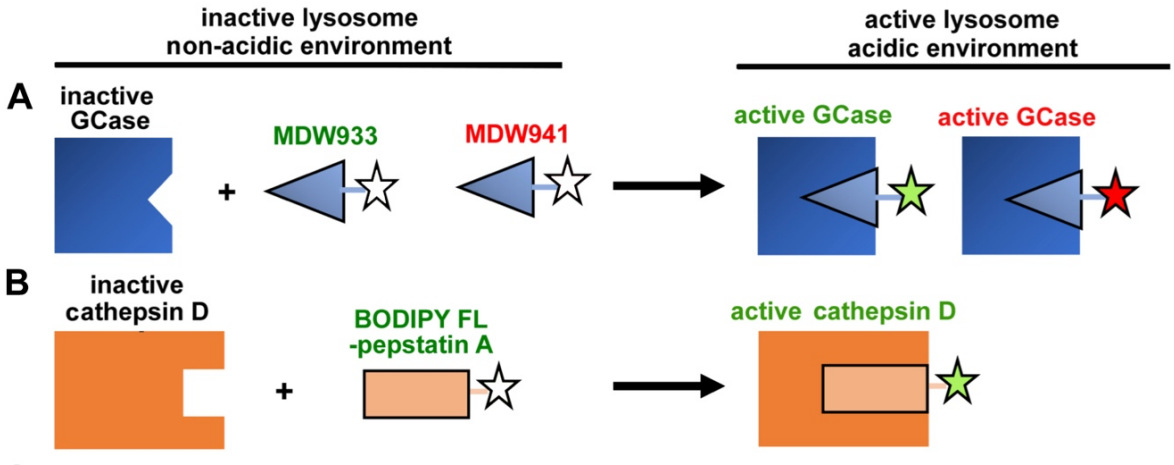


Figure 2.1 – Schematic diagram showing lysosome labeling using activity-based lysosome probes. *In non-acidic luminal pH environments, the active site of lysosomal hydrolases GCase and CTSD are not in the correct conformation to allow for probe binding and therefore remain non-fluorescent. However, in acidic luminal pH environments, acid hydrolases become active and are in the correct conformation to allow for probe binding, resulting in visualization of punctate and vesicular fluorescent signals. Cropped image taken from Farfel-Becker T et al., 2019 (135).*

2.2.3 – Plasmids

2.2.3.1 – Cloning

2.2.3.1.1 – Cloning Strategy

Recombinant DNA constructs were generated by subcloning genes of interest into desired expression vector systems using standard PCR cloning methods. Full-length transcripts were amplified using primer sequences that contained restriction site

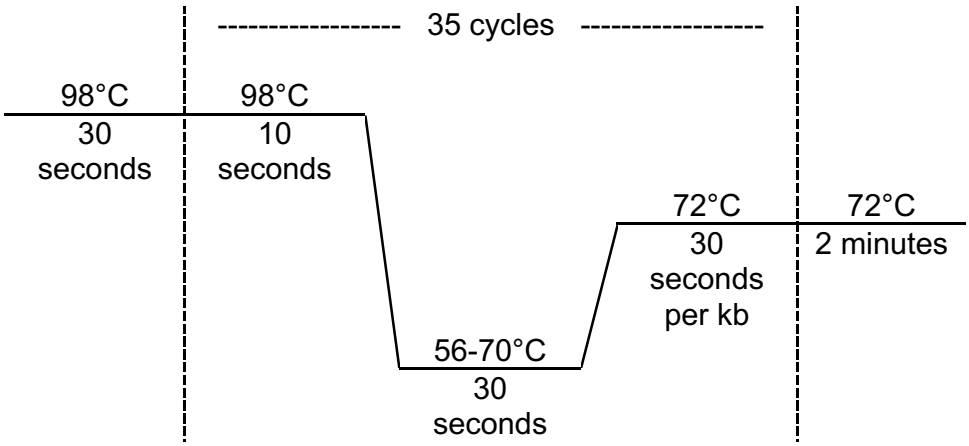
sequences on the 5' and 3' ends to allow for ligation into the final expression vector. The transcript sequence was analyzed using SnapGene software (GSL Biotech) to identify restriction sites and cross-checked with the restriction map of the desired vector to ensure that the pair of enzymes could be used for cloning without cutting the transcript. Forward primers were designed to include a Kozak sequence (GCCAAA) to increase transcription efficiency and, if necessary, additional bases were added to ensure the transcript would be read in-frame with the epitope tag in the vector. Primer sequences used for cloning are located in Appendix 1.

2.2.3.1.2 – Generation of Insert

The Q5 High-Fidelity DNA Polymerase (New England Biolabs) was used to PCR amplify genes of interest. Each reaction was set up as indicated below.

Reagent	Volume per reaction (µl)
Q5 Master Mix (5X)	10
High GC Buffer (5X)	10
dNTPs (10 mM)	1
Forward primer (10 µM)	2.5
Reverse primer (10 µM)	2.5
Template DNA (10 ng/µl)	1
Q5 High-Fidelity DNA Polymerase	0.5
Nuclease free water	22.5
TOTAL	**50**

The following amplification conditions were used to generate the insert.



2.2.3.1.3 – Gel Extraction

The entire PCR reaction was loaded on a 1% agarose gel and electrophoresed as described in section 2.2.1.2. The correct size band representing the PCR product of interest was excised from the gel, transferred to a new microcentrifuge tube, and extracted from the agarose using the QIAquick Gel Extraction kit (QIAGEN) according to the manufacturer's instructions. Briefly, three times the weight of the excised gel slice in volume of Buffer QG was added to the gel slice, then heated at 50°C until the gel was completely dissolved. One volume of isopropanol was added, and the resulting solution was applied to the QIAquick spin column, centrifuged at 13,000 x g for 1 minute at room temperature, the flow through discarded, and the column washed with 500 µl Buffer QG. To wash the bound DNA, 750 µl Buffer PE in ethanol was applied to the column, incubated at room temperature for 5 minutes, and centrifuged as before. The flow through was then discarded and centrifuged once more to remove any residual buffer. The column was then transferred to a clean microcentrifuge tube, and 20 µl

nuclease-free water was added directly onto the column. After a 3-minute incubation at room temperature, the column was centrifuged to elute the DNA into the clean tube.

2.2.3.1.4 – Restriction Digestion of Insert and Vector

The gel extracted PCR product inserts and specified vectors were restriction digested with the necessary restriction enzymes to create compatible sticky ends on both the insert and vector. The restriction enzyme combinations and buffers used are given below.

Insert	5' Enzyme	3' Enzyme	Vector	Buffer
Arl8b-mCh	NotI-HiFi	MluI-HiFi	pLEX-PGK	CutSmart
mCh	NotI-HiFi	MluI-HiFi	pLEX-PGK	CutSmart
EGFP-LC3	BsrGI	SspI	pLEX-PGK	NEBuffer 2.1

All restriction digests were carried out in 30 µl reactions and incubated at 37°C for 3 hours. The reactions were set up as indicated below.

Reagent	Amount per reaction	
	Insert	Vector
Buffer (10X)	3 µl	3 µl
5' Enzyme (10 units/µl)	1 µl	1 µl
3' Enzyme (10 units/µl)	1 µl	1 µl
DNA	20 µl	3 µg
Nuclease free water	5 µl	to 30 µl
TOTAL	**30 µl**	**30 µl**

The products of the restriction digests were then loaded on a 1% agarose gel, and the required bands were extracted as in Section 2.2.3.1.3.

2.2.3.1.5 – Ligation

To ligate the DNA insert into the desired expression vector, the following reaction was set up using the gel extracted, restriction digested insert and vector. The Ligation Calculator (NEBioCalculator, New England Biolabs) was used to calculate the amount of insert and vector required to achieve a molar ratio of 1:3 vector to insert. The T4 DNA Ligase (New England Biolabs) reaction was set up as indicated below, then incubated overnight at room temperature and stored at 4°C until needed.

Reagent	Amount per reaction
T4 DNA Ligase Buffer (10X)	1 µl
Insert DNA (1 kb)	37.5 ng
Vector DNA (4 kb)	50 ng
T4 DNA Ligase	1 µl
Nuclease free water	to 10 µl
TOTAL	**10 µl**

2.2.3.1.6 – Bacterial Transformation

Each ligation reaction (1-5 µl) was added to 50 µl DH5 alpha competent *Escherichia coli* cells (Thermo Fisher Scientific) and incubated on ice for 30 minutes. The cells were then heat shocked at 42°C for 20 seconds, immediately cooled on ice for 2 minutes, then 950 µl SOC medium (Clontech) was added to the cells. The transformed cells were then incubated at 37°C for 1 hour at 225 rpm for recovery, centrifuged at 3000 x g for 1 minute to pellet, and 750 µl of the supernatant was removed. The pellet was then gently resuspended in the remaining 200 µl and plated onto Luria-Bertani (LB) agar plates supplemented with 100 µg/mL ampicillin. The plates were then incubated upside down (agar up) at 37°C overnight.

2.2.3.1.7 – Colony Screening

Single colonies from bacterial plates were selected and transferred to 14 mL round bottom tubes containing 4 mL LB supplemented with 100 µg/mL ampicillin (LB/Amp) and grown overnight at 37°C and 225 rpm. The next day, a 20% glycerol stock was each made for a small sample of colonies and stored at -80°C until needed. The remaining culture was centrifuged at 5000 x g for 5 minutes to pellet the bacteria. Plasmids were isolated from bacterial cells using the QIAprep Spin Miniprep kit (QIAGEN) according to the manufacturer's instructions. Briefly, the bacterial pellet was resuspended in 250 µl Buffer P1 supplemented with RNase and LyseBlue reagent, then lysed in 250 µl Buffer P2 containing NaOH and SDS. The alkali was neutralized with Buffer P3, then centrifuged at 13,000 x g for 10 minutes. The supernatant was then transferred to a QIAprep spin column, centrifuged as before, and the bound DNA washed with 500 µl Buffer PB followed by 750 µl Buffer PE. The column was then centrifuged once more to remove any residual buffer, transferred to a clean microcentrifuge tube, and 50 µl nuclease free water added directly to the column and incubated for 3 minutes. The column was then centrifuged as before to elute the plasmid DNA into the new tube. A restriction digest was performed on 5 µl of the resulting plasmid DNA using the same enzymes from the original cloning step. The digested products were then run on a 1% agarose gel along with the empty vector and undigested plasmid as controls to help identify plasmids containing an insert.

2.2.3.1.8 – Plasmid Sequencing

Plasmids identified as containing gene inserts based on restriction digestion analysis were prepared as indicated on the next page and sent for sequencing through the EZ-

Seq DNA sequencing service (Macrogen). Primers were designed to cover the entire open reading frame and ligation sites using Primer 3 software (206, 207)

Reagent	Amount per reaction (in µl)
Plasmid (100 ng/µl)	5
Primer (5 pmol/µl)	5
TOTAL	**10**

2.2.3.1.9 – Plasmid Purification

After confirming the recombinant plasmid contains the gene of interest and is in frame with the epitope tag with no sequence errors, the plasmid was then amplified and purified from bacterial cells. A starter culture was prepared by inoculating 4 mL LB/Amp with bacteria from the previously prepared glycerol stock and incubated at 37°C for approximately 6 hours at 225 rpm. The starter culture was then used to inoculate 200 mL LB/Amp at a dilution of 1:500 (400 µl) and incubated overnight at 37°C with shaking at 225 rpm.

The next day, plasmids were extracted using the QIAGEN Plasmid Maxi-kit according to the manufacturer's instructions. Briefly, the bacterial suspension was centrifuged at 4000 x rpm for 30 minutes at 4°C, then the resulting pellet was resuspended in 10 mL Buffer P1 containing RNase and LyseBlue reagent. The cells were lysed in 10 mL Buffer P2 and incubated at room temperature for 5 minutes. The solution was then neutralized with 10 mL Buffer P3 and immediately transferred to the filtration column. After a 10-minute incubation, the solution was pushed through the column and collected in a new 50 mL conical tube. To remove endotoxins, 2.5 mL Buffer ER was added, and the mixture incubated on ice for 30 minutes. During this incubation, the DNA binding column was equilibrated with 10 mL Buffer QBT, then the plasmid solution was added to the

pre-equilibrated column and allowed to pass through the column. Bound DNA was washed twice with 30 mL Buffer QC and eluted with 15 mL Buffer QF to a new conical tube. The eluted DNA was precipitated with 10.5 mL isopropanol and centrifuged at 11,000 x g for 30 minutes at 4°C. The supernatant was removed, and the resulting pellet washed with 5 mL 70% ethanol and centrifuged as before but for 15 minutes. The plasmid DNA pellet was allowed to air dry, then resuspended in 500-1000 µl nuclease free water. The DNA concentration was determined using a Nanodrop instrument (Thermo Fisher Scientific).

2.2.3.2 – Plasmids Table

RESOURCE	SOURCE	IDENTIFIER
Recombinant DNA		
pCMV-EGFP-LC3	(136)	N/A
pLEX-PGK-EGFP-LC3	(135)	N/A
psPAX2	A gift from Dr. Didier Trono	Addgene plasmid #12260
pMD2.G	A gift from Dr. Didier Trono	Addgene plasmid #12259
pAdVAntage	Promega	Cat #E1711

2.2.4 – Western Blotting

2.2.4.1 – Protein Extraction

Neurons were plated on 35-mm dishes coated with 20 µg/mL poly-L-ornithine and 2.5 µg/mL laminin at a density of 2 x 10^6 cells per dish. At day *in vitro* (DIV) 7-8, cells were rinsed with cold phosphate buffered saline (PBS) and lysed in radioimmunoprecipitation assay (RIPA) buffer (50 mM Tris-HCl, pH 7.5, 150 mM NaCl, 1% Triton X-100, 0.1% SDS, 0.5% DOC) supplemented with a protease inhibitor cocktail tablet (Roche). Cell

lysates were centrifuged at 15,000 x rpm for 15 minutes at 4°C, and soluble proteins were collected.

2.2.4.2 – Protein Concentration Quantification

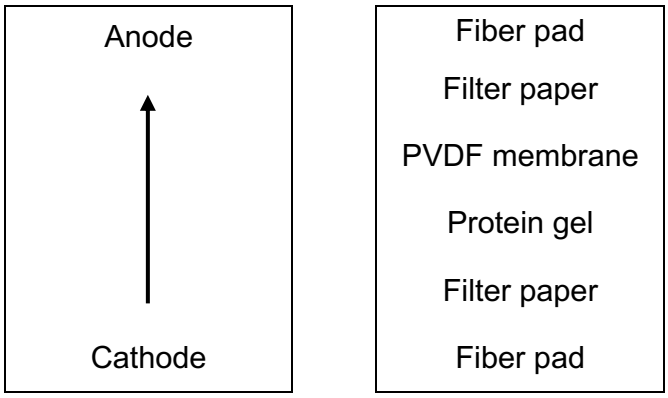
Protein concentrations were assessed using the Pierce BCA Protein Assay kit according to the manufacturer's instructions. For each assay, a 2-fold serial dilution of a 2 mg/mL BSA protein standard in RIPA buffer was made. RIPA buffer alone was also loaded as a blanking control. A Working Reagent (WR) was prepared by combining 4 µl copper (II) sulfate solution with 196 µl bicinchoninic acid solution for each protein sample. Ten microliters of either standard or sample were loaded in duplicate on a 96-well plate followed by 200 µl WR. The plate was then incubated in the dark at 37°C for 30 minutes and read on a plate reader with absorbance at 562 nm.

2.2.4.2 – SDS-PAGE

Sodium dodecyl sulfate polyacrylamide gel electrophoresis (SDS-PAGE) was carried out to separate proteins by molecular mass. Equal amounts of proteins (10 µg) containing 1X NuPAGE LDS Sample Buffer (Thermo Fisher Scientific) and 100 mM DTT were heated at 70°C for 10 minutes and resolved on NuPAGE 4-12% Bis-Tris protein gels (Thermo Fisher Scientific). A Precision Plus Dual Color molecular weight standard (Bio-Rad) was run with each protein gel so that protein sizes could be estimated. The electrophoresis was run in 1X NuPAGE MES running buffer (Thermo Fisher Scientific) for around 1 hour at 80-120 volts.

2.2.4.3 – Transfer

For immunoblotting, the SDS-PAGE separated proteins were transferred to PVDF membranes, which were first activated in methanol for 1 minute. All materials below were equilibrated in 1X NuPAGE Transfer Buffer (Thermo Fisher Scientific). The blot was created as indicated below to transfer LDS-bound negatively charged proteins from the protein gel and onto the PVDF membrane.



The transfer was performed in 1X NuPAGE Transfer Buffer at 250 mA constant current for 1.5 hours at 4°C with an ice pack and constant stirring.

2.2.4.4 – Chemiluminescent Detection

The PVDF membranes were blocked in 10% milk in TBS with 0.1% Tween 20 (TBST) for 1 hour at room temperature and incubated with primary antibodies in 5% milk in TBST overnight at 4°C. After washing four times in TBST, membranes were incubated with horseradish peroxidase (HRP)-conjugated secondary antibodies (1:5000) in 5% milk in TBST for 1 hour at room temperature. After washing four times with TBST, proteins were detected using SuperSignal chemilumescent substrates and X-ray film.

2.2.4.5 – Membrane Stripping and Re-probing

Membranes were stripped to remove primary and secondary antibodies by washing three times with TBS followed by incubation in Restore Western Blot Stripping Buffer for 15 minutes at room temperature. After three more washes with TBS, chemiluminescent detect was carried out as before in Section 2.2.4.4.

2.2.4.6 – Densitometry Analysis

Western blot X-ray films were scanned and imported into ImageJ. The intensity of each band was calculated, and the band intensity of the protein of interest was normalized to β-actin, which was used as a loading control.

2.2.5 – Primary Neuronal Cultures

2.2.5.1 – Embryonic Cortical

For cortical neurons, embryos from heterozygote breedings were obtained at embryonic day 18-19 and stored in ice-cold Hibernate medium supplemented with 2% B27 and antibiotics while genotyping was performed to identify WT and *Npc1*$^{-/-}$ embryos. Following identification, cortical neurons were prepared as previously described (208). Briefly, brains were dissected out and transferred to HBSS supplemented with HEPES and antibiotics. After removing the brain stem and diencephalon from the cerebral hemispheres, meninges and blood vessels were peeled away from the cerebrum and hippocampi were removed. The cerebrums were then collected and digested in papain supplemented with DNase (Worthington) for 45 minutes at 37°C with brief gentle agitation every 10 minutes. After digestion, neurons

were carefully triturated, centrifuged at 1400 x rpm for 5 minutes, re-suspended in ovomucoid inhibitor solution containing DNase (Worthington), and incubated at room temperature for 10 minutes to allow undissociated tissue to settle. The supernatant was then layered on a discontinuous density gradient composed of albumin and trypsin inhibitor solution (Worthington), centrifuged at 1400 x rpm for 10 minutes, and re-suspended in pre-warmed Neurobasal media supplemented with supplemented with 10% FBS, 2% B27, 0.5 mM GlutaMAX, 55 μM 2-mercaptoethanol, and 25 μg/mL insulin and maintained at 37°C and 5% CO_2.

2.2.5.2 – Adult Dorsal Root Ganglion

For doral root ganglion (DRG) neurons, WT and *Npc1*$^{-/-}$ littermates at postnatal day 30-40 (P30-40) were anesthetized with 2.5% avertin and transcardially perfused with ice-cold perfusion buffer to remove blood, reduce protease/metabolic toxicity, and improve cell survival. After bisecting the spinal canal to expose the spinal cord, DRGs were removed and transferred to HBSS supplemented with HEPES and antibiotics. After excess dorsal roots were trimmed off, DRGs were digested in 2.5 units/mL dispase II and 200 units/mL collagenase at 37°C for 30 minutes followed by 35 minutes gently rotating at room temperature. After filtering debris with a 70μm nylon strainer, neurons were collected and plated on coverslips coated with 20 μg/mL poly-L-ornithine and 10 μg/mL laminin.

2.2.6 – Basic Neuron Nucleofection

Exogenous plasmid DNA was introduced into DRG neurons using a Nucleofector device (Lonza) and Basic Neuron Small Cell Number (SCN) Nucleofector kit (Lonza)

according to the manufacturer's specifications. Briefly, approximately 2-5 x 10^4 DRGs were re-suspended in 16.4 µl Basic Neuron SCN Nucleofector Solution and 3.6 µl SCN Supplement with 0.4 µg plasmid DNA, transferred to an SCN cuvette, then nucleofected using SCN Basic Neuro Program 6. Immediately after, 300 µl of pre-equilibrated Neurobasal-A media supplemented with 2% B27, 0.5 mM GlutaMAX, and 2.5% fetal bovine serum was added and incubated at 37°C and 5% CO_2 for recovery. DRGs were then plated on 12-mm coverslips coated with 20 µg/mL poly-L-ornithine and 10 µg/mL laminin. DRG neurons were maintained at 37°C and 5% CO_2, and media was one-half changed three hours after plating.

2.2.7 – Microfluidic Device Preparation and Culture

Microfluidic chambers were prepared as previously described (138). Briefly, SYLGARD 184 silicone elastomer base was combined with its corresponding curing agent at a ratio of 10:1. After mixing and de-foaming, the silicone elastomer was poured into a silicon wafer template made out of SU-8 by photolithography. Following desiccation for 2.5 hours to remove air bubbles, the wafer was heated at 80°C for 2 hours to cure. Then, the silicone elastomer was carefully removed from the wafer and chambers were punched out following template guides. The microfluidic chambers were then adhered to coverslips prior to neuron culture.

For culture in microfluidic devices, 2 x 10^5 freshly dissociated cortical neurons in a volume of 10 µl were added directly to the soma/dendritic transwell. If necessary, for lentiviral transduction, 5 µl of the desired lentivirus was combined with 2 x 10^5 freshly dissociated neurons in a volume of 5 µl, and this 10 µl volume was then added directly to the soma/dendritic transwell. To equilibrate, 10 µl of media was added directly to the

axon transwell. Following a 10-minute incubation, 200 µl of media was added to the axon chamber followed by 180 µl of media to the soma/dendritic chamber. After a one-fourth media change at DIV1, media was one-fourth changed every three days.

2.2.8 – Immunostaining

Neurons were plated on poly-L-ornithine-coated 12-mm coverslips in 24-well plates at a density of 0.2 x 10^6 cells per well or in microfluidic devices as indicated above. At DIV7-8, neurons were quickly rinsed in PBS then fixed with either 4% paraformaldehyde (PFA) with 4% sucrose or Bouin's solution with 4% sucrose for 15 minutes at room temperature. Cells were then washed three times with PBS, permeabilized and blocked with 0.4% saponin, 1% BSA, and 5% goat serum in PBS for 1 hour, and incubated with primary antibodies in 0.1% saponin, 1% BSA, and 5% goat serum in PBS overnight at 4°C. After primary antibody labeling, cells were washed three times with PBS then incubated with Alexa Fluor conjugated secondary antibodies for 30 minutes at room temperature. After washing four times with PBS, coverslips were mounted with anti-fade mounting medium while neurons in microfluidic devices were transferred to low fluorescence Hibernate medium prior to imaging.

2.2.9 – Transmission Electron Microscopy

Samples for transmission electron microscopy (TEM) were prepared as previously described (186) with minor modifications. Briefly, mice were anesthetized and transcardially perfused with freshly made EM fixative (2% glutaraldehyde and 2% paraformaldehyde in 0.1 N cacodylate buffer). Tissues were removed and post-fixed in EM fixative overnight, then sent to the NINDS EM Facility for staining and silver

enhancement. After dehydration, embedding, and sectioning, images were taken using a JEOL 1200EX electron microscope.

2.2.10 – Image Acquisition and Analysis

Confocal images were acquired using a Zeiss LSM880 confocal microscope with a 40x/1.3 NA oil immersion objective. All images of endogenous proteins from a given experiment were taken on the same day using the same settings and analyzed using the same threshold. Image analyses were performed using ImageJ. For quantification of axonal autophagosome density, the number of EGFP-LC3 puncta was manually counted and normalized by axon length. For quantification of axonal lysosome density, the lysosome channel was segmented to identify bona fide lysosome vesicles. The fill holes and watershed functions were then applied, and the number of lysosomes was detected using the analyze particles function and normalized by axon length. For quantification of lysosomal integrated density in the cell body, the lysosome channel was segmented, and raw fluorescent intensity values were retrieved by redirecting the binary mask to the original 16-bit grayscale image. Mean integrated density values were calibrated to the area of the cell body and normalized to WT.

2.2.11 – Live-neuron Imaging and Motility Analysis

For live-cell imaging, neurons were transferred to low fluorescence Hibernate medium supplemented with 2% B27 and 0.5 mM GlutaMax. Cells were visualized with a 40x/1.3 NA oil immersion objective on a Zeiss LSM880 confocal microscope. Time lapse imaging was performed in an incubation chamber maintained at 37°C. To quantify motility, kymographs were generated using an ImageJ plugin as previously described

(Kang JS, Cell 2008). Organelles were considered stationary if the net displacement was ≤ 10 μm during the entire acquisition period. If the net displacement was ≥ 10 μm throughout this period, the organelle was considered motile in its corresponding direction.

2.2.12 – Statistical Analyses

Statistical analyses were carried out using GraphPad Prism 8 software. For comparison between two groups, the Student's *t* test (sample size n ≥ 30) or Mann-Whitney test (sample size n < 30) was used. For comparison between three or more groups, one-way ANOVA was used. All data are expressed as mean ± SEM. Differences were considered statistically significant at a value of $p < 0.05$.

2.3 – Results

2.3.1 – Axonal Autophagic Stress in *Npc1*$^{-/-}$ Mice at Presymptomatic Stages

Previous studies demonstrated that *Npc1*$^{-/-}$ neurons display axonal pathology characterized by the accumulation of various membranous organelles (39, 44, 51). These axonal alterations precede symptom onset in *Npc1*$^{-/-}$ mice, suggesting early pathological features contributing to neurodegeneration. To characterize the nature of these accumulating organelles, we first examined their composition in dorsal root and cortical axons from symptomatic *Npc1*$^{-/-}$ mice corresponding to postnatal day 50-60 (P50-60), representing two regions vulnerable to neurodegeneration in *Npc1*$^{-/-}$ mice (43, 50). Using transmission electron microscopy (TEM), we observed a striking buildup of endocytic and autophagic organelles within dystrophic axons consisting primarily of multivesicular bodies, multilamellar vesicles, and autophagic vacuoles (AVs) (**Figure 2.2**). Notably, the majority of autophagosomes in *Npc1*$^{-/-}$ swollen axons exhibited features of early stage initial autophagic vacuoles (AVi) characterized by a double-membrane bilayer containing electron-lucent material, while fewer late autophagic vacuoles in the degradative stage (AVd) following fusion with lysosomes (73) were observed. Importantly, these axonal phenotypes were not found in age-matched wild type (WT) mice. Such unique organelle accumulations largely represent intermediates of the endo-lysosomal-autophagic pathways, indicating defects in their trafficking and maturation in *Npc1*$^{-/-}$ distal axons.

We next aimed to better understand the dynamic events that might underlie AV accumulation by assessing their distribution in neuronal axons cultured from presymptomatic *Npc1*$^{-/-}$ mice corresponding to P30-40. To address this, we used dorsal root ganglion (DRG) neurons because (1) they displayed *in vivo* axonal organelle

accumulation; (2) represent a rigorous model amenable to isolation and culture from adult mice in our previous studies (135, 136, 138, 186); and (3) almost all neurites are tau-positive axons with uniformly polarized microtubules with plus ends oriented outward to allow for directional analyses of kinesin- and dynein-driven organelle transport along axons (158). DRG neurons isolated from presymptomatic *Npc1*$^{-/-}$ mice were nucleofected with autophagosome marker EGFP-LC3 at DIV0 followed by live imaging at DIV3-4. Only distal axons with uniform diameter were selected for live imaging. In WT axons, EGFP-LC3 appeared mostly diffuse as cytosolic LC3I (**Figure 2.3A**). However, in *Npc1*$^{-/-}$ axons, EGFP-LC3 was more punctate as lipidated LC3II incorporated into autophagosome membranes. Strikingly, *Npc1*$^{-/-}$ axons showed a robust increase in autophagosome density compared to control (**Figure 2.3B**; WT: 1.02 ± 0.18; *Npc1*$^{-/-}$: 9.21 ± 0.69; $p < 0.0001$; per 100 μm axon length), reflecting axonal autophagic stress in adult presymptomatic *Npc1*$^{-/-}$ mice.

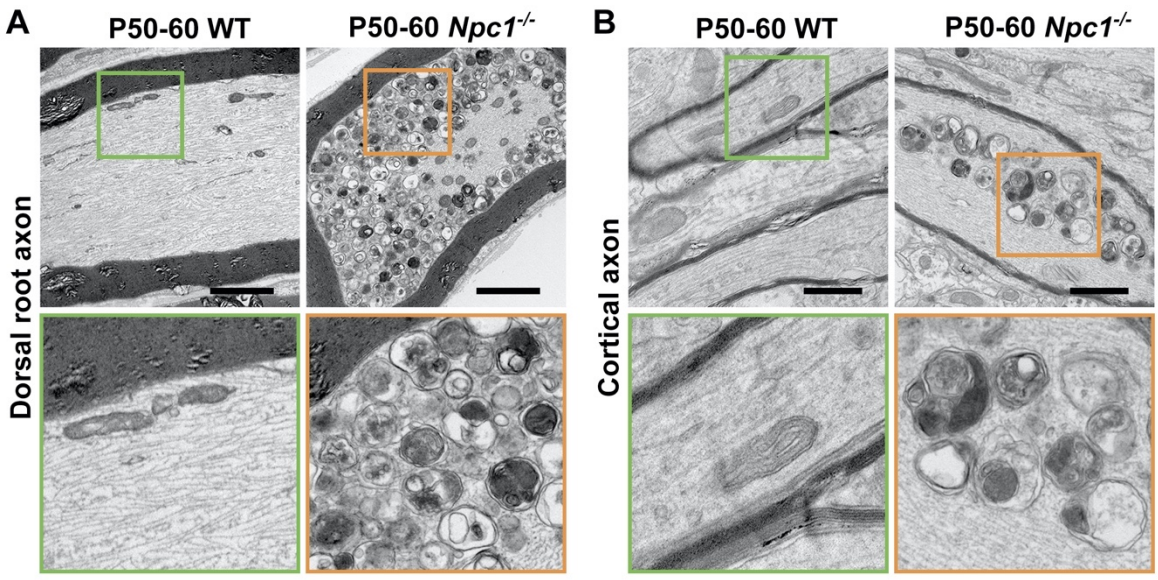


Figure 2.2 – Axonal organelle accumulation in symptomatic Npc1$^{-/-}$ mice.
*(**A, B**) Representative TEM images showing accumulation of endocytic and autophagic organelles in DRG (**A**) and cortical (**B**) axons in Npc1$^{-/-}$ mice at symptomatic stages (P50-60). Such accumulations were not readily observed in age-matched WT mice. Note the presence of many early stage initial autophagic vacuoles (AVi) characterized*

by a double-membrane bilayer with low electron density in Npc1$^{-/-}$ axons. Colored boxes represent four-fold higher magnification of corresponding region in upper panels (green: WT; orange: Npc1$^{-/-}$). Scale bars: 800 nm. Experiment carried out in collaboration with Y. Xie (NINDS, NIH) and support from V. Crocker and S. Cheng (NINDS Electron Microscopy Facility).

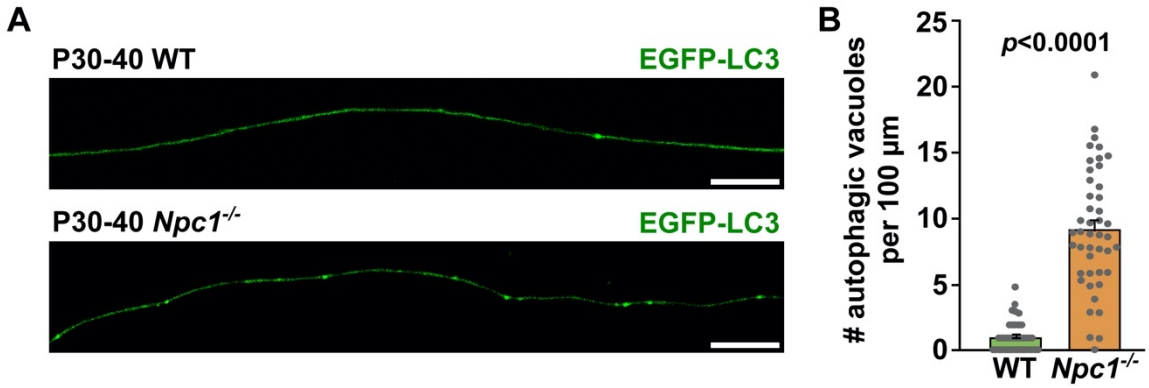


Figure 2.3 – Axonal autophagic stress in presymptomatic Npc1$^{-/-}$ mice.
*(**A, B**) Representative images (**A**) and quantitative analysis (**B**) showing a robust increase in autophagosome density in DRG axons isolated from presymptomatic (P30-40) Npc1$^{-/-}$ mice compared to WT neurons at the same age. DRG neurons were nucleofected with EGFP-LC3 at DIV0, followed by live imaging at DIV3-4. Data are presented as mean ± SEM with dots representing individual axons (WT n=45, Npc1$^{-/-}$ n=40) and analyzed by Student's t test. Scale bars: 10 µm.*

Because most axonal autophagosomes form distally and exhibit predominant retrograde transport towards the soma for degradation (136, 142, 158), we hypothesized that autophagosome accumulation in *Npc1$^{-/-}$* distal axons may reflect defects in their retrograde motility. To test this, we monitored autophagosome trafficking in axons from live DRG neurons cultured from P30-40 mice. In WT neurons, EGFP-LC3-labeled axonal autophagosomes moved predominantly (57.63 ± 7.35%) in the retrograde direction (**Figure 2.4**), consistent with previous studies (136, 142, 158, 159). However, contrary to our hypothesis, axonal autophagosomes in *Npc1$^{-/-}$* neurons displayed similar motility patterns compared to WT control, suggesting that increased autophagosome density in *Npc1$^{-/-}$* axons does not result from defects in their retrograde

transport at this presymptomatic stage. Our findings instead indicate defects in the capacity of axonal autophagosomes to achieve effective maturation and clearance during their retrograde trafficking in presymptomatic *Npc1*$^{-/-}$ axons.

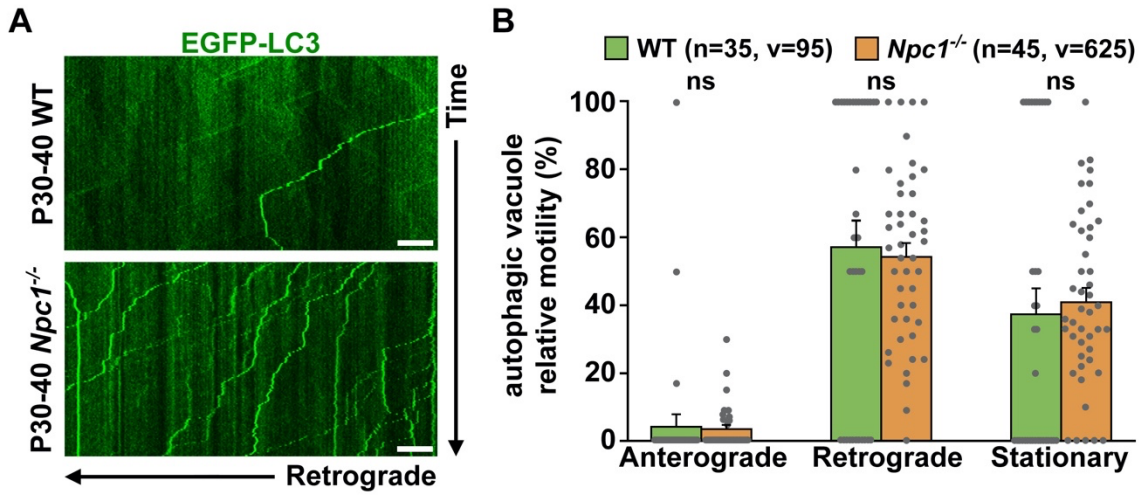


Figure 2.4 – No change in autophagosome motility in presymptomatic Npc1$^{-/-}$ axons.

*(**A, B**) Representative kymographs (**A**) and quantitative analysis (**B**) showing no significant differences in the relative motility of axonal autophagosomes between WT and Npc1$^{-/-}$ DRG neurons under basal conditions. DRG neurons were isolated from presymptomatic Npc1$^{-/-}$ mice, nucleofected with EGFP-LC3 at DIV0, followed by live imaging at DIV3-4. Note that the majority of autophagosomes undergo retrograde transport toward the soma. Data were collected from the total number of vesicles (v) from the total number of axons (n) indicated in parentheses, presented as mean ± SEM with dots representing individual axons, and analyzed by Student's t test. Scale bars: 10 µm.*

2.3.2 – Reduced Lysosome Density in *Npc1*$^{-/-}$ Distal Axons

Lysosomes contain acid hydrolases required for endocytic and autophagic cargo degradation. Since the majority of autophagosomes in *Npc1*$^{-/-}$ dystrophic axons represent immature AVi-like structures, we next asked whether axonal lysosome distribution is altered in DRG neurons cultured from P30-40 *Npc1*$^{-/-}$ mice. Given that the membrane protein LAMP1 is distributed among a heterogenous population of endocytic

and autophagic organelles (147), we used LAMP1 along with an activity-based lysosome probe to monitor degradative lysosomes in axons. We first examined axonal lysosome distribution by labeling active glucocerebrosidase (GCase) using MDW933, a fluorescent activity-based probe that binds specifically to the active site of the lysosomal hydrolase GCase under acidic conditions (204, 205). Strikingly, *Npc1*$^{-/-}$ neurons showed an approximately six-fold decrease in the number of active lysosomes positioned along axons relative to age-matched WT neurons (**Figures 2.5A and 2.5B**; WT: 15.02 ± 1.50; *Npc1*$^{-/-}$: 2.27 ± 0.48; $p < 0.0001$; per 100 μm axon length), representing a significant reduction in the relative lysosomal degradative capacity in *Npc1*$^{-/-}$ distal axons. Since activity-based lysosome probes depend on enzymatically active hydrolases for its fluorescent reporting, we next tested whether this reduction resulted from decreased lysosome positioning in distal axons by examining LAMP1-labeled total endolysosomes. Notably, *Npc1*$^{-/-}$ axons displayed a two-fold reduction in the total number of endolysosomes compared to WT littermates (**Figures 2.5C and 2.5D**; WT: 17.75 ± 1.37; *Npc1*$^{-/-}$: 8.41 ± 1.35; $p < 0.0001$; per 100 μm axon length), reflecting a decrease in endolysosome density in *Npc1*$^{-/-}$ axons at this presymptomatic stage.

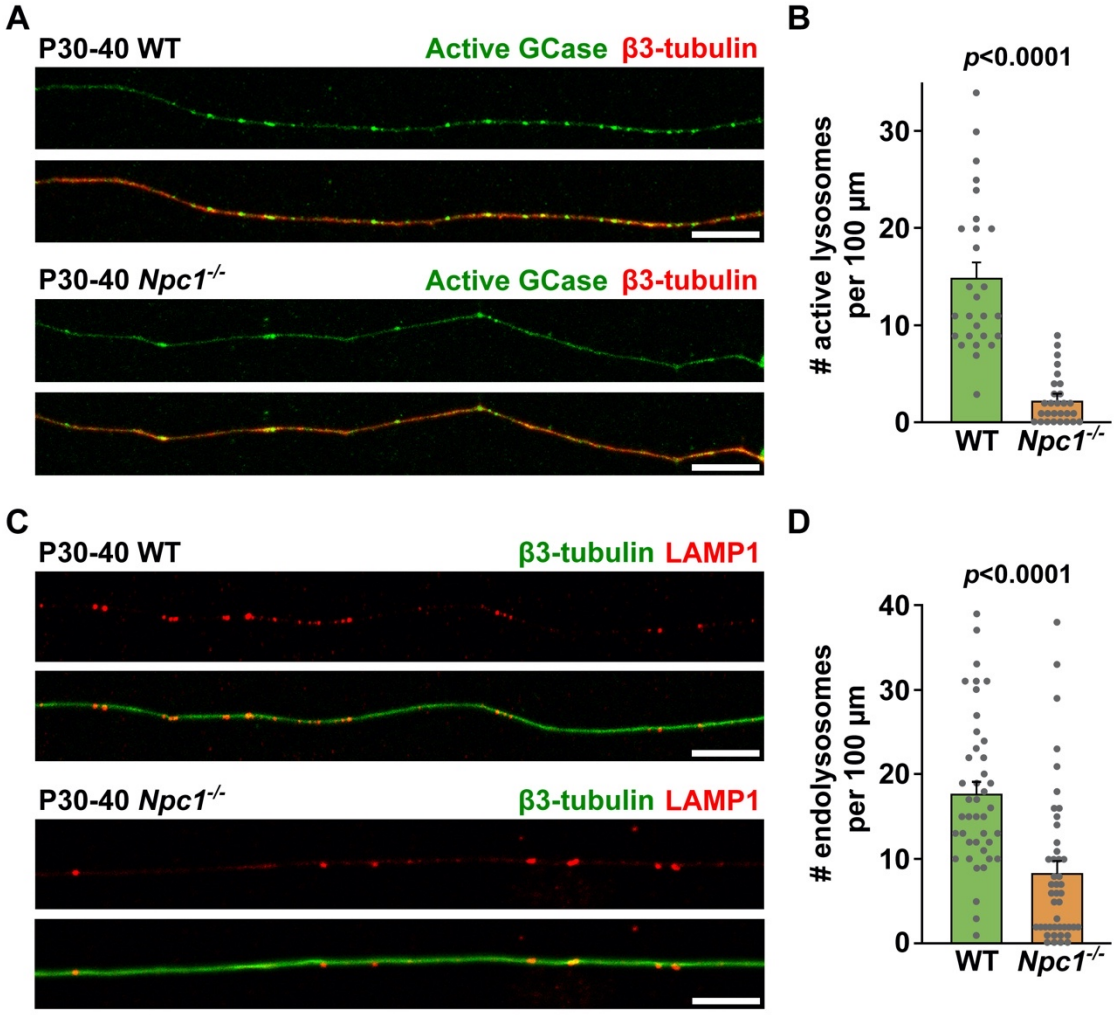


Figure 2.5 – Reduced density of endolysosomes and degradative lysosomes in DRG axons from presymptomatic Npc1$^{-/-}$ mice.

*(**A-D**) Representative images (**A, C**) and quantitative analyses (**B, D**) showing reduced density of both endolysosomes and degradative lysosomes in adult DRG neuron axons isolated from presymptomatic Npc1$^{-/-}$ mice. DRG neurons isolated from P30-40 mice were incubated with MDW933 (500 nM) for 1 hour to label active GCase, followed by immunostaining for β3-tubulin or directly co-immunostaining for LAMP1 and β3-tubulin. Data are presented as mean ± SEM with dots representing individual axons (**B:** WT n=27, Npc1$^{-/-}$ n=28; **D:** WT n = 45, Npc1$^{-/-}$ n = 45) and analyzed by Mann-Whitney test (**B**) or Student's t test (**D**). Scale bars: 10 µm.*

These findings raise a question as to whether decreased lysosome density along axons in *Npc1*$^{-/-}$ DRG neurons could be also detected in central nervous system (CNS) neurons. To address this, we examined cortical neurons cultured in microfluidic devices that physically and fluidically separate axons from neuronal cell bodies and dendrites by an array of narrow 450-μm long microgrooves (135, 209, 210). Cortical neurons were plated in the soma/dendritic chamber and by 5 days *in vitro* (DIV5), only axons that enter the microgrooves extend far enough to grow into the axon chamber, thus allowing analysis of lysosomes in distal axons. Using this system, we observed that lysosome density was also reduced in *Npc1*$^{-/-}$ cortical axons with an approximately two-fold decrease in the number of degradative lysosomes labeled with active lysosome probe MDW933 (**Figures 2.6A and 2.6B**; WT: 13.49 ± 1.0; *Npc1*$^{-/-}$: 6.32 ± 0.57; $p < 0.0001$; per 100 μm axon length) and total endolysosomes labeled by LAMP1 (**Figures 2.6C and 2.6D**; WT: 18.18 ± 1.34; *Npc1*$^{-/-}$: 8.64 ± 0.87; $p < 0.0001$; per 100 μm axon length) compared to WT neurons. These results demonstrate that reduced axonal lysosome density occurs at early stages of disease progression in embryonic CNS neurons.

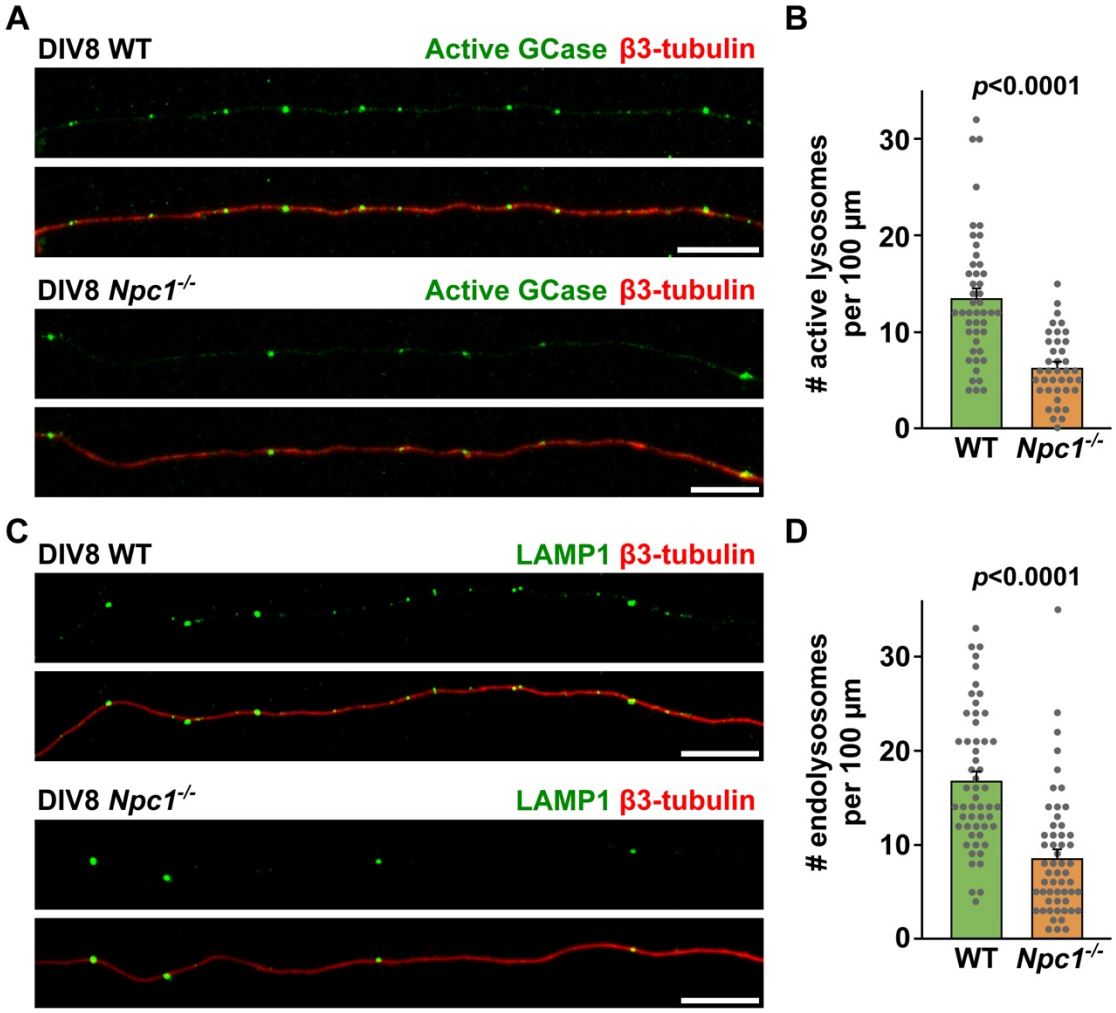


Figure 2.6 – Reduced density of endolysosomes and degradative lysosomes in axons from Npc1$^{-/-}$ cortical neurons.

*(**A-D**) Representative images (**A, C**) and quantitative analyses (**B, D**) showing reduced density of both endolysosomes and degradative lysosomes in axons of Npc1$^{-/-}$ cortical neurons. Cortical neurons were plated in microfluidic chambers to allow physical and fluidic separation of axons from neuronal cell bodies and dendrites. At DIV8, neurons were loaded with MDW933 (500 nM) for 1 hour to label active GCase-positive lysosomes and immunostained for β3-tubulin, or co-immunostained for LAMP1 and β3-tubulin. Note the similar reduction in axonal lysosome density using two independent lysosomal markers. Data are presented as mean ± SEM with dots representing individual axons (**B:** WT n=46, Npc1$^{-/-}$ n=39; **D:** WT n=56, Npc1$^{-/-}$ n=55) and analyzed by Student's t test. Scale bars: 10 µm.*

2.3.3 – Lysosomes Accumulate in Cell Bodies of *Npc1*$^{-/-}$ Cortical Neurons

To determine whether fewer lysosomes in *Npc1*$^{-/-}$ axons reflected an overall reduction in neuronal lysosome levels, we next examined lysosomes in the soma. Notably, *Npc1*$^{-/-}$ neurons exhibited increased integrated density of MDW933 ($p < 0.0001$) and LAMP1 ($p < 0.0001$) in the cell body relative to control (**Figure 2.7**), indicating that reduced axonal lysosome density in *Npc1*$^{-/-}$ neurons is not due to decreased lysosome biogenesis. We also examined total protein levels of GCase and LAMP1 in cortical neurons at DIV7 and found no differences between *Npc1*$^{-/-}$ and WT (**Figure 2.8**). In addition, filipin staining to detect unesterified cholesterol showed that *Npc1*$^{-/-}$ neurons, but not WT neurons, store cholesterol (**Figures 2.9**), consistent with a cellular phenotype of NPC. Taken together, these results suggest that the lower number of degradative lysosomes in *Npc1*$^{-/-}$ axons may reflect an altered mechanism that impairs lysosome trafficking and/or positioning in axons.

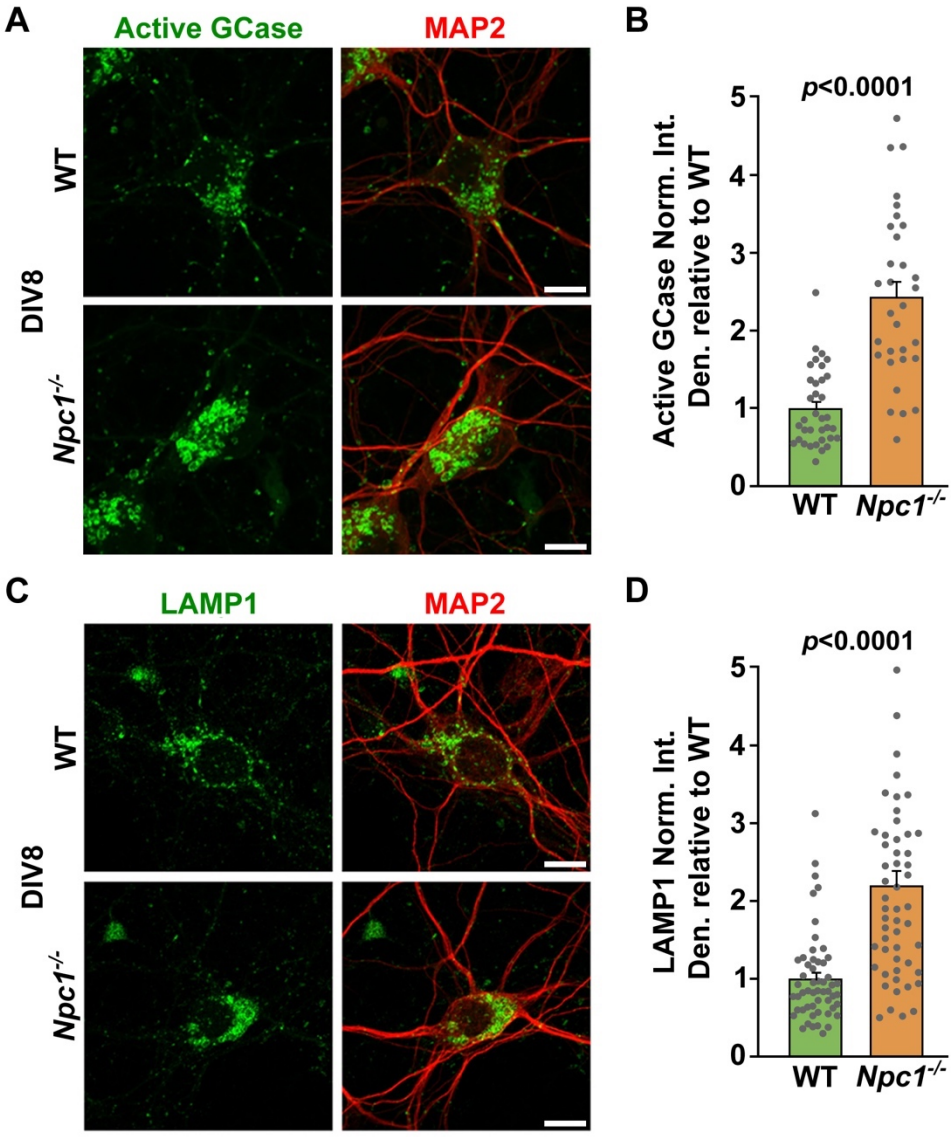


Figure 2.7 – Lysosomes accumulate in cell bodies of Npc1$^{-/-}$ cortical neurons. *(**A-D**) Representative images (**A, C**) and quantitative analyses (**B, D**) showing lysosomal accumulation in the soma of Npc1$^{-/-}$ cortical neurons. Neurons at DIV8 were incubated with MDW933 and immunostained for MAP2 or co-immunostained for LAMP1 and MAP2. Integrated density was measured in thresholded images using ImageJ. Data were collected from the total number of neurons shown within bars and presented as mean integrated density normalized to WT neurons. Data are presented as mean ± SEM with dots representing individual neurons (**B:** WT n=34, Npc1$^{-/-}$ n=31; **D:** WT n=54, Npc1$^{-/-}$ n=52) and analyzed by Student's t test. Scale bars: 10 µm.*

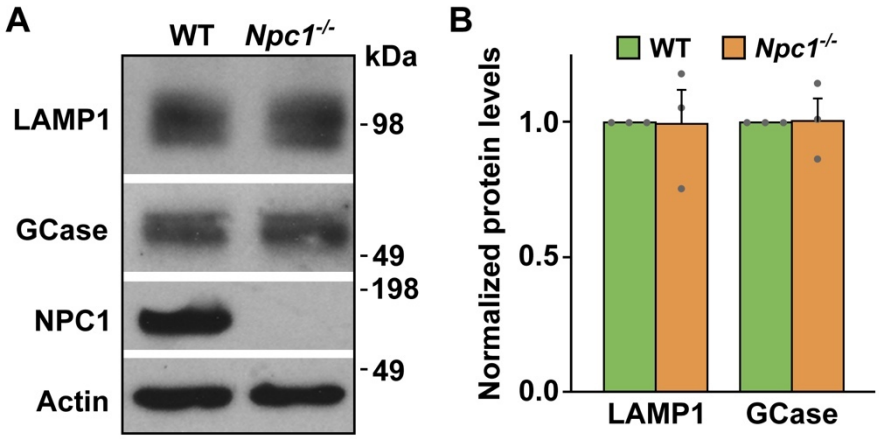


Figure 2.8 – No change in total lysosome protein levels in cultured Npc1$^{-/-}$ cortical neurons.

*(**A, B**) Immunoblots (**A**) and quantitative analysis (**B**) showing no detectable changes in total protein levels of GCase and LAMP1 between cultured WT and Npc1$^{-/-}$ cortical neurons at DIV7-8. Equal amounts of cell lysates (10 µg) were sequentially immunoblotted on the same membrane after stripping between each primary antibody. Protein band intensities were quantified and averaged from three biological replicates. Data are presented as mean ± SEM with dots representing each repeat and analyzed by Student's t test. Experiment carried out in collaboration with M. Lin (NINDS, NIH).*

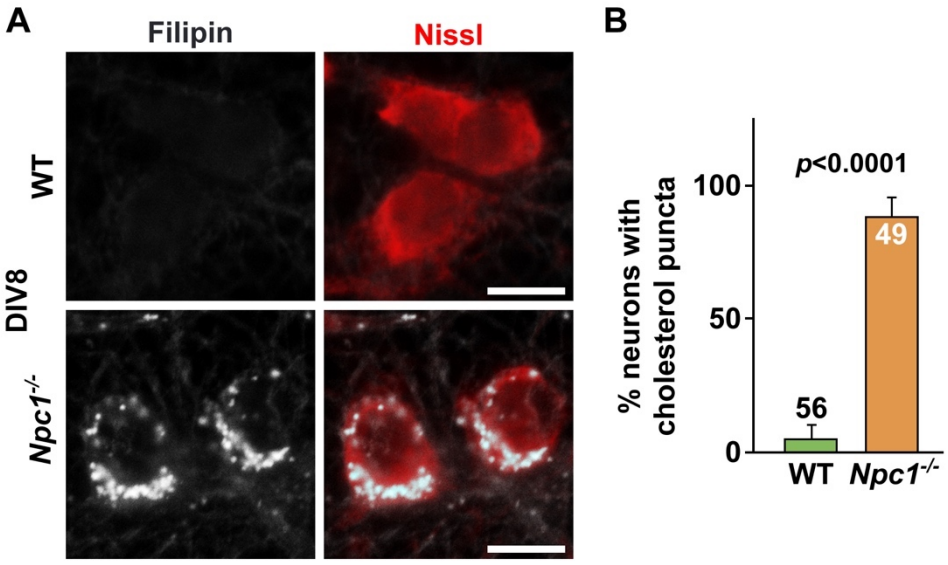


Figure 2.9 – Cholesterol storage in Npc1$^{-/-}$ cortical neurons.

*(**A, B**) Representative images (**A**) and quantitative analysis (**B**) showing aberrant accumulation of cholesterol within endolysosomes in cell bodies of Npc1$^{-/-}$ cortical neurons. Neurons were stained with filipin (50 µg/ml) to detect unesterified cholesterol followed by Nissl staining to identify neuronal cell bodies. Note that nearly all Npc1$^{-/-}$*

neurons store cholesterol inside endolysosomes at DIV7-8, which is not readily detected in WT neurons. Data were collected from the total number of neurons indicated above or within bars, presented as mean ± SEM, and analyzed by Student's t test. Scale bars: 10 μm.

2.4 – Discussion

Here, we show that endocytic and autophagic organelles predominantly accumulate within dystrophic axons in NPC mice, and find that autophagosome accumulation in NPC axons does not result from defects in their retrograde transport at presymptomatic stages. Instead, we observe a robust decrease in the number of lysosomes positioned in axons, reflecting a significant reduction in the relative lysosomal degradation capacity in NPC axons. Fluorescence microscopy analysis of the cell body revealed increased integrated density of endolysosomal proteins in NPC relative to WT, while western blot showed no change in total levels of these proteins between the genotypes. Collectively, these results indicate that reduced axonal lysosome density in NPC does not result from an overall reduction in neuronal lysosome levels but suggests a change in lysosome distribution (**Figure 2.10**).

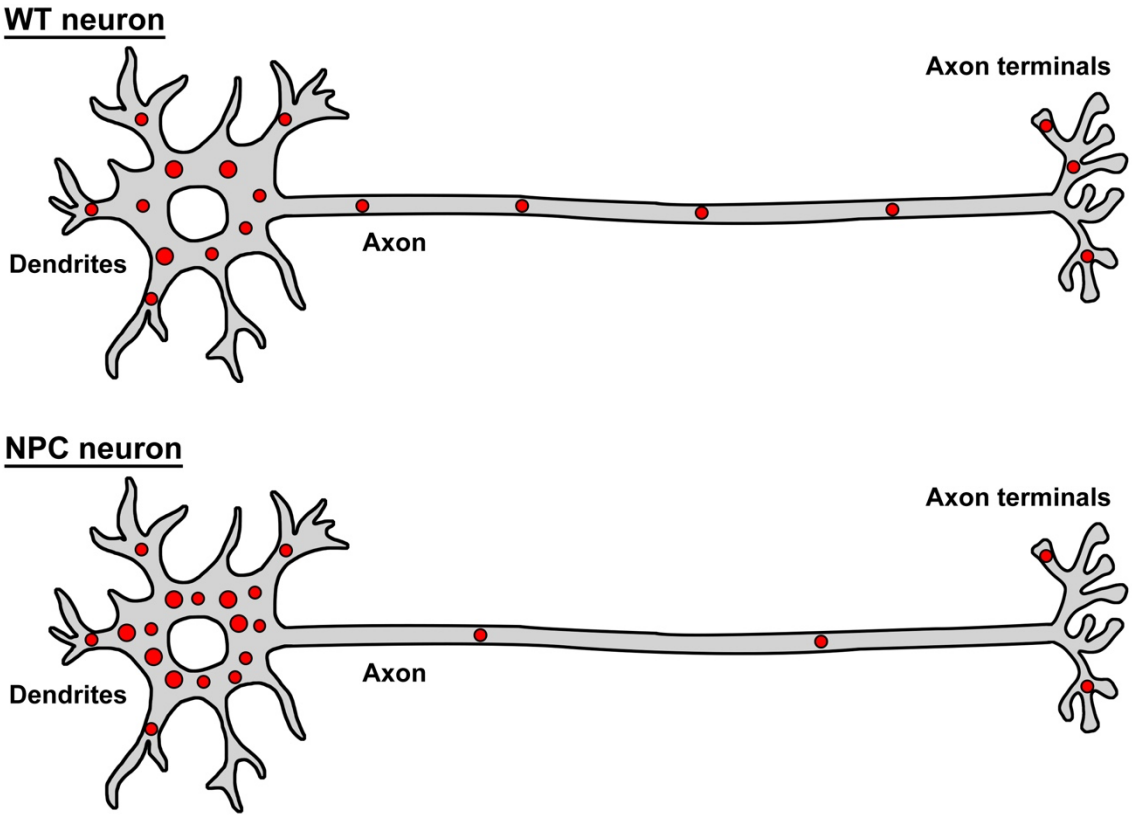


Figure legend on next page.

Figure 2.10 – Schematic diagram showing altered lysosome distribution in axons of Npc1$^{-/-}$ neurons. *In WT neurons, lysosomes are distributed along axons and enriched in the cell body. However, in Npc1$^{-/-}$ neurons, lysosome density in axons is reduced with an expanded lysosomal system in the cell body.*

Axonal dystrophy and autophagic stress are two major pathological hallmarks of common neurodegenerative diseases and LSDs associated with impaired lysosome function (44, 139, 142, 186-193). These studies raised a fundamental question as to whether reduced turnover or clearance of lysosomal substrates contributes to axon pathology. Since degradative lysosomes have been thought to be confined to the neuronal cell body, it was unclear why a disturbance in lysosomal function would be associated with cellular pathology in distal axons in neurodegenerative LSDs such as NPC (44).

In agreement with previous reports (39, 44, 51), dystrophic axons in NPC did not contain the characteristic lysosome inclusions representative of NPC lysosomes. Rather, we observed a predominant accumulation of multivesicular bodies, multilamellar vesicles, and autophagic vacuoles, largely representing intermediates of the endocytic and autophagic pathways. It has been well established that the retrograde transport of axonal autophagosomes is linked to their maturation and degradation (136, 142, 158). One of our most unexpected observations was that autophagosome accumulation in presymptomatic NPC axons did not reflect a defect in their retrograde transport. Despite increased axonal autophagic stress, we were surprised to find that autophagosomes in NPC axons showed similar motility patterns compared to control axons, predominantly moving in the retrograde direction towards the cell body. This prompted consideration of other scenarios in which axonal autophagosome density may be increased. Given global disruptions to axonal transport would lead to

accumulation of a more diverse set of organelles, our findings suggested that impaired maturation and clearance of lysosomal substrates likely underlies early axonal pathology in NPC.

Reduced lysosomal degradation by leupeptin or bafilomycin A1 treatment was previously observed to result in an accumulation of autophagosomes in axons, neurites, and/or the soma (142, 211, 212). These studies suggest that impaired lysosomal proteolytic function may also contribute to autophagic stress in NPC axons. Indeed, previous studies linked autophagosome accumulation in NPC cells to a block in autophagic flux, which was suggested to result from reduced lysosome degradation capacity with prolonged autolysosome lifespan (213), while in other studies to impaired autophagosome-lysosome fusion with intact proteolytic function (37, 214). Studies in brains from *Npc1*$^{-/-}$ mice demonstrated autophagosome accumulation (215) that was later revealed to be mTOR-independent (216), suggesting increased autophagosome levels may not result from autophagy induction in the brain. Interestingly, a recent study in NPC cats reported accumulation of LC3-positive puncta and aggregates in axons and presynaptic terminals but not in the neuronal cell body or dendrites (217), further highlighting the importance of lysosome distribution and function to maintain axonal autophagic flux and degradation capacity in axons.

Our findings suggest that progressive accumulation of lipid storage within the lysosomal lumen of NPC neurons alters lysosome degradative capacity at presymptomatic stages but seems to remain intact at embryonic stages. We observed reduced lysosome density in axons but an expanded lysosomal system in the cell body using both LAMP1 and an activity-based lysosome probe in embryonic NPC cortical neurons at DIV7-8. However, in adult presymptomatic NPC DRG neurons, decreased axonal lysosome

density was associated with altered lysosome distribution and a further reduction in active lysosome density was noted. Collectively, these results suggest that both lysosome positioning and function in distal axons are important to support axonal health.

CHAPTER 3 – MECHANISMS CONTRIBUTING TO IMPAIRED AXONAL LYSOSOME POSITIONING IN NPC

3.1 – Introduction

Given their highly polarized morphology, neurons require efficient transport mechanisms to maintain a steady-state distribution of lysosomes throughout the cell. While enzymatically active degradative lysosomes are relatively enriched in the cell body, their trafficking to and positioning at distal axons have recently been observed (135, 143). Axonal lysosomes are highly dynamic and move bidirectionally along microtubules through the coordinated activities of kinesin and dynein motor proteins. Because axonal microtubules are uniformly polarized with plus-ends oriented outward, kinesin motors mediate lysosome movement towards distal growth cones whereas dynein motors mediate movement back towards the cell body (**Figure 3.1**). To ensure a homeostatic supply of axonal lysosomes, a balance between their anterograde and retrograde transport is required.

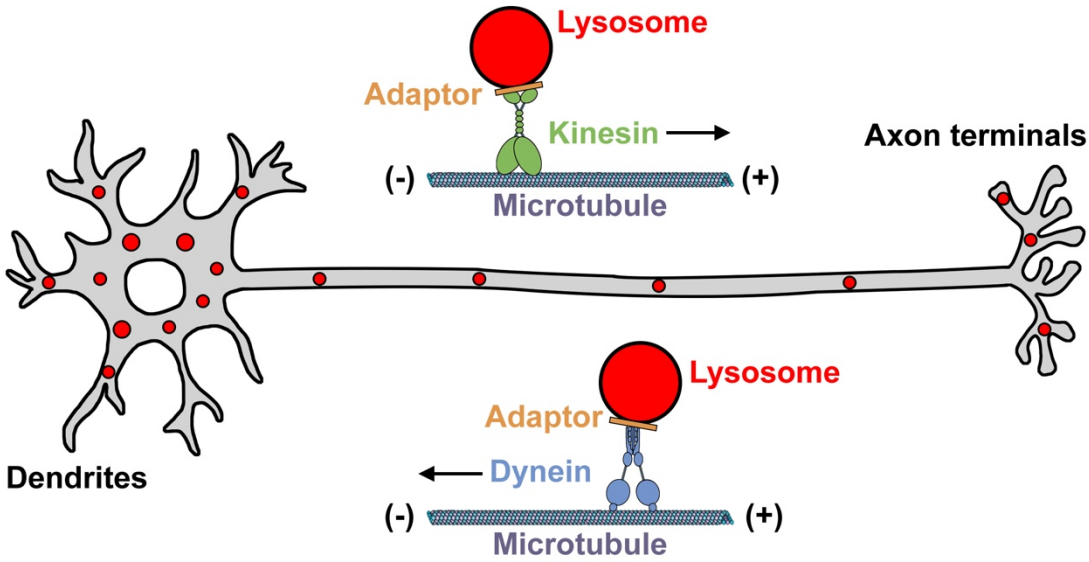


Figure 3.1 – Schematic diagram of neuronal lysosome distribution. *Kinesin and dynein motors are recruited to lysosomes through interactions with motor-adaptor proteins to enable microtubule-based lysosome movement. Note that kinesin motors mediate transport towards axon terminals whereas dynein motors facilitate axonal lysosome movement towards the cell body.*

Mechanisms controlling lysosome movement studied in non-neuronal cells have recently been investigated in neurons. Notably, the BORC-Arl8-SKIP-kinesin-1 complex was discovered to drive anterograde lysosome transport specifically into axons but not dendrites (**Figure 3.2**) (143). BORC is a multiprotein complex that associates with the cytosolic face of lysosomes and is required for recruitment of the small GTPase Arl8 from the cytoplasm (106). The Arl8 effector SKIP then binds Arl8 and links lysosomes to kinesin-1 motors (107). This mechanism drives lysosome transport into axons, and interference with multiple components of the complex selectively impairs axonal lysosome availability (143). Moreover, our previous study demonstrated that soma-derived lysosomes are continuously delivered to distal axons and target to autophagic cargo and axonal growth cones (135). Depleting lysosomes from axons by targeted knockdown of the small GTPase Arl8 results in axonal autophagic stress and abnormal growth cone morphology (135, 143). These observations highlight the importance of small GTPases in the regulation of lysosome transport and positioning in distal axons.

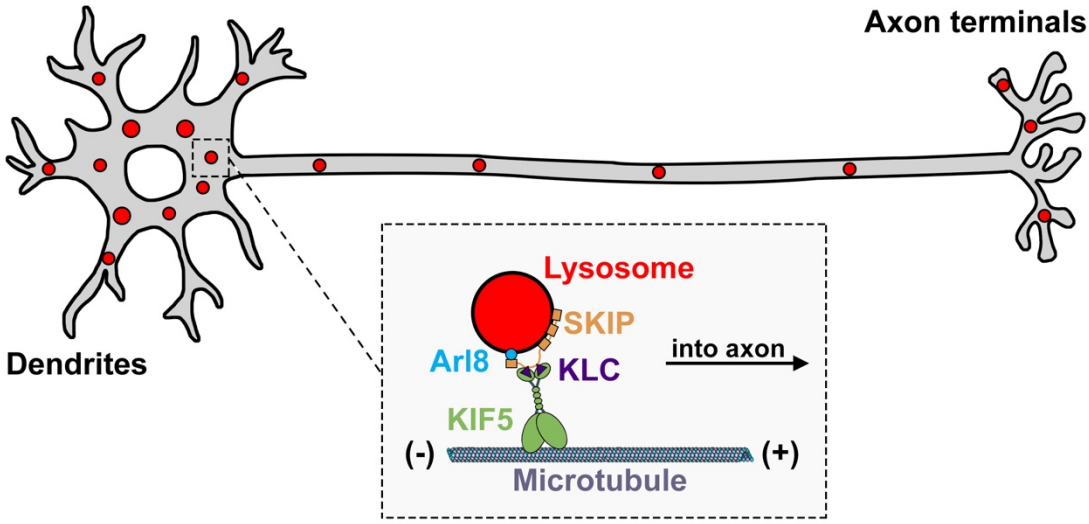


Figure 3.2 – Schematic diagram of the Arl8-SKIP-kinesin-1 axonal lysosome transport complex. *This complex mediates lysosome transport into the axon but not dendrites (143).*

Altered small GTPase function triggered by abnormal cholesterol accumulation was previously observed in NPC cells. Endolysosomal cholesterol storage resulted in increased levels of membrane associated Rab7 and Rab9 through interference with their GDP-GTP cycle (218, 219). Notably, recent structural analyses of the yeast orthologue of NPC1 known as Niemann-Pick type C-related protein 1 (Ncr1) revealed a hydrophobic tunnel within Ncr1 that moves cholesterol and other sterols from the lysosomal lumen to the inner leaflet of the limiting membrane, where they may diffuse to the outer leaflet for transfer to other cellular membranes (220). This structural model is consistent with the observation that NPC1-deficient lysosomes accumulate cholesterol within the lysosomal lumen. Interestingly, it was recently reported that NPC lysosomes also accumulate ER-derived cholesterol at the lysosomal limiting membrane (221), which may be distinguished from cholesterol derived from an endocytic source. However, the pathological relevance of cholesterol accumulation in NPC neurons and whether this contributes to axonal dystrophy and autophagic stress in axons remain largely unknown.

In this chapter, we investigate pathological mechanisms underlying altered lysosome distribution in NPC axons using live-neuron and STED super-resolution imaging combined with biochemical and pharmacologic approaches.

3.2 – Materials and Methods

3.2.1 – Lentivirus Production and Transduction

Lentiviral constructs were generated by sub-cloning genes of interest into the pLEX vector under the expression of the PGK promoter. For packaging and production, Lenti-X 293T cells were transfected with the desired lentiviral construct, the packaging plasmid psPAX2 (Addgene #12260), the envelope plasmid pMD2.G (Addgene #12259), and pAdVAntage for enhanced protein expression. Media was changed every 24 hours and collected at 48- and 72-hours post-transfection. Following centrifugation to remove cell debris, lentivirus-containing media was aliquoted and stored at -80°C until use.

For culture in microfluidic devices where lentiviral transduction was needed, 5 µl of the desired lentivirus was combined with 2 x 10^5 freshly dissociated neurons in a volume of 5 µl, and this 10 µl volume was then added directly to the soma/dendritic transwell. To equilibrate, 10 µl of media was added directly to the axon transwell. Following a 10-minute incubation, 200 µl of media was added to the axon chamber followed by 180 µl of media to the soma/dendritic chamber. After a one-fourth media change at DIV1, media was one-fourth changed every three days.

3.2.2 – Super-resolution STED Imaging

STED super-resolution imaging was performed as previously described (138). Neurons were plated on 25-mm poly-L-ornithine-coated coverslips in 6-well plates and processed for immunostaining as in Section 2.2.8. A Leica TCS SP8 inverted STED 3X microscope with a resolution of ~50-90 nm was used. Alexa Fluor 488 was excited by a tunable white light laser (70% of maximum power) at 470 nm (10%) with

the STED depletion laser at 592 nm (30% of the maximum power); its fluorescence at 480-560 nm was collected using time-gated detection (1.5-6.5 nsec). Alexa Fluor 594 was excited by the tunable white light laser at 594 nm (10%) with the STED depletion laser at 660 nm (30% of the maximum power); its fluorescence between 600-640 nm was collected using time-gated detection (1.5-6.5 nsec). GST-D4H*-mCherry was excited by the tunable white light laser at 587 nm (10%) with the STED depletion laser at 660 nm (50% of the maximum power); its fluorescence between 600-640 nm was collected using time-gated detection (1.5-6.5 nsec).

3.2.3 – Recombinant GST-D4H*-mCherry Protein Purification

Recombinant GST-D4H*-mCherry proteins were purified as previously described (221) with minor modifications. GST-D4H*-mCherry (Addgene #134604) was expressed in BL21(DE3) *Escherichia coli* (Thermo Fisher Scientific) and grown to an optical density at 600 nm (OD_{600}) of ~0.6. Protein production was then induced with IPTG at a final concentration of 0.4 mM and grown for 20 hours at 18°C. The bacterial pellet was resuspended in lysis buffer (20 mM Tris-Cl pH 8.0, 0.1 M NaCl, 1 mM DTT) supplemented with a protease inhibitor cocktail tablet (Roche) and incubated with end-over-end rotation at 4°C for 30 minutes. The bacterial lysate was sonicated on an ice-cold water bath with a 5 second pulse at 30% amplitude followed by a 10 second break for a total of 15 minutes. Cleared lysate containing soluble protein was incubated with pre-equilibrated Glutathione Sepharose 4B beads (GE Healthcare) for 2 hours at 4°C with end-over-end rotation. GST-D4H*-mCherry proteins were eluted with 25 mM reduced L-glutathione in 50 mM Tris-Cl pH 8.8 and 200 mM NaCl, then sequentially filtered using 3kDa and 30kDa molecular weight cutoff centrifugal filter units (Millipore) to concentrate the protein in 50 mM Tris-Cl pH 8.0 and 5 mM DTT. Following supplementation with sucrose to a final concentration of 0.5 M, the

GST-D4H*-mCherry protein solution was aliquoted, frozen in liquid nitrogen, and stored at -80°C until use.

3.2.4 – Detecting Luminal and Membrane Cholesterol with Filipin and D4H*

Luminal and membrane cholesterol were labeled as previously described (**Figure 3.3**) (221, 222) with minor modifications. Neurons were plated on poly-L-ornithine-coated 12-mm coverslips in 24-well plates at a density of 0.2 x 10^6 cells per well. At DIV7-8, cells were quickly rinsed in PBS, then fixed with 4% PFA with 4% sucrose for 15 minutes at room temperature. The coverslips were washed three times with PBS, then submerged in liquid nitrogen for 30 seconds to permeabilize the plasma membrane while leaving intracellular membranes intact. Cells were blocked with 1% BSA in PBS for 1 hour, then incubated with recombinant GST-D4H*-mCherry (1:100) in 1% BSA in PBS for 2 hours at room temperature. The cells were quickly rinsed twice in PBS, re-fixed with 4% PFA with 4% sucrose for 10 minutes at room temperature, blocked with 1% BSA in PBS for 1 hour at room temperature, and incubated with a LAMP1 primary antibody overnight at 4°C. Cells were then washed three times with PBS, and incubated with an Alexa Fluor 488 conjugated secondary antibody for 30 minutes at room temperature. After washing three times with PBS, cells were incubated with 50 µg/mL filipin (Sigma-Aldrich) in PBS for 40 minutes at room temperature followed by three more washes in PBS. The coverslips were then mounted with anti-fade mounting medium.



Figure legend on next page.

Figure 3.3 – Schematic diagram of in situ cholesterol labeling assay. *Adapted directly from Lim CY et al., 2019 (221).*

3.2.5 – Magnetic Isolation of Lysosomes

Lysosomes were isolated as previously described (223, 224) (**Figure 3.4**) with minor modifications. Neurons were plated on poly-L-ornithine- and laminin-coated 10-cm culture dishes at a density of 10 x 10^6 cells per dish. The day before isolation, conditioned neuronal media was collected by removing 10 mL media from each 10-cm dish. Cells were then treated with 1 mL DexoMAG iron-dextran solution (10 mg/mL) for 20 hours, washed with PBS, and cultured for an additional 2 hours in conditioned neuronal media collected from the day before. Cells were gently scraped and washed three times in cold PBS, then lysed using a 25 G needle in cold SCA buffer (20 mM HEPES-KOH, pH 7.5, 10 mM KCl, 1.5 mM $MgCl_2$, 1 mM EDTA, 1 mM EGTA, 250 mM sucrose) supplemented with 1 mM DTT, 1 mM Pefabloc, benzonase nuclease, and a protease inhibitor cocktail tablet. Ruptured cells were centrifuged at 800 x *g* for 5 minutes at 4°C, then the supernatant containing cytosol and organelles was collected and this process repeated two more times, followed by loading onto pre-equilibrated MS columns fitted into the magnetic field of a MiniMACS separator attached to a MACS multistand. Columns were washed five times with SCA buffer, removed from the separator unit, and lysosomal membrane fractions were eluted with 200 µL buffer containing 5 mM Tris-HCl (pH 7.5), a protease inhibitor cocktail, and 1% Triton X-114. Protein concentration was determined using a BCA Protein Assay Kit according to the manufacturer's instructions. For immunoblots, eluted proteins were precipitated in methanol/chloroform, resuspended in LDS sample buffer with 100 mM DTT, and resolved on NuPAGE Bis-Tris protein gels.

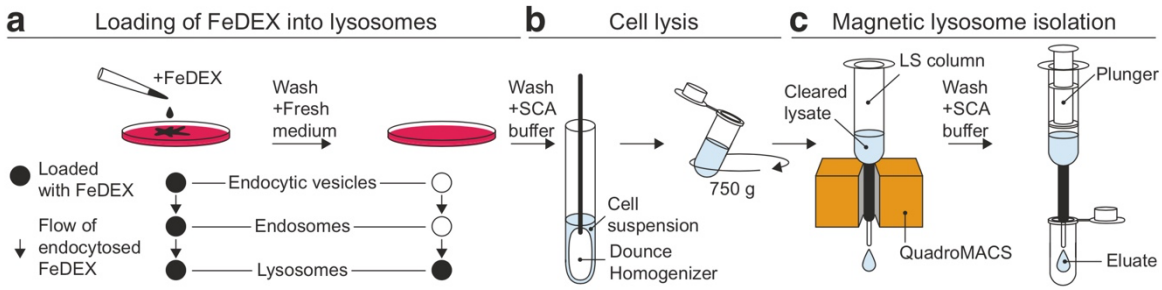


Figure 3.4 – Schematic diagram of magnetic isolation of lysosomes. *Cropped image taken directly from Bilgin M et al., 2017 (223).*

3.2.6 – Image Acquisition and Analysis

Confocal images were acquired and analyzed as in Section 2.2.10. Axonal lysosome relative motility was quantified as in Section 2.2.11. For endolysosomal membrane cholesterol quantification, the Just Another Colocalization Plugin (JACoP) (225) was used. A set threshold was applied to each LAMP1 and GST-D4H*-mCh channel to identify authentic signals, and the Manders' overlap coefficient representing the fraction of LAMP1-vesicles that were also positive for GST-D4H*-mCh was calculated. Data were normalized to a reference group as indicated in the corresponding figure legend.

3.3 – Results

3.3.1 – Impaired Anterograde Transport and Delivery of Lysosomes to Distal Axons in *Npc1*$^{-/-}$ Cortical Neurons

Our previous study revealed that soma-derived degradative lysosomes are continuously delivered from the cell body to distal axons to maintain distal degradation capacity and thus cellular homeostasis (135). Increased lysosome accumulation in cell bodies and reduced lysosome density in distal axons prompted us to ask whether lysosomes were not being delivered properly to distal axons in *Npc1*$^{-/-}$ neurons. To test this hypothesis, we loaded active GCase probe MDW941 or active cathepsin D probe BODIPY-FL-pepstatin A into the soma/dendritic chamber of neurons cultured in microfluidic devices for 30 minutes, followed by live imaging the axon chamber for a total period of 90 minutes (**Figure 3.5**). Our previous study demonstrated that these activity-based probes are fluidically restricted in the soma/dendritic chamber where they were loaded, and their dynamic influx into the axonal chamber represents microtubule-based anterograde lysosome transport (135). We observed degradative lysosomes labeled by MDW941 (**Figures 3.6A and 3.6B**) or BODIPY-FL-pepstatin A (**Figures 3.6C and 3.6D**) in distal axons after soma/dendritic chamber labeling, representing axonal lysosome delivery from the cell body. Strikingly, *Npc1*$^{-/-}$ neurons displayed significantly reduced axonal density of these soma-labeled lysosomes relative to control WT neurons at DIV7 (MDW941: 0.44 ± 0.06; BODIPY-FL-pepstatin A: 0.47 ± 0.07) and further at DIV10 (MDW941: 0.16 ± 0.03; BODIPY-FL-pepstatin A: 0.15 ± 0.03), indicating a progressive decrease in soma-derived lysosome transport to distal axons in *Npc1*$^{-/-}$ neurons.

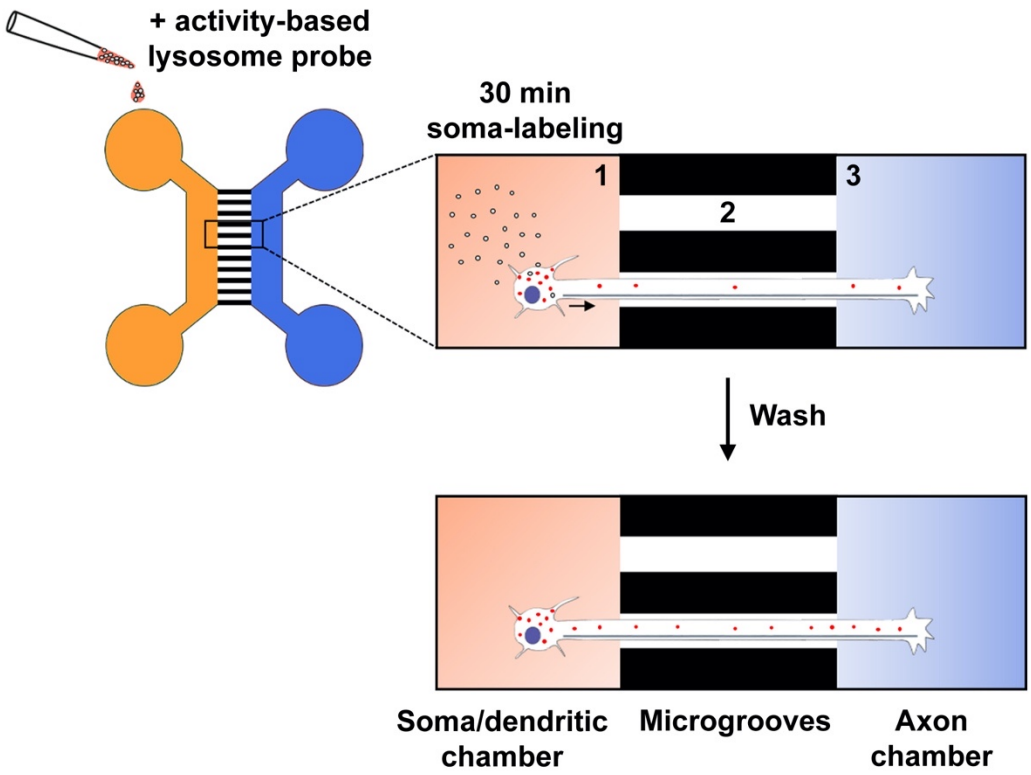


Figure 3.5 – Schematic diagram of soma-restricted labeling of degradative lysosomes and their delivery to distal axons using a microfluidic device.
Neurons are plated in the soma/dendritic chamber (1) of a microfluidic device that provides physical and fluidic separation of axons from cell bodies and dendrites. Only axons that enter the 450-μm long microgrooves (2) are able to extend far enough to grow into the axon chamber (3). The soma/dendritic chamber is loaded with an activity-based lysosome probe for 30 minutes, followed by washes with unlabeled imaging buffer and live imaging carried out in the axon chamber for 90 minutes. Degradative lysosomes visualized in distal axons after soma/dendritic chamber labeling represent those that were transported there from the cell body (135).

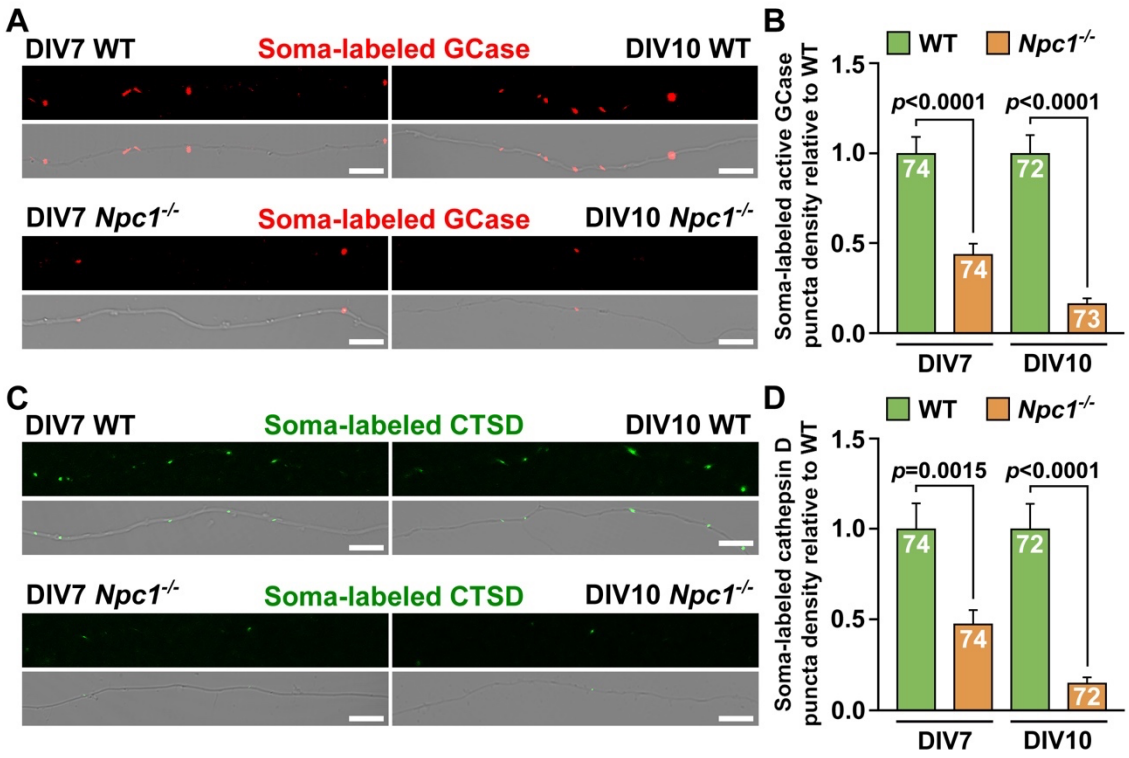


Figure 3.6 – Impaired lysosome delivery to distal axons in Npc1$^{-/-}$ neurons. *(**A-D**) Representative images (**A**, **C**) and quantitative analyses (**B**, **D**) showing impaired anterograde delivery of active GCase- and active cathepsin D (CTSD)-labeled degradative lysosomes from the soma/dendritic chamber to distal axons in Npc1$^{-/-}$ cortical neurons plated in microfluidic devices. At DIV7, the soma/dendritic chamber was loaded with MDW941 (100 nM) (**A**) or BODIPY FL-pepstatin A (1 μM) (**C**) for 30 minutes, followed by washes with imaging buffer and live imaging as described in **Figure 3.5**. Note that while soma-labeled degradative lysosomes were efficiently delivered to distal axons in WT neurons, such axon-targeted delivery progressively decreased in Npc1$^{-/-}$ neurons from DIV7 to DIV10. Data were quantified from the number of axons indicated in bars, presented as mean ± SEM, and analyzed by Student's t test. Scale bars: 10 μm. Experiment carried out in collaboration with T. Farfel-Becker (NINDS, NIH).*

To determine whether this defect in axonal lysosome delivery represents a specific impairment in anterograde transport, we next monitored lysosome motility in distal axons of live WT and *Npc1*$^{-/-}$ cortical neurons. Neurons were incubated with MDW941 for 30 minutes prior to time-lapse live imaging at DIV8. In WT neurons, degradative lysosomes exhibited bidirectional transport with motile lysosomes accounting for approximately 60% of the total lysosome pool (**Figures 3.7A and**

3.7B); of which 36.29 ± 2.41% moved in the retrograde direction, and 23.93 ± 2.74% moved anterogradely towards the distal terminal. However, lysosomes in *Npc1*$^{-/-}$ distal axons displayed reduced anterograde transport (12.59 ± 2%, $p = 0.0022$) with no significant changes in stationary or retrograde motility ($p = 0.1546$ and $p = 0.6366$, respectively). We also monitored relative lysosome motility in distal axons using BODIPY-FL-pepstatin A. Consistently, *Npc1*$^{-/-}$ neurons showed impaired anterograde lysosome transport (**Figures 3.7C and 3.7D**; WT: 33.22 ± 2%; *Npc1*$^{-/-}$: 21.6 ± 3.36%; $p = 0.0038$) but with a corresponding increase in stationary puncta (WT: 27.92 ± 2.22%; *Npc1*$^{-/-}$: 45.23 ± 3.56%; $p < 0.0001$) and no significant changes in retrograde motility ($p = 0.1019$). Taken together, these results support the notion that impaired anterograde transport contributes to reduced axonal lysosome density in *Npc1*$^{-/-}$ neurons.

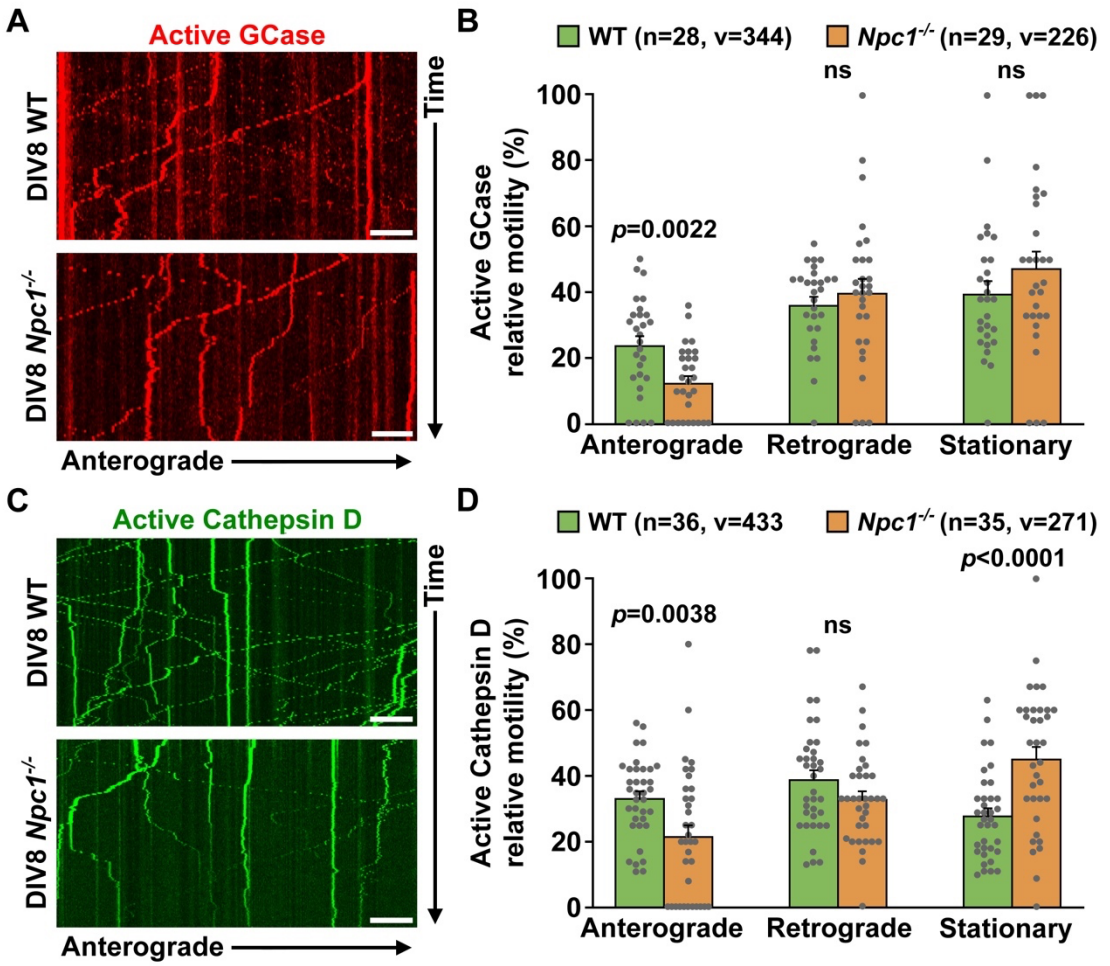


Figure 3.7 – Impaired anterograde lysosome transport in Npc1$^{-/-}$ distal axons. *(**A-D**) Kymographs (**A, C**) and quantitative analyses (**B, D**) showing impaired anterograde motility of degradative lysosomes in distal axonal segments of Npc1$^{-/-}$ cortical neurons. Neurons plated in microfluidic devices were incubated with MDW941 (100 nM) (**A, B**) or BODIPY-pepstatin A (1 μM) (**C, D**) for 30 minutes prior to live imaging at DIV8. Time-lapse images were collected every 2 seconds for 90 frames totaling 3 minutes. Relative motility was quantified from the total number of vesicles (v) from the total number of axons (n) indicated in parentheses. Data are presented as mean ± SEM with dots representing individual values and analyzed by Mann-Whitney test (**B**) or Student's t test (**D**). Scale bars: 10 μm.*

This prompted us to ask whether decreased lysosome density along axons has an impact on axonal autophagic clearance in *Npc1*$^{-/-}$ neurons. While a robust increase in autophagosomes was readily detected in DRG axons isolated from presymptomatic (P30-40) *Npc1*$^{-/-}$ mice (**Figures 2.2A and 2.2B**), it is unclear whether embryonic *Npc1*$^{-/-}$ cortical neurons also display axonal autophagic stress.

To address this, neurons cultured in microfluidic devices were transduced with a lentivirus encoding EGFP-LC3 at DIV0 followed by live imaging at DIV8 and DIV10. We found no significant differences in the density of EGFP-LC3-labeled autophagosomes in *Npc1*$^{-/-}$ axons at DIV8 (**Figures 3.8A and 3.8B**), a time point where we observed lysosome density already reduced (**Figures 2.5 and 2.6**). However, at DIV10, autophagosome density was significantly increased in *Npc1*$^{-/-}$ axons (WT: 2.86 ± 0.44; *Npc1*$^{-/-}$: 4.76 ± 0.62; $p = 0.0122$; per 100 µm axon length). Notably, this increase in axonal autophagosome density did not reflect changes in AV transport as no differences in their relative motility were observed (**Figures 3.9A and 3.9B**). These results indicate that lysosome transport defects precede axonal autophagosome accumulation in *Npc1*$^{-/-}$ cortical neurons, suggesting that impaired lysosome delievery to distal axons contributes to autophagic stress in *Npc1*$^{-/-}$ axons.

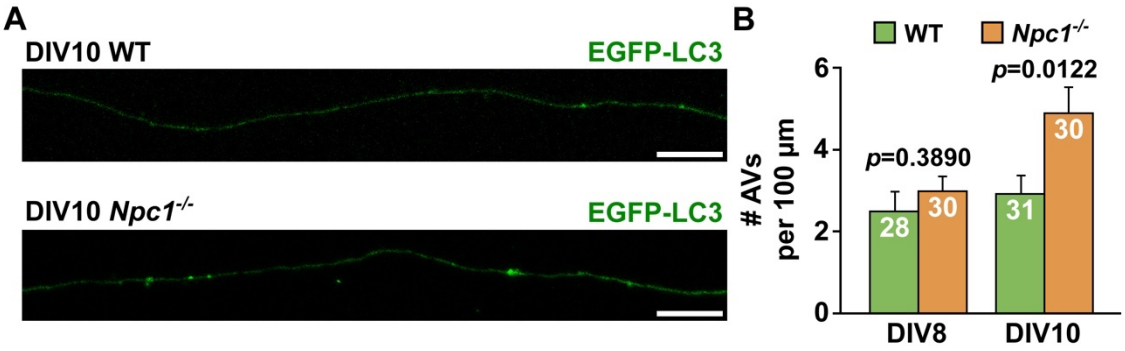


Figure 3.8 – Altered axonal autophagosome density over time in Npc1$^{-/-}$ cortical neurons.

*(**A, B**) Representative images (**A**) and quantitative analysis (**B**) showing no change in axonal autophagosome density at DIV8 but an increase at DIV10. Neurons were transduced with a lentivirus expressing EGFP-LC3 at DIV0 and live imaging was performed at DIV8 or 10. Autophagosome density was measured from the total number of axons indicated within bars, presented as mean ± SEM, and analyzed by Student's t test. Scale bars: 10 µm.*

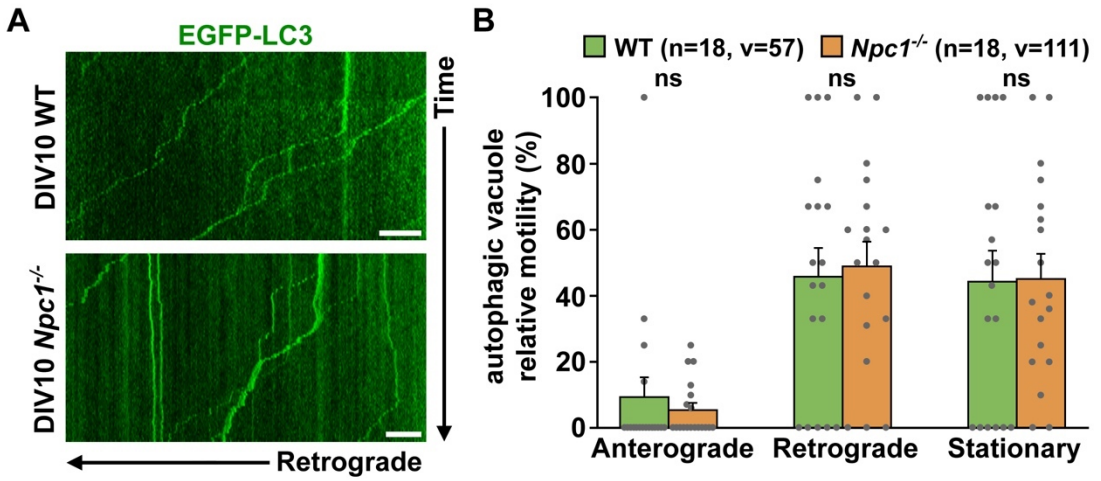


Figure 3.9 – No change in axonal autophagosome motility in DIV10 Npc1$^{-/-}$ cortical neurons.

*(**A, B**) Kymographs (**A**) and quantitative analysis (**B**) showing no changes in autophagosome motility at DIV10 in Npc1$^{-/-}$ cortical axons. Neurons transduced with a lentivirus expressing EGFP-LC3 were plated in microfluidic chambers at DIV0 and live imaging was performed at DIV10. Time-lapse images were collected every 2 seconds for 90 frames totaling 3 minutes. Motility data was collected from the total number of vesicles (v) from the total number of axons (n) shown in the graph. Data are presented as mean ± SEM with dots representing individual values and analyzed by Mann-Whitney test. Scale bars: 10 µm.*

3.3.2 – Aberrant Sequestration of Arl8 and kinesin-1 on *Npc1*$^{-/-}$ Lysosome Membranes

Our studies in *Npc1*$^{-/-}$ neurons established a defect in lysosome delivery to distal axons leading to axonal autophagic stress. These findings prompted us to examine potential mechanisms underlying impaired anterograde axonal transport of soma-derived lysosomes in *Npc1*$^{-/-}$ neurons. It is well established that lysosome transport is driven by functional interactions between motor proteins and their adaptors to enable microtubule-based transport (90, 226). The small GTPase Arl8b links lysosomes to the anterograde motor kinesin-1 (KIF5) through its effector SKIP, and this motor-effector-adaptor (kinesin-1-SKIP-Arl8b) complex was previously shown to drive lysosome anterograde transport specifically into axons (143). Therefore, we

hypothesized that these complexes might be improperly recruited to *Npc1*$^{-/-}$ neuronal lysosomes as a potential mechanism underlying defective axonal lysosome delivery. To test this hypothesis, we applied stimulated emission and depletion (STED) super-resolution microscopy to examine the localization of kinesin-1, SKIP, and Arl8 on lysosomes. Unexpectedly, we observed that both endogenous kinesin-1 and Arl8 appear abundantly recruited to and accumulated on the surface of LAMP1-labeled endolysosomes in the cell body of *Npc1*$^{-/-}$ cortical neurons (**Figures 3.10A and 3.10B**). In contrast, both Arl8 and kinesin-1 were largely dispersed throughout the soma of WT neurons. Notably, the Arl8b effector SKIP did not show similarly enhanced lysosomal membrane association in *Npc1*$^{-/-}$ neurons (**Figure 3.10C**), indicating that kinesin-1 was not recruited to *Npc1*$^{-/-}$ neuronal lysosomes by the GTPase effector SKIP and thus may represent a non-functional anterograde transport complex. These results suggest that the sequestration of motor-adaptor proteins on *Npc1*$^{-/-}$ lysosomal membranes may contribute to impaired axonal lysosome delivery.

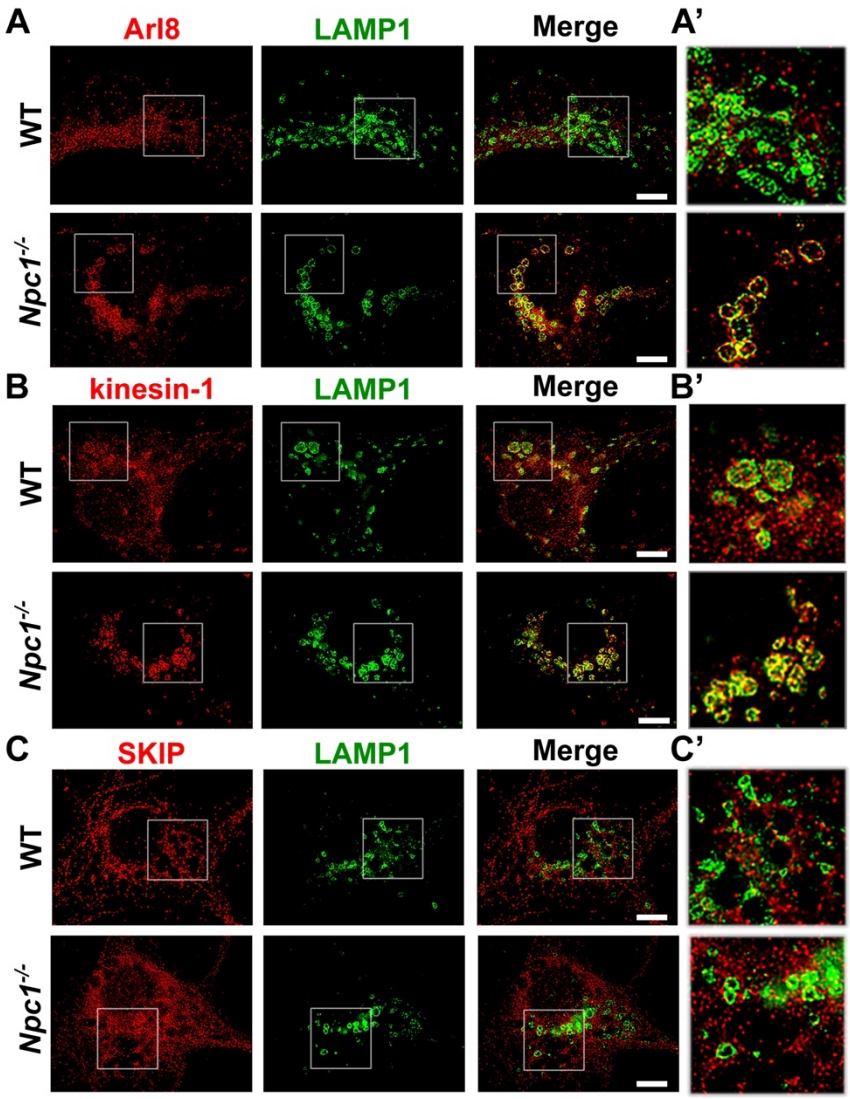


Figure 3.10 – STED super-resolution imaging reveals aberrant sequestration of Arl8 and kinesin-1 on lysosome membranes in Npc1$^{-/-}$ neurons.

(A-C) *Representative STED super-resolution images showing phase sequestration of endogenous kinesin-1 and its adaptor Arl8 on the surface of Npc1$^{-/-}$ lysosome membranes. WT and Npc1$^{-/-}$ cortical neurons at DIV8 were co-immunostained with antibodies against LAMP1 and Arl8 (**A**), kinesin-1 (**B**), or the Arl8 effector SKIP (**C**). Enlarged views of the boxed region are shown in (**A'**), (**B'**) and (**C'**), respectively. Note that Arl8 and kinesin-1 appear abundantly stabilized on Npc1$^{-/-}$ lysosomal membranes whereas SKIP does not show similarly enhanced membrane association. Experiment carried out in collaboration with S. Li (NINDS, NIH).*

3.3.3 – Elevated Lysosomal Membrane Cholesterol Sequesters Kinesin-1 and Arl8

Our STED super-resolution imaging data prompted us to further examine membranes of *Npc1*$^{-/-}$ neuronal lysosomes. Notably, a recent study established that the limiting membrane of *Npc1*$^{-/-}$ lysosomes in non-neuronal cells shows significant cholesterol accumulation (221). To determine whether *Npc1*$^{-/-}$ neurons also show elevated membrane cholesterol levels, we applied the cholesterol biosensor GST-D4H*-mCherry to semi-permeabilized cells. This semi-permeabilization method was reported to disrupt the plasma membrane while leaving organelle membranes largely intact (221), which allows the D4H* protein to bind intracellular membranes (222) with a cholesterol molar content that exceeds 10% (227). In addition, we co-labeled lysosomal luminal cholesterol with filipin. Whereas filipin binds free cholesterol, GST-D4H*-mCh selectively binds cholesterol-rich membranes (228). In WT neurons, recombinant D4H*-mCherry appeared mostly diffuse and did not bind LAMP1-labeled endolysosomal membranes (**Figure 3.11A**), indicating that their membrane cholesterol content is below 10%. However, *Npc1*$^{-/-}$ neurons showed strong vesicular D4H*-mCherry signals overlapping LAMP1-positive endolysosomes, indicating elevated cholesterol content on lysosomal membranes in *Npc1*$^{-/-}$ neurons compared to WT (**Figures 3.11A and 3.11B**; $p = 0.0008$). Moreover, *Npc1*$^{-/-}$ neurons also showed increased luminal cholesterol levels relative to WT (**Figures 3.11A and 3.11C**; $p < 0.0001$), indicating that *Npc1*$^{-/-}$ neuronal lysosomes accumulate both luminal and membrane cholesterol.

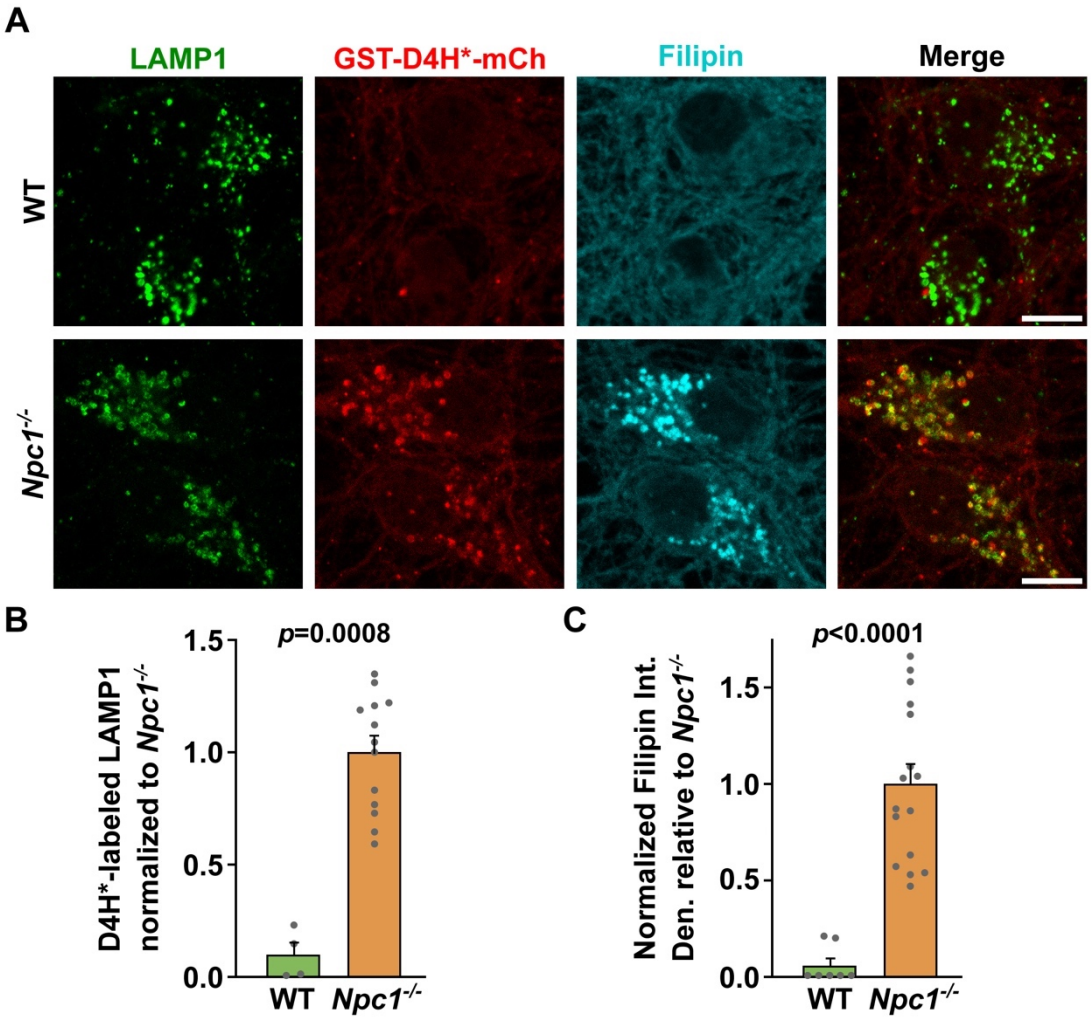


Figure 3.11 – Elevated cholesterol on lysosome membranes in Npc1$^{-/-}$ neurons. *(**A-C**) Representative images (**A**) and quantitative analyses (**B, C**) showing cholesterol enriched at the limiting membrane of lysosomes from Npc1$^{-/-}$ neurons. Cortical neurons at DIV7-8 were fixed, permeabilized with a 30-sec pulse in liquid nitrogen, and labelled with GST-D4H*-mCherry and filipin to detect cholesterol, followed by immunostaining for LAMP1. Merged images are of LAMP1 and GST-D4H*-mCherry. To quantify membrane cholesterol on LAMP1-positive endolysosomes, colocalization between D4H* and LAMP1 was measured and expressed as the fraction of LAMP1-vesicles that were also positive for D4H*. To quantify luminal cholesterol levels, the integrated density of filipin was measured in thresholded images and normalized to Npc1$^{-/-}$. Data are presented as mean ± SEM with dots representing individual images (**B:** WT n=7, Npc1$^{-/-}$ n=20) or neurons (**C:** WT n=7, Npc1$^{-/-}$ n=16) and analyzed by Mann-Whitney test. Scale bars: 10 µm.*

We next asked whether elevated cholesterol content at the limiting membrane of Npc1$^{-/-}$ neuronal lysosomes leads to sequestration of Arl8 and kinesin-1. To address

this, we first sought to pharmacologically reduce lysosomal membrane cholesterol levels. Cyclodextrin derivatives have commonly been used to extract cholesterol from membranes (229-231). Interestingly, the cyclodextrin derivative 2-hydroxypropyl-β-cyclodextrin (HPCD) was previously shown to reduce luminal cholesterol accumulation, delay disease onset, and extend life span in *Npc1*$^{-/-}$ mice (232-234), which supported its rationale for evaluation in a clinical trial with NPC patients (235). However, it remains to be determined whether cyclodextrin can effectively remove cholesterol from *Npc1*$^{-/-}$ neuronal lysosome membranes. Strikingly, treatment of *Npc1*$^{-/-}$ cortical neurons with HPCD almost completely reversed D4H*-mCh signals on lysosome membranes ($p < 0.0001$) and also significantly reduced luminal cholesterol ($p < 0.0001$) in *Npc1*$^{-/-}$ lysosomes (**Figures 3.12A and 3.12B**).

Having established pharmacologic conditions that effectively lower membrane cholesterol in *Npc1*$^{-/-}$ neuronal lysosomes in the soma, we next determined whether HPCD treatment could release the sequestration of endogenous Arl8 and kinesin-1 from the surface of lysosome membranes. STED super-resolution imaging revealed that while Arl8 and kinesin-1 appear distributed throughout the soma of WT neurons, they showed pronounced accumulation on the surface of cholesterol-enriched LAMP1-labeled endolysosomes in *Npc1*$^{-/-}$ neurons. Remarkably, treatment with HPCD released Arl8 and kinesin-1 sequestration from *Npc1*$^{-/-}$ lysosome membranes, returning to a cytosolic distribution similar to that observed in WT neurons (**Figures 3.13A and 3.13B**).

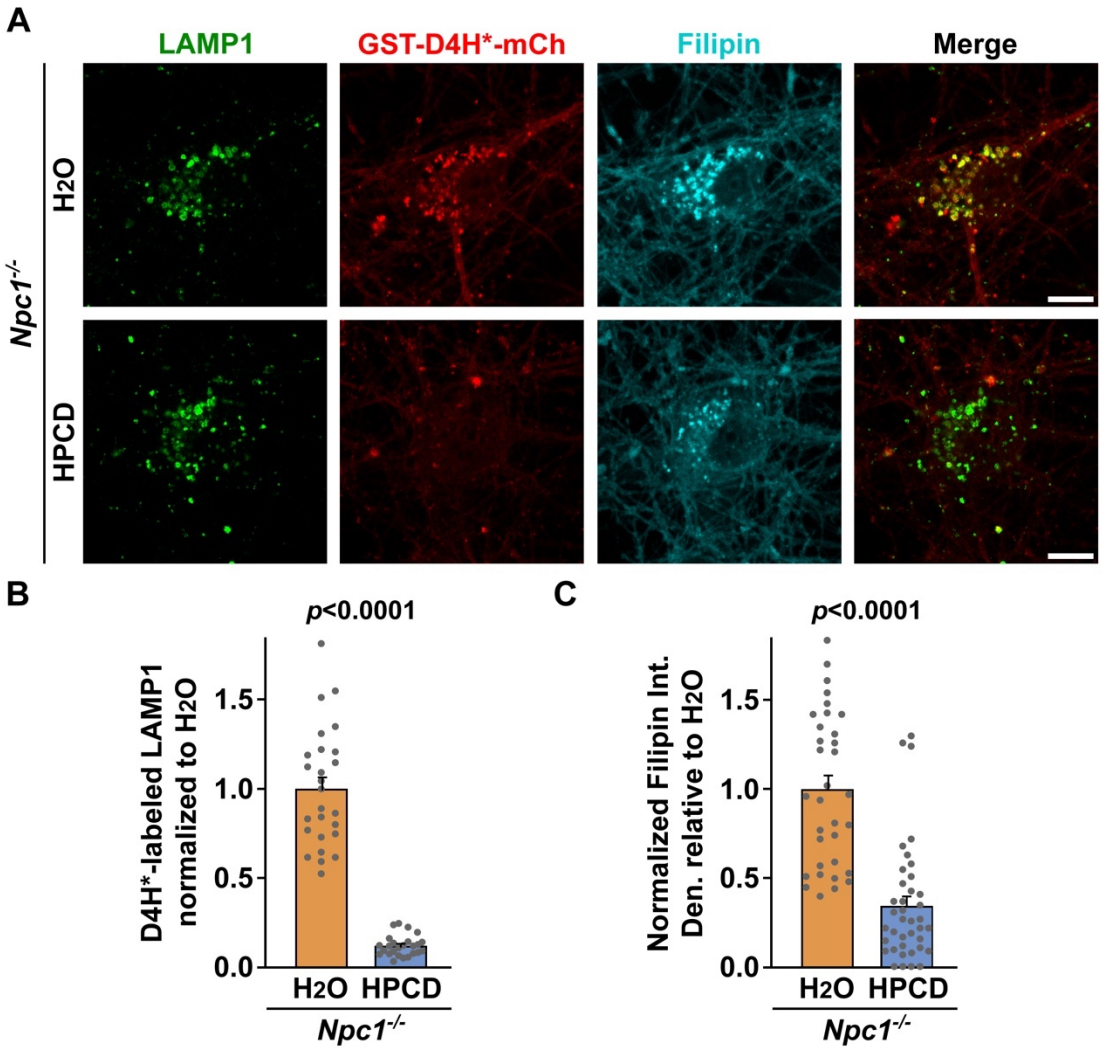


Figure 3.12 – Pharmacologic treatment with 2-hydroxypropyl-β-cyclodextrin (HPCD) reduces cholesterol from lysosome membranes in Npc1$^{-/-}$ neurons.
*(**A-C**) Representative images (**A**) and quantitative analyses (**B, C**) showing reduced cholesterol on lysosome membranes and the lumen of Npc1$^{-/-}$ neurons following HPCD treatment. Cortical neurons were treated with HPCD (100 μM) for 48 hours at DIV5-6, followed by endolysosomal cholesterol labeling at DIV7-8. Merged images are of LAMP1 and GST-D4H*-mCherry. Membrane and luminal cholesterol were quantified as in **Figure 3.11** but with normalization to H_2O control. Data are presented as mean ± SEM with dots representing individual images (**B:** H_2O n=37, HPCD n=39) or neurons (**C:** H_2O n=33, HPCD n=39) and analyzed by Student's t test. Scale bars: 10 μm.*

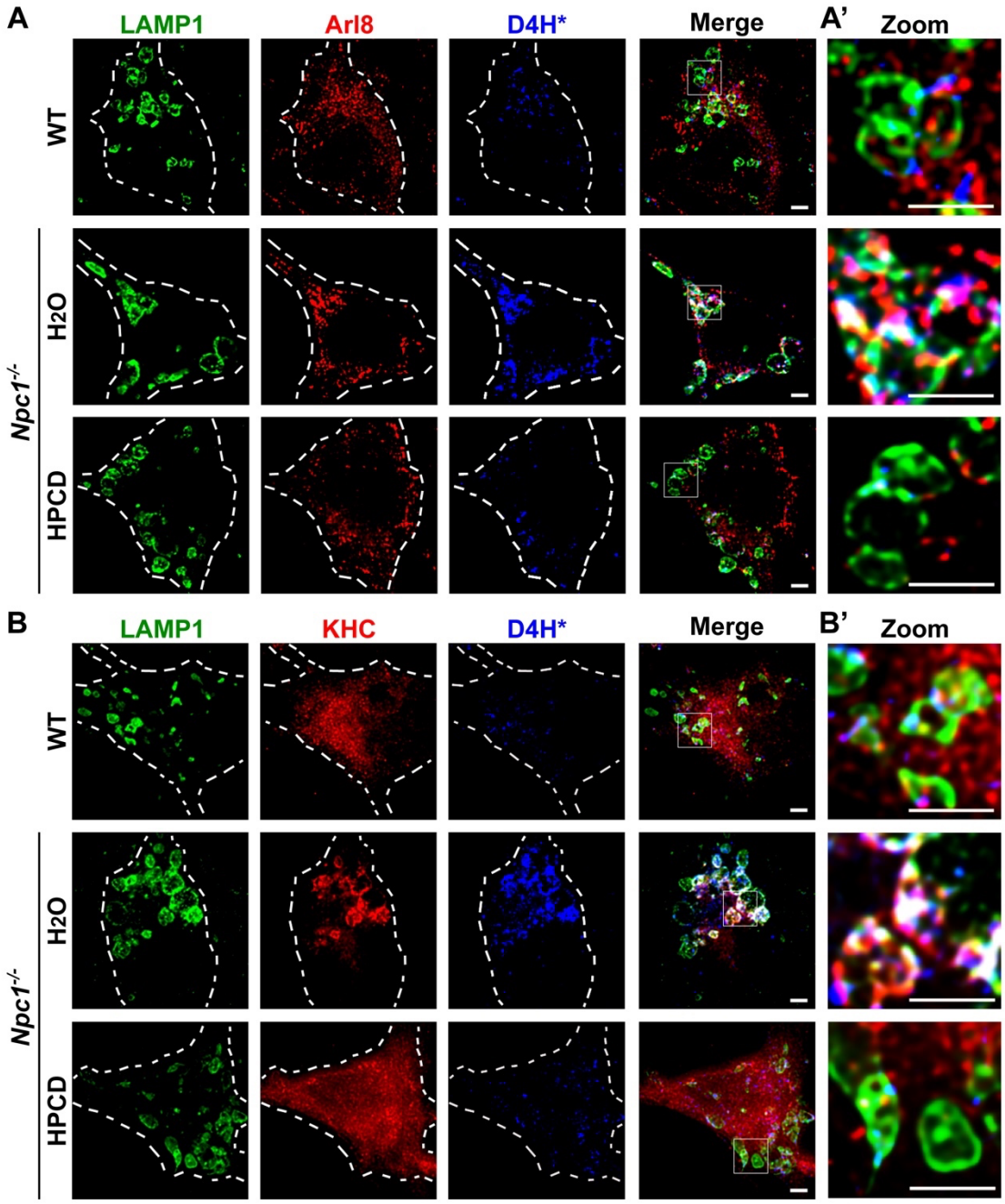


Figure 3.13 – STED imaging reveals that reducing membrane cholesterol with HPCD releases sequestration of Arl8 and kinesin-1 from Npc1$^{-/-}$ lysosome membranes.

*(**A, B**) Representative STED images showing release of sequestrated Arl8 (**A**) and kinesin-1 (**B**) in Npc1$^{-/-}$ neurons by reducing lysosomal cholesterol with HPCD. Cortical neurons at DIV8 were labeled with GST-D4H*-mCherry, followed by immunostaining for LAMP1 and Arl8 (**A**) or kinesin-1 (**B**). A blue pseudo-color was applied to visualize GST-D4H*-mCherry membrane cholesterol labeling; a red pseudo-color was applied to visualize Arl8 (**A**) or kinesin-1 (**B**) immunostaining. The edges of cell bodies and proximal processes are outlined with white dashed lines. Enlarged views of the corresponding boxed regions are shown in (**A'**) and (**B'**). Scale bars: 2 µm. Experiment carried out in collaboration with S. Li (NINDS, NIH).*

As a complementary approach, we magnetically isolated endolysosomes from WT and *Npc1*$^{-/-}$ neurons to further examine the altered distribution of the kinesin-1-SKIP-Arl8 transport complex on *Npc1*$^{-/-}$ lysosomes. Neuronal lysosomes were loaded with iron-dextran and separated by magnetic chromatography (223, 224), followed by immunoblotting to assess relative protein levels within endolysosomal membranes. LAMP1, but not GAPDH or TOM20, was readily detected in captured organelles, indicating an enriched endolysosome population following magnetic chromatography. Consistent with results observed by STED imaging, lysosomal membranes showed increased levels of Arl8 and kinesin-1, but not SKIP, in *Npc1*$^{-/-}$ neurons compared to WT, further supporting their non-functional accumulation in the absence of the GTPase effector SKIP. Importantly, HPCD treatment reduced the abnormal accumulation of Arl8 and kinesin-1 on endolysosome membranes of *Npc1*$^{-/-}$ neurons (**Figures 3.14A and 3.14B**), further suggesting lipid-mediated protein sequestration. These changes occurred without noticeable differences in the total protein levels in whole cell lysates, suggesting that the observed alterations occur locally at *Npc1*$^{-/-}$ lysosomal membranes. Collectively, these STED imaging and lysosome purification analyses consistently suggest that altered lysosomal limiting membrane lipid composition may drive the aberrant sequestration of Arl8 and kinesin-1 on *Npc1*$^{-/-}$ lysosome membranes in the soma.

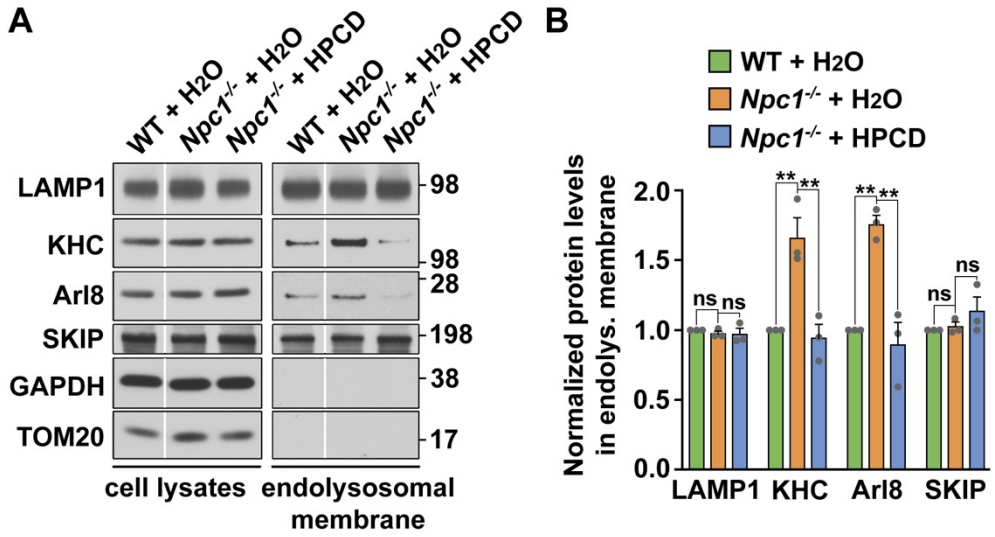


Figure 3.14 – Endolysosomal membrane isolations show that HPCD treatment releases sequestration of Arl8 and kinesin-1 from Npc1$^{-/-}$ lysosome membranes.

*(**A, B**) Sequential immunoblots (**A**) and quantitative analysis (**B**) showing release of sequestrated kinesin-1 and Arl8 from Npc1$^{-/-}$ neuronal lysosomes by depleting lysosomal membrane cholesterol with HPCD. Cortical neurons were treated with HPCD (100 µM) or H_2O control for 48 hours, followed by magnetic isolation of lysosomes at DIV8. Equal amounts of whole cell lysates (5 µg) and captured endolysosomes (0.8 µg) were loaded and sequentially immunoblotted with antibodies as indicated. Protein band intensities were quantified and averaged from three repeats. Data were normalized to H_2O-treated WT control neurons and analyzed by one-way ANOVA. **p < 0.01. Experiment carried out in collaboration with N. Huang (NINDS, NIH).*

3.4 – Discussion

Here, we reveal that impaired anterograde transport and delivery of lysosomes to distal axons contributes to reduced lysosome density in NPC axons. We show that elevated cholesterol on NPC lysosome membranes in the soma aberrantly sequesters kinesin-1 motors and the kinesin-lysosome adaptor Arl8, resulting in a significant depletion of lysosomes in NPC distal axons. We further observe that the cyclodextrin derivative 2-hydroxypropyl-β-cyclodextrin reduces cholesterol levels on NPC lysosomal membranes. Based on these observations, we propose a pathological mechanism in which elevated membrane cholesterol on NPC somatic lysosomes impairs their delivery into axons, thus disrupting distal degradation capacity in NPC.

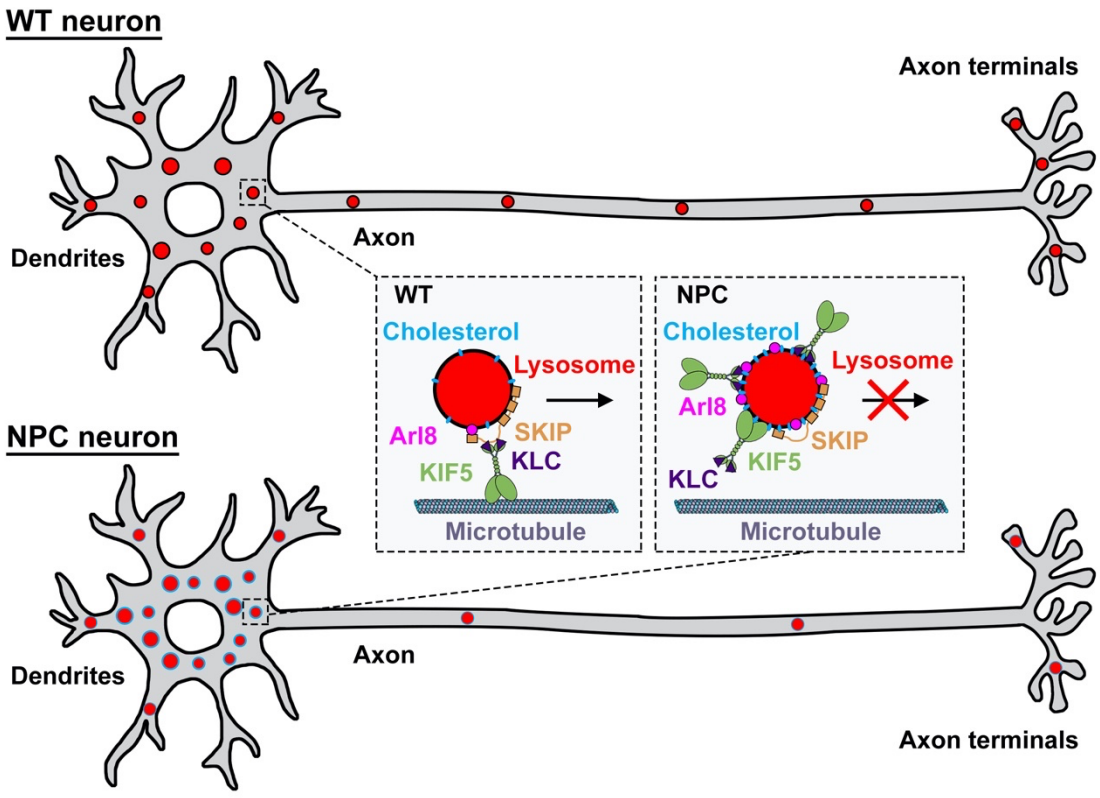


Figure 3.15 – Schematic diagram showing lipid-mediated sequestration of motor-adaptor proteins impairs axonal lysosome delivery in Npc1$^{-/-}$ neurons. *In WT neurons, Arl8 links somatic lysosomes to kinesin-1 motors through SKIP interaction, resulting in efficient lysosome transport to distal axons (143). However,*

in NPC neurons, elevated cholesterol within lysosome membranes in the soma may sequester Arl8 and kinesin-1, leading to impaired axonal lysosome delivery.

Defective axonal delivery of soma-derived lysosomes suggested a disruption to kinesin-1-driven anterograde lysosome transport in NPC neurons under pathological conditions. Cholesterol accumulation in the lumen of NPC lysosomes was previously shown to alter lysosome positioning in NPC through the Rab7/RILP/ORP1L pathway (121) and the TMEM55B/JIP4 pathway (127) as well as impair Rab7 and kinesin function (219). Abnormal cholesterol accumulation was also previously observed to stabilize Rab9 on NPC membranes (218) and sequester SNARE fusion proteins in the two neurodegenerative LSDs multiple sulfatase deficiency and mucopolysaccharidosis type IIIA (236), indicating the pathological role cholesterol accumulation plays in altering endolysosomal membrane events. However, the underlying mechanisms and pathological relevance of cholesterol accumulation in NPC neurons and whether this contributes to altered lysosome positioning in NPC axons remain unknown.

Here, we observed that axonal lysosomes in NPC display a selective defect in anterograde transport with no changes in their retrograde motility, resulting in a net reduction of degradative lysosomes in NPC axons. While it is well established that cholesterol progressively stores in the lumen of NPC lysosomes, it was recently reported that NPC lysosomes also accumulate ER-derived cholesterol at the limiting membrane (221). These membrane changes may also in part contribute to the alterations in Rab7 and kinesin function observed in previous studies (218, 219). To elucidate mechanisms underlying impaired axonal lysosome delivery in NPC neurons, we used STED super-resolution imaging to study the recruitment of the Arl8-SKIP-kinesin-1 axonal lysosome transport complex (143) to NPC lysosome

membranes at nanometer resolution. Consistent with a potential role for lysosomal membrane cholesterol in altering anterograde lysosome transport, we observed that Arl8 and kinesin-1, but not the Arl8-kinesin-1 linker SKIP, showed enhanced membrane association on NPC lysosomes. Given that SKIP links Arl8 to kinesin-1 through binding Arl8 in its active GTP-bound state (107) and is required for kinesin-1 to promote lysosome transport into axons (143), this suggested their non-functional membrane association, likely triggered by altered lipid composition within NPC lysosome membranes. In line with this notion, pharmacologic reduction of membrane cholesterol with HPCD released the sequestration of Arl8 and kinesin-1, returning to a similar distribution to that observed in WT neurons.

Moreover, cyclodextrin was reported to reduce sphingolipid accumulation in lysosomes (237) and reduce cholesterol storage by facilitating lysosomal exocytosis (238). Therefore, it is possible that elevated membrane sphingolipid content may also contribute to the lipid-mediated sequestration of non-functional motors and adaptors on NPC lysosome membranes. Levels of cholesterol and sphingolipids in biological membranes influence membrane properties and their organization into liquid-ordered and -disordered lipid phases (239). At physiological levels, cholesterol-enriched membrane domains play an important role in supporting various signaling and membrane trafficking events (240, 241). Proteins may preferentially associate and sequester into cholesterol-enriched regions of the membrane for their normal function (242, 243). However, abnormally elevated cholesterol levels were reported to alter SNARE complex assembly (236) and interfere with the GDP-GTP cycle of small GTPases (218, 219), indicating a pathological role for excess membrane cholesterol in driving aberrant protein sequestration. Because cholesterol is an important regulator of membrane organization, cells must maintain cholesterol levels within a narrow range. Therefore,

treatment with cyclodextrin derivatives may require careful dosing, as excessive depletion of cholesterol from cellular membranes may alter cholesterol-dependent homeostatic events (37, 244, 245).

Collectively, these results suggest that changes in lipid composition within NPC lysosomal membranes abnormally sequester axonal lysosome motor-adaptor proteins, resulting in impaired delivery of soma-derived lysosomes into NPC axons.

CHAPTER 4 – GENETIC AND PHARMACOLOGICAL RESCUE OF AXONAL LYSOSOME DELIVERY AND ITS IMPACT ON AXONAL HOMEOSTASIS IN NPC

4.1 – Introduction

Endolysosomal trafficking requires coordinated regulation to maintain efficient uptake and clearance capacity throughout the cell (3, 60). The autophagy pathway represents one membrane trafficking route in which damaged organelles and aggregated proteins captured within autophagosomes are delivered to lysosomes for degradation and recycling (69, 70). Neurons are particularly sensitive to perturbations in autophagy-lysosomal function, in part due to their polarized morphology and longevitiy (246). Indeed, autophagy follows a spatially compartmentalized organization in neurons (247, 248). In axons, autophagosomes are predominantly formed at distal terminals and subsequently transported retrogradely towards the cell body where biosynthetic and degradative compartments are enriched (136, 142, 158). Axonal autophagosomes acquire dynein motors through fusion with late endosomes, resulting in hybrid organelles referred to as amphisomes (**Figure 4.1**), and blocking autophagosome-late endosome fusion results in the accumulation of stationary autophagosomes in distal axons (136). Therefore, retrograde transport of axonal autophagosomes is critical for maintaining neuronal homeostasis by preventing autophagosome buildup within the axon.

One intriguing aspect of axonal autophagy is the observation that autophagosomes mature and become increasingly acidified as they move from distal to proximal (158). This process is thought to promote encounters with late endosomes and lysosomes during their retrograde transport route, thereby facilitating the maturation and clearance of autophagic cargo, which includes synaptic proteins, mitochondrial fragments, and pathogenic protein aggregates (132, 249). Axonal accumulation of autophagosomes and lysosome-like organelles characterizes the early stages of

several neurodegenerative diseases (44, 139, 142, 186-188, 246), highlighting the importance of axonal organelle transport to neuronal survival. However, the impact of lysosome anterograde trafficking and positioning on axonal pathology and its contribution to the pathogenesis of neurodegenerative diseases remains largely unknown.

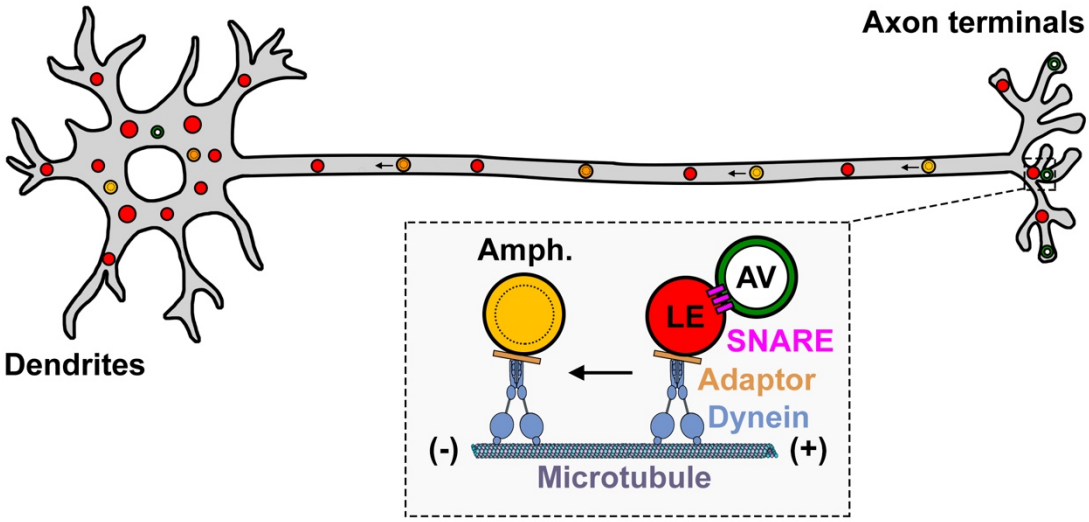


Figure 4.1 – Schematic diagram of axonal autophagosome maturation coupled to their retrograde transport. *Autophagic vacuoles (AVs) acquire dynein motors following fusion with late endosomes (LEs) to form amphisomes (Amph.) in a motor-adaptor sharing model (136). Arrows indicate maturing axonal autophagosomes as they move retrogradely toward the cell body.*

In this chapter, we examine the relevance of soma-derived lysosome transport to distal axons in the maintenance of axonal homeostasis and neuron survival in NPC using genetic and pharmacologic approaches.

4.2 – Materials and Methods

4.2.1 – siRNA Knockdown

Stealth RNAi oligonucleotides (Thermo Fisher Scientific) were used for small interfering RNA (siRNA) knockdown experiments. After isolating and before plating, DRG neurons were nucleofected with 60 nM single oligonucleotide siRNAs against Arl8a and Arl8b or a scrambled control. Knockdown efficiency was assessed by western blotting and immunostaining. Single oligonucleotide siRNA sequences are provided in Appendix 1.

4.2.2 – TUNEL Assay and Analysis

Neurons were plated on 12-mm poly-L-ornithine-coated coverslips in 6-well plates. Where indicated and before plating, neurons were transduced with lentiviruses encoding Arl8b-mCh or mCh. At DIV7 and DIV10, cells were fixed and immunostained for MAP2 followed by TUNEL staining. TUNEL-positive neurons were detected using the Fluorescein *In Situ* Cell Death Detection Kit according to the manufacturer's instructions. The coverslips were mounted with anti-fade mounting medium with DAPI. Neurons were visualized with a 40x/1.3 NA oil immersion objective on a Zeiss LSM880 confocal microscope. Images of entire coverslips were acquired using the Tiles acquisition mode setting in Zeiss ZEN black software. The percentage of TUNEL-positive cells to total DAPI staining was calculated in thresholded, watershed segmented images using ImageJ.

4.2.3 – Image Acquisition and Analysis

Confocal images were acquired and analyzed as in Section 2.2.10. For quantification of integrated density in axonal growth cones, the desired channel was segmented, and raw fluorescent intensity values were retrieved by redirecting the binary mask to the original 16-bit grayscale image. Mean integrated density values were calibrated to the area of the axonal growth cone and normalized to a reference group as indicated in the corresponding figure.

4.3 – Results

4.3.1 – Pharmacologic Rescue of Axonal Lysosome Delivery Reduces Autophagic Stress in *Npc1*$^{-/-}$ Neuronal Axons

We investigated whether pharmacologic reduction of lysosomal membrane cholesterol with HPCD, and therefore releasing Arl8/kinesin-1 sequestration, has an impact on axonal lysosome density in DRG neurons isolated from presymptomatic *Npc1*$^{-/-}$ mice. To test this, DRG neurons cultured from adult mice (P30-40) were incubated with HPCD for 48 hours, followed by co-immunostaining for LAMP1 and β3-tubulin. In WT neurons, HPCD treatment did not significantly alter the number of lysosomes along axons compared to H_2O control (**Figures 4.2A-4.2C**; WT H_2O: 17.31 ± 1.84; WT HPCD: 13.87 ± 1.15; $p > 0.9999$; per 100 μm axon length). However, *Npc1*$^{-/-}$ neurons treated with HPCD showed a striking increase in the number of axonal lysosomes compared to H_2O-treated *Npc1*$^{-/-}$ neurons (**Figures 4.2A-4.2C**; *Npc1*$^{-/-}$ H_2O: 8.54 ± 1.02; *Npc1*$^{-/-}$ HPCD: 15.20 ± 1.44; $p = 0.0014$; per 100 μm axon length), suggesting that reducing lysosomal membrane cholesterol effectively rescues lysosome transport into axons from presymptomatic *Npc1*$^{-/-}$ mice.

We directly tested this possibility by examining the anterograde transport of lysosomes from the soma to distal axons in *Npc1*$^{-/-}$ neurons following HPCD treatment. Neurons were cultured in microfluidic devices, and only the soma/dendritic chamber was briefly loaded with MDW933 for 15 minutes to label active GCase-positive lysosomes in the cell body. Neurons were then washed and fixed after 0, 1, 2, or 3 hours, followed by imaging lysosomes at axonal terminals within the axon chamber. Remarkably, as post-wash time increased from 0 to 3 hours, HPCD treatment resulted in a more rapidly progressive accumulation of active GCase signal at distal growth cones compared to H_2O-treated *Npc1*$^{-/-}$ neurons

(**Figures 4.3A and 4.3B**), reflecting enhanced axonal lysosome delivery from the cell body.

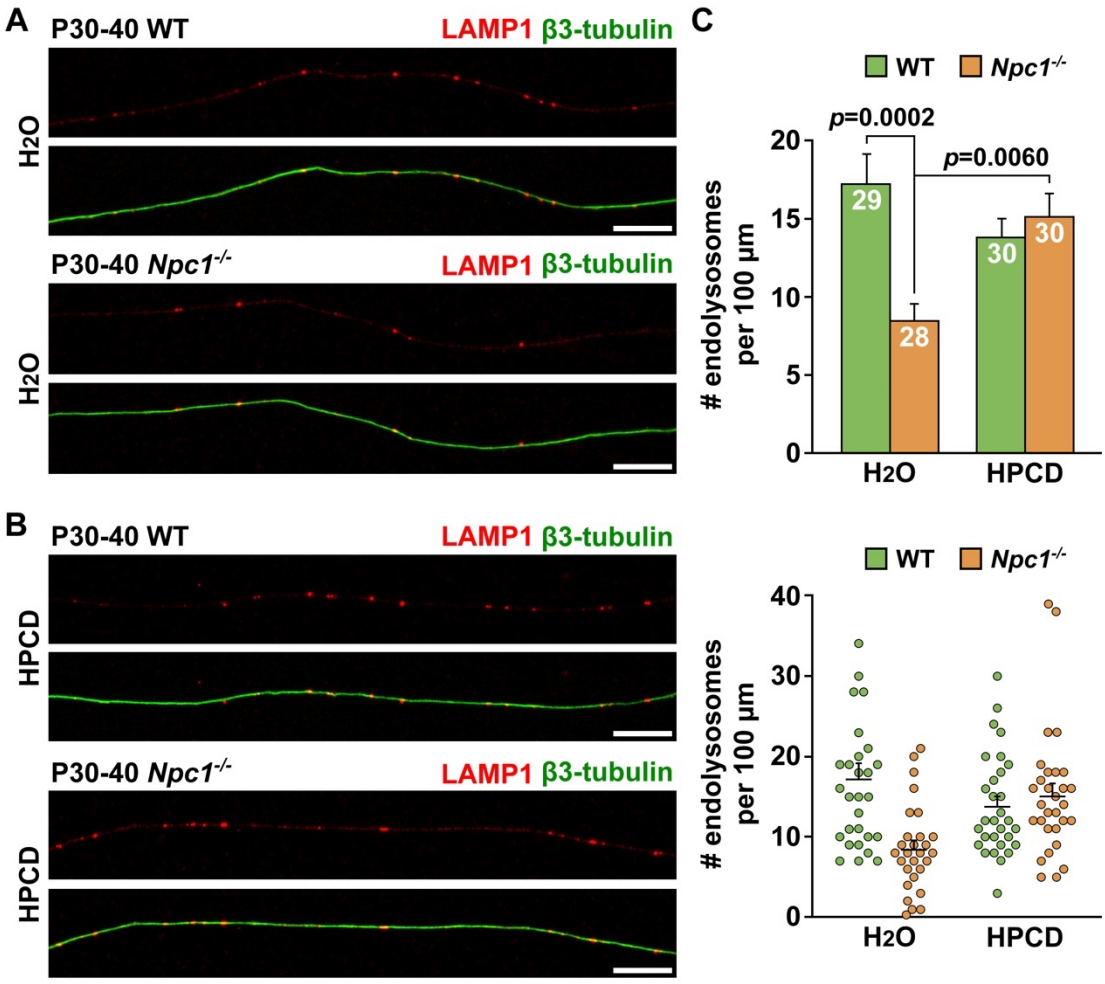


Figure 4.2 – Pharmacologic rescue of axonal lysosome distribution with HPCD in DRG neurons from presymptomatic Npc1$^{-/-}$ mice.
*(**A-C**) Representative images (**A, B**) and quantitative analysis (**C**) showing increased axonal lysosome density following depletion of lysosomal membrane cholesterol with HPCD treatment. DRG neurons from mice at P30-40 were treated with HPCD (100 µM) for 48 hours at DIV1-2 followed by co-immunostaining for LAMP1 and β3-tubulin at DIV3-4. Data were collected from the total number of axons indicated within bars, presented as mean ± SEM with dots representing individual axons, and analyzed by one-way ANOVA. Scale bars: 10 µm.*

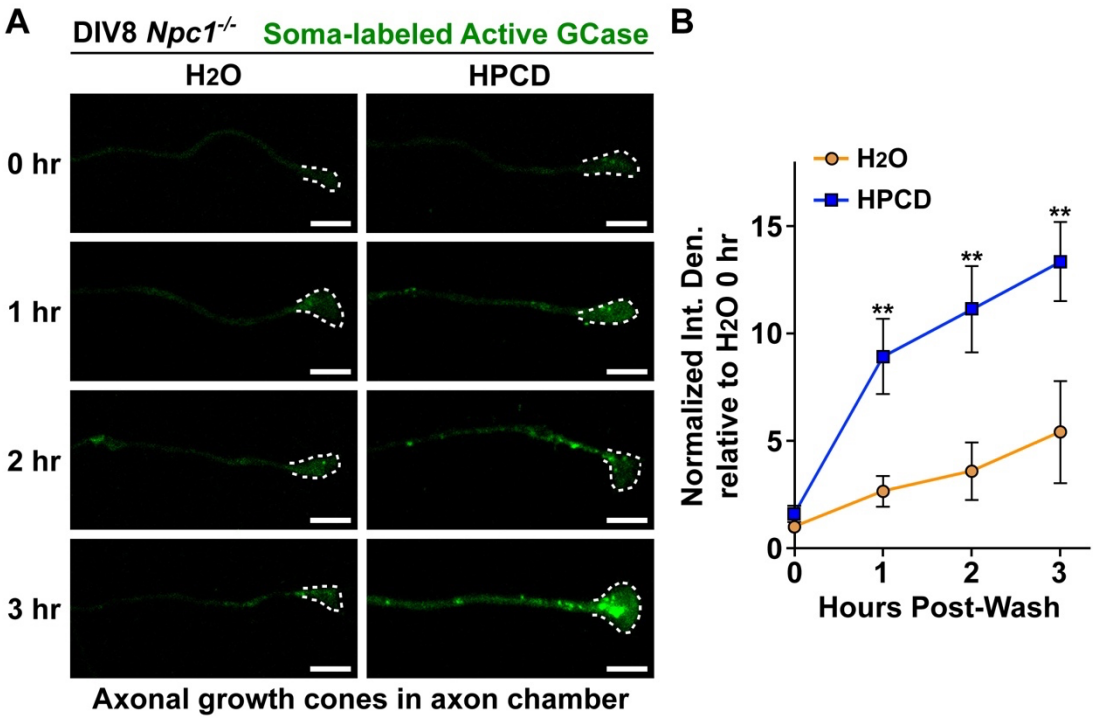


Figure 4.3 – HPCD treatment enhances axonal lysosome delivery in Npc1$^{-/-}$ neurons.

*(**A, B**) Representative images (**A**) and quantitative analysis (**B**) showing enhanced delivery of soma-labeled lysosomes to distal axons following HPCD treatment in Npc1$^{-/-}$ neurons cultured in microfluidic devices. At DIV8, MDW933 (500 nM) was applied only to the soma/dendritic chamber for 15 minutes to label active GCase-positive lysosomes in the cell body. Neurons were then washed and fixed after 0, 1, 2, or 3 hours, followed by immunostaining for β3-tubulin to identify axon terminals. Axonal growth cones are outlined with white dashed lines. Data were collected from greater than 30 axon terminals for each time point and analyzed by two-way ANOVA with Sidak's multiple comparisons test. **p < 0.01. Error bars: SEM, Scale bars: 5 μm.*

Moreover, our previous study demonstrated that soma-derived lysosomes transport to distal axons and target to axonal autophagic cargo (135). In this study, we tested whether reduced axonal lysosome delivery impacts axonal clearance of autophagosomes by targeted knockdown of the kinesin-lysosome adaptor Arl8, which was previously shown to regulate axonal transport of endolysosomes and presynaptic cargos (143, 250). In mammalian cells, Arl8 has two isoforms: Arl8a and Arl8b. Therefore, we depleted Arl8 expression in DRG neurons using small

interfering RNAs (siRNAs) against both Arl8a and Arl8b, which significantly decreased endogenous Arl8a/b by western blotting and immunostaining (**Figures 4.4A-4.4C**). We then examined the impact of Arl8 knockdown on axonal lysosome distribution and autophagosome maturation in axons. DRG neurons were co-nucleofected with EGFP-LC3 together with control or Arl8a/b siRNAs at DIV0, followed by incubation with MDW941 prior to live imaging at DIV3. In neurons expressing control siRNA, active GCase-positive lysosomes were distributed along axons, whereas EGFP-LC3 appeared mostly diffuse. However, depleting Arl8 significantly reduced the density of lysosomes in axons and increased axonal autophagosome density (**Figures 4.5A and 4.5B**), reflecting axonal autophagic stress. These results demonstrate that lysosome transport to distal axons is critical for maintaining efficient autophagic flux (135).

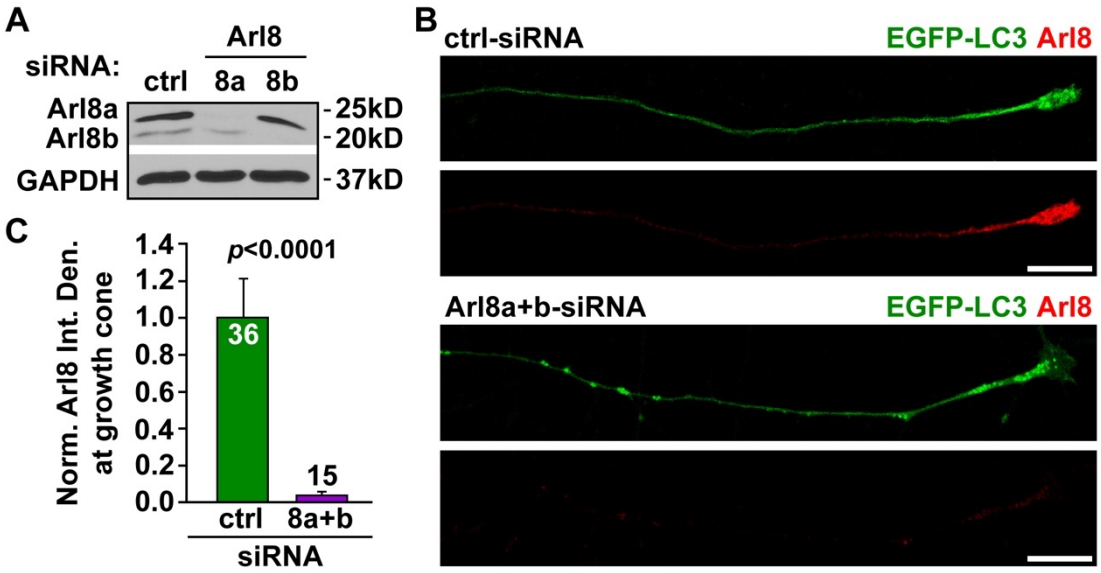


Figure 4.4 – Arl8 siRNA knockdown efficiency.
*(**A**) Immunoblot showing siRNA-mediated depletion of Arl8a/b. DRG neurons were nucleofected with siRNAs against Arl8a/b or a scrambled control (ctrl) at DIV0, and levels of knockdown were assessed at DIV3 by immunoblotting equal amounts of cell lysates (6 µg) with antibodies against Arl8 and GAPDH.*
*(**B, C**) Images showing siRNA-mediated depletion of Arl8/b. DRG neurons were co-nucleofected with EGFP-LC3 and Arl8/b siRNAs or a scrambled control (ctrl). Knockdown was assessed by immunostaining for endogenous Arl8 at DIV3-4. The*

integrated density of Arl8 fluorescence was measured at axonal growth cones using ImageJ, and data are presented as mean integrated density normalized to control siRNA.
Data were collected from the total number of growth cones indicated in or above bars and analyzed by Student's t test. Error bars: SEM, Scale bars: 10 µm.

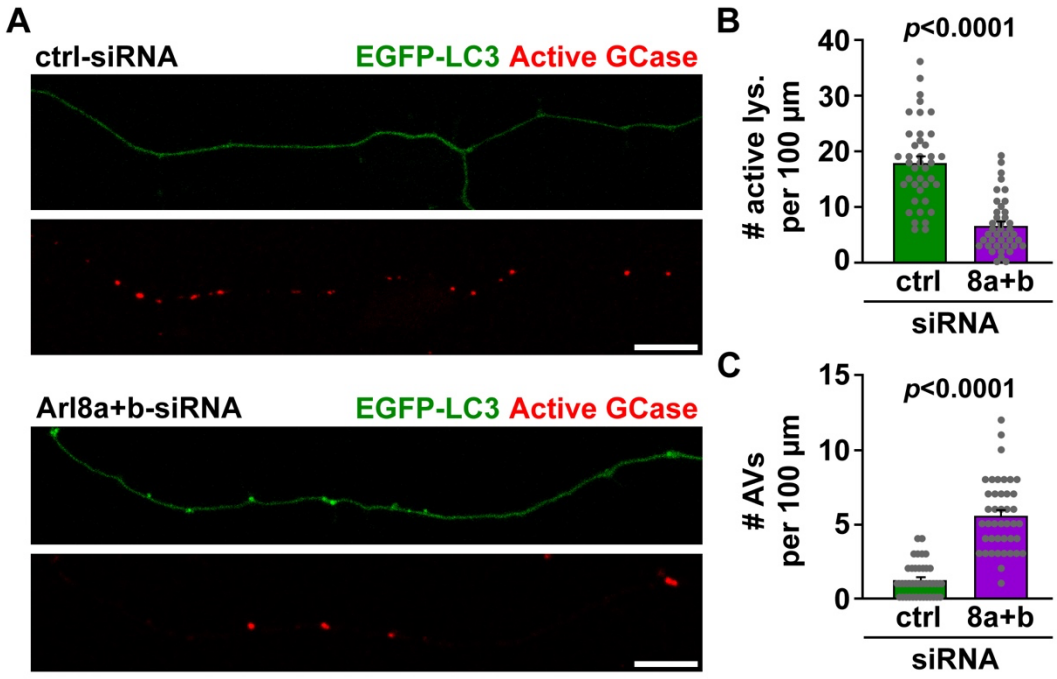


Figure 4.5 – Impaired axonal lysosome delivery induces autophagic stress in axons.
*(**A-C**) Representative images (**A**) and quantitative analyses (**B, C**) showing increased axonal autophagic stress with Arl8 knockdown-mediated disruption of axonal lysosome delivery. DRG neurons were co-nucleofected at DIV0 with EGFP-LC3 to label autophagic vacuoles (AVs) and siRNAs against Arl8a/b or a scrambled control (ctrl). Neurons were then incubated with MDW941 for 30 minutes prior to live imaging at DIV3-4. Note that depleting Arl8 reduced the density of axonal lysosomes and increased the density of AVs in distal axons. Data are presented as mean ± SEM with dots representing individual axons (**B:** ctrl n=40, 8a+8b n=40; **C:** ctrl n=40, 8a+8b n=42) and analyzed by Student's t test. Scale bars: 10 µm.*

Given that lysosome transport defects precede axonal autophagosome accumulation in *Npc1*$^{-/-}$ neurons (**Figures 2.5 and 3.6**), we next determined whether rescuing axonal lysosome delivery with HPCD treatment has an impact on axonal autophagic stress in *Npc1*$^{-/-}$ neurons. To test this, DRG neurons from P30-40 *Npc1*$^{-/-}$ mice were nucleofected with EGFP-LC3 at DIV0, treated with HPCD for 48-72 hours,

then incubated with MDW941 for 30 minutes to label active GCase-positive lysosomes prior to live imaging at DIV3-4. Notably, treatment with HPCD resulted in an increased density of axonal lysosomes (*Npc1*$^{-/-}$ + H_2O: 5.22 ± 0.60; *Npc1*$^{-/-}$ + HPCD: 12.47 ± 1.24; $p < 0.0001$; per 100 µm axon length) and a reduced density of axonal autophagosomes (*Npc1*$^{-/-}$ + H_2O: 8.32 ± 0.62; *Npc1*$^{-/-}$ + HPCD: 3.28 ± 0.45; $p < 0.0001$; per 100 µm axon length) (**Figures 4.6A-4.6D**), suggesting that reducing lysosomal membrane cholesterol and therefore enhancing axonal lysosome delivery facilitates autophagic flux in distal axons of DRG neurons from presymptomatic *Npc1*$^{-/-}$ mice.

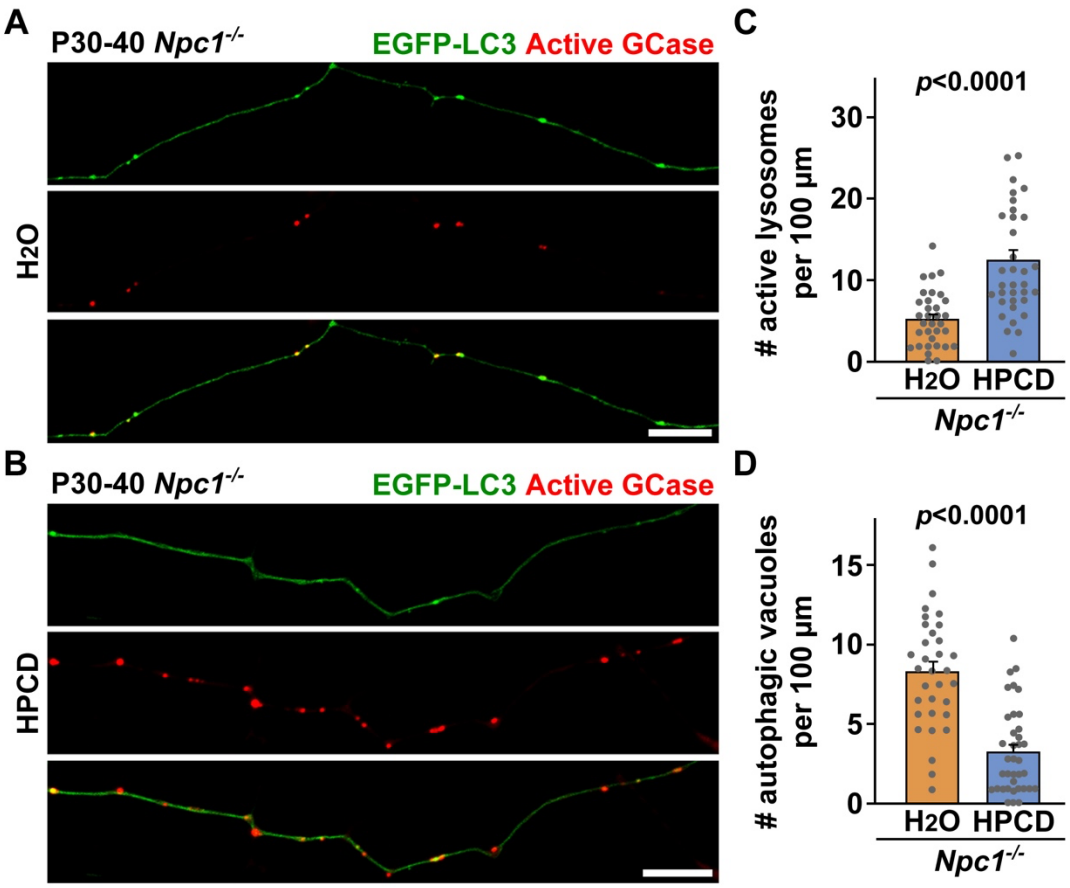


Figure 4.6 – HPCD treatment facilitates axonal autophagic flux in Npc1$^{-/-}$ neurons.

*(**A-D**) Representative images (**A, B**) and quantitative analyses (**C, D**) showing increased density of axonal lysosomes and reduced density of axonal autophagosomes by lowering lysosomal membrane cholesterol with HPCD*

*treatment in DRG axons from P30-40 Npc1$^{-/-}$ mice. DRG neurons were nucleofected with EGFP-LC3 at DIV0 and treated with HPCD (100 μM) at DIV1-2, followed by live imaging at DIV3-4. Data are presented as mean ± SEM with dots representing individual axons (**C:** H_2O n=33, HPCD n=35; **D:** H_2O n=33, HPCD n=37) and analyzed by Student's t test. Scale bars: 10 μm*.

4.3.2 – Elevated Expression of Kinesin-lysosome Adaptor Arl8b Facilitates Lysosome Transport into Axons and Reduces Axonal Autophagic Stress and Neuron Death in Presymptomatic *Npc1$^{-/-}$* Neurons

It was reported that Arl8b operates as a rate-limiting factor in assembling functional kinesin-1 transport complexes on neuronal lysosomes and that overexpressing Arl8b increases lysosome positioning at distal axon terminals (143). In addition, previous studies demonstrated that SKIP binds Arl8 in its active GTP-bound form (107), and kinesin-1 requires SKIP to drive lysosome transport into axons (143). Because SKIP did not show enhanced lysosomal membrane association, Arl8 may be sequestered in a non-functional GDP-bound form. Therefore, SKIP may be unable to bind and properly assemble kinesin-1 axonal lysosome transport complexes. We tested whether elevated Arl8b expression in *Npc1$^{-/-}$* neurons is able to overcome the lipid-mediated membrane sequestration of endogenous Arl8, and therefore recruit SKIP to rescue the anterograde transport of lysosomes to distal axons. DRG neurons isolated from presymptomatic *Npc1$^{-/-}$* mice at P30-40 were nucleofected with Arl8b-mCh at DIV0, followed by co-immunostaining for LAMP1 and β3-tubulin at DIV3-4. Strikingly, elevated Arl8b expression rescued lysosome density in *Npc1$^{-/-}$* axons (*Npc1$^{-/-}$*: 8.58 ± 0.91; *Npc1$^{-/-}$* with Arl8b-mCh: 29.73 ± 3.18; $p < 0.0001$; per 100 μm axon length) and also further increased the number of lysosomes in axons from control WT littermates (WT: 18.80 ± 1.50; WT with Arl8b-mCh: 32.11 ± 2.56; $p = 0.0156$; per 100 μm axon length) (**Figures 4.7A-4.7C**). Concordantly, elevated Arl8b-mCh expression in *Npc1$^{-/-}$* neurons reduced the accumulation of lysosomes in

the soma (**Figure 4.8A and 4.8B**). Notably, excessively high levels of Arl8b overexpression resulted in axonal organelle accumulation in *Npc1*$^{-/-}$ axons (**Figure 4.9**), highlighting the importance of maintaining a steady-state distribution of axonal lysosomes to axonal homeostasis (140).

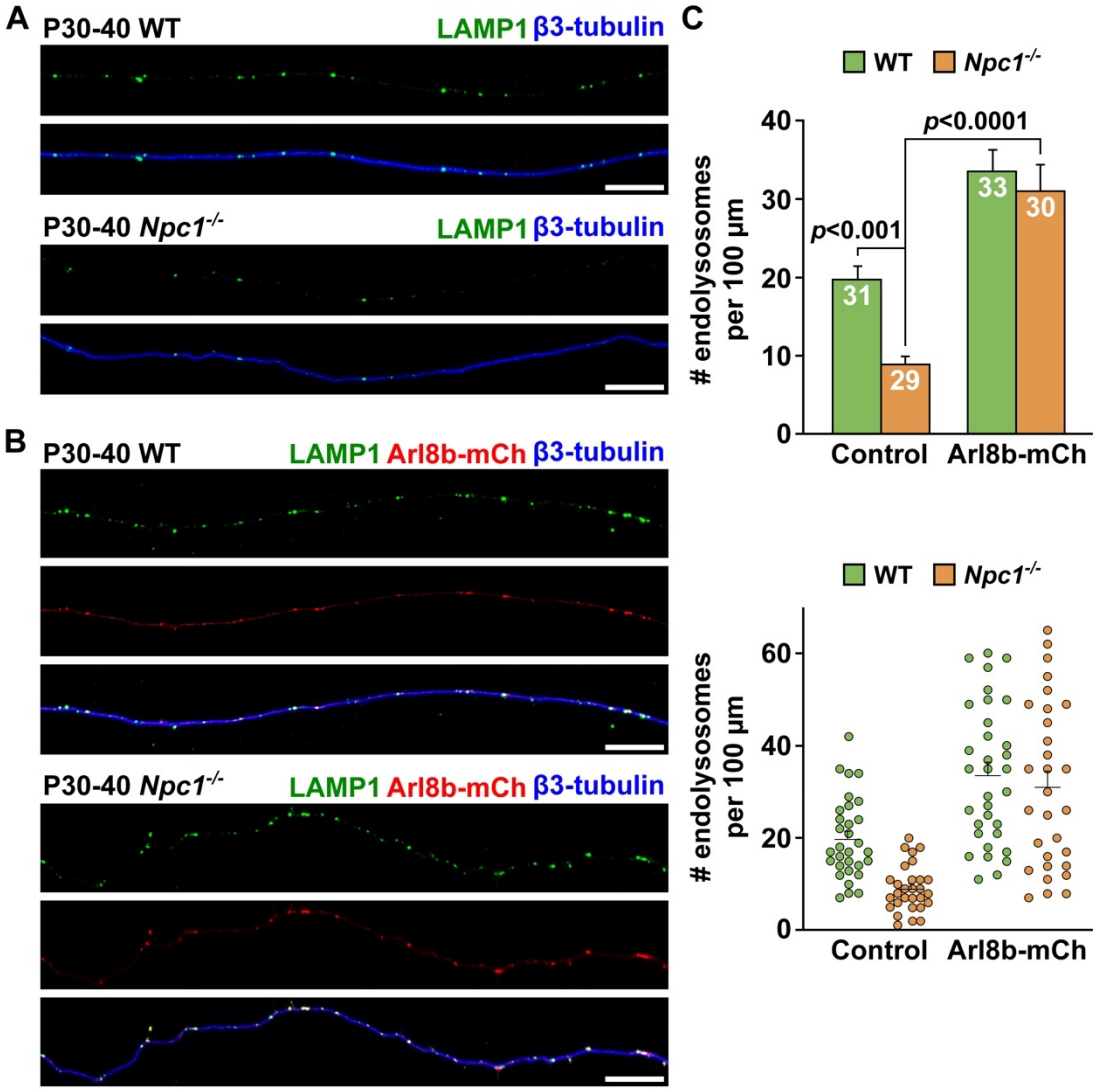


Figure 4.7 – Elevated expression of kinesin-lysosome adaptor Arl8b rescues axonal lysosome density in DRG neurons from presymptomatic Npc1$^{-/-}$ mice. *(**A-C**) Representative images (**A, B**) and quantitative analysis (**C**) showing increased axonal lysosome density with elevated Arl8b expression. DRG neurons isolated from young adult mice at P30-40 were nucleofected with Arl8b-mCh at DIV0 followed by co-immunostaining with LAMP1 and β3-tubulin at DIV3-4. Note that both WT and Npc1$^{-/-}$ neurons displayed an increase in the density of axonal lysosomes with Arl8b expression. Data were collected from the total number of axons indicated inside bars, presented as mean ± SEM with dots representing individual axons, and analyzed by one-way ANOVA. Scale bars: 10 µm.*

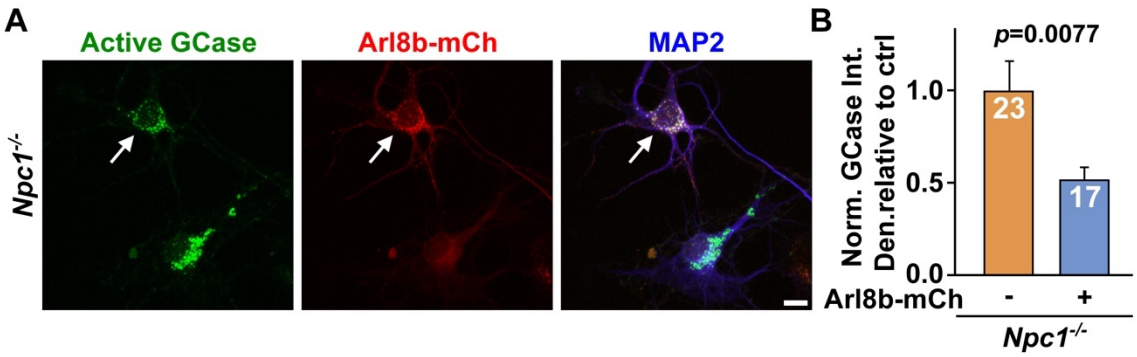


Figure 4.8 – Elevated Arl8b expression reduces lysosome accumulation in the soma of Npc1$^{-/-}$ neurons.

*(**A, B**) Representative images (**A**) and quantitative analysis (**B**) showing reduced lysosome integrated density in the soma of Npc1$^{-/-}$ cortical neurons following Arl8b expression. Neurons were transduced with a lentivirus encoding Arl8b-mCh at DIV0, loaded with MDW933 for 1 hour, followed by immunostaining for MAP2 at DIV8. Arrows indicate transduced neurons. Integrated density was analyzed in thresholded images using ImageJ, and data are presented as mean integrated density normalized to Npc1$^{-/-}$ neurons without transduction. Data were quantified from the total number of neurons shown inside bars, presented as mean ± SEM, and analyzed by Mann-Whitney test. Error bars: SEM, Scale bars: 10 µm.*

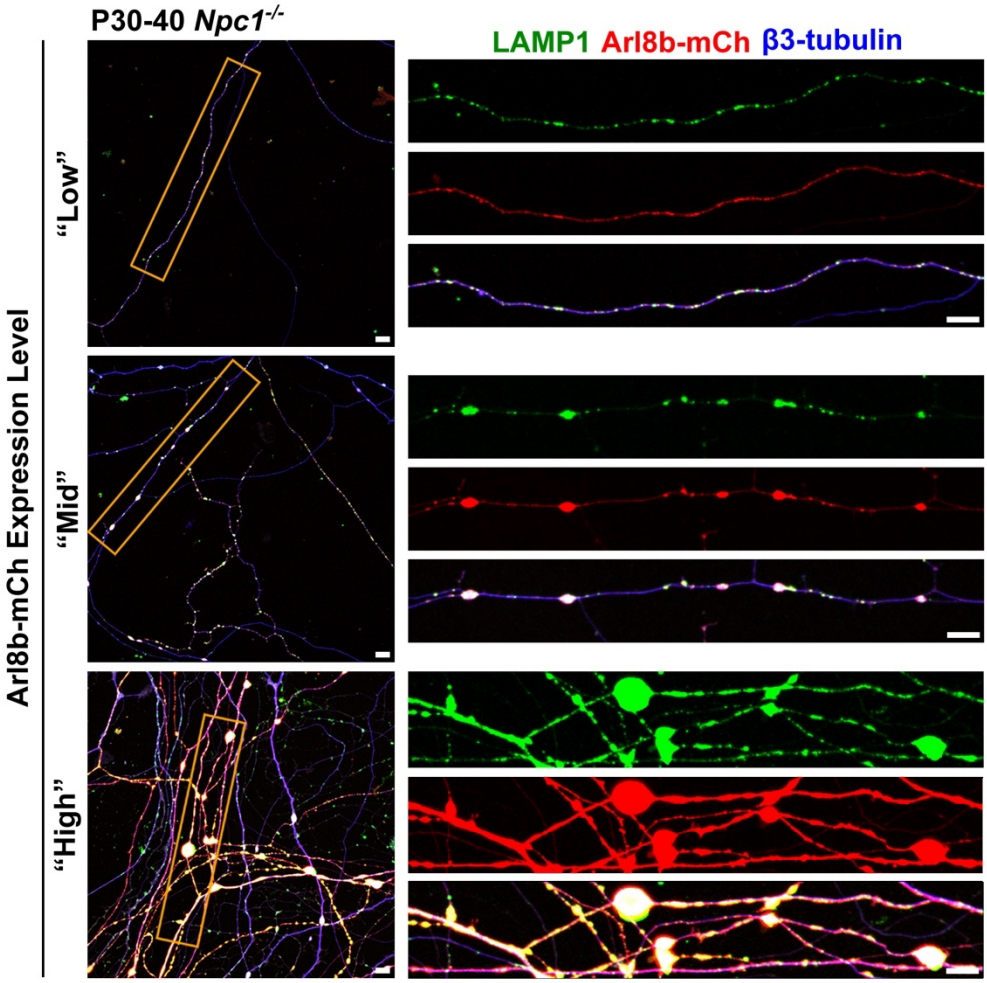


Figure 4.9 – Excessively high levels of Arl8b overexpression leads to organelle accumulation in Npc1$^{-/-}$ axons.
Representative images showing that high levels of Arl8b overexpression lead to the formation of axonal swellings in neurons isolated from presymptomatic Npc1$^{-/-}$ mice. DRG neurons at P30-40 were nucleofected with Arl8b-mCh at DIV0, followed by co-immunostaining for LAMP1 and β3 tubulin at DIV3-4. Note that neurons with Arl8b expressed at low levels do not display axonal swellings whereas higher expression levels induce axonal swelling formation. Scale bars: 10 μm.

Given that elevated cholesterol content within *Npc1*$^{-/-}$ lysosomal membranes leads to the aberrant sequestration of Arl8 from the cytosol (**Figure 3.8A**), we next tested whether facilitating lysosome transport to distal axons by elevating Arl8b expression also reduces autophagosome accumulation in *Npc1*$^{-/-}$ axons. To address this, DRG neurons cultured from presymptomatic *Npc1*$^{-/-}$ mice were nucleofected with EGFP-LC3 alone or together with Arl8b-mCh at DIV0, followed by live imaging at DIV3-4.

Consistently, elevated Arl8b expression reduced autophagosome density in *Npc1*$^{-/-}$ axons (**Figures 4.10A and 4.10B**; *Npc1*$^{-/-}$: 9.29 ± 0.57; *Npc1*$^{-/-}$ + Arl8b-mCh: 4.93 ± 0.35; $p < 0.0001$; per 100 µm axon length). These experiments suggest that facilitating lysosome transport into *Npc1*$^{-/-}$ axons is sufficient to support the maturation and clearance of axonal autophagosomes at this early presymptomatic stage.

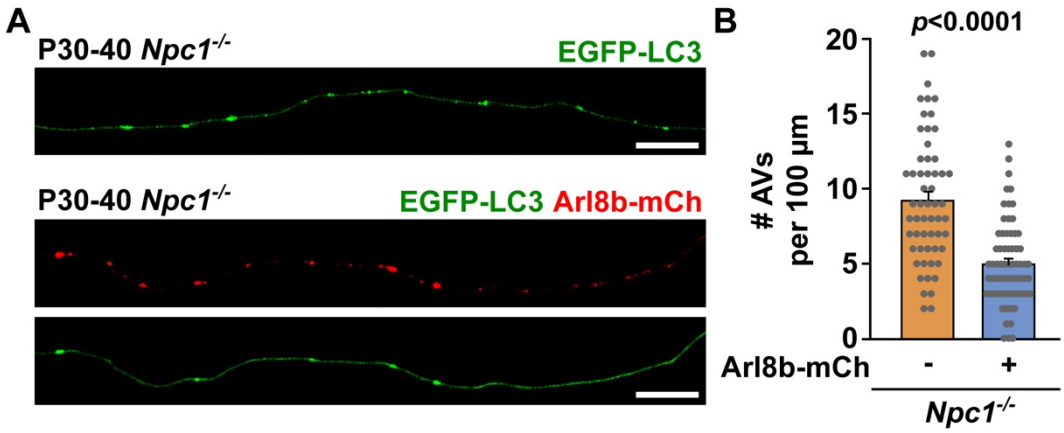


Figure 4.10 – Elevated expression of kinesin-lysosome adaptor Arl8b reduces axonal autophagic stress in DRG neurons from presymptomatic Npc1$^{-/-}$ mice. *(**A, B**) Images (**A**) and quantitative analysis (**B**) showing reduced axonal autophagic stress with elevated Arl8b expression in DRG axons from P30-40 Npc1$^{-/-}$ mice. DRG neurons were nucleofected with EGFP-LC3 or co-nucleofected with EGFP-LC3 and Arl8b-mCh at DIV0, followed by live imaging at DIV3-4. Data are presented as mean ± SEM with dots representing individual axons (Npc1$^{-/-}$ n=57, Npc1$^{-/-}$ + Arl8b-mCh n=67) and analyzed by Student's t test. Scale bars: 10 µm.*

We further examined whether elevated Arl8b expression has an impact on *Npc1*$^{-/-}$ neuron survival. Cortical neurons cultured from presymptomatic adult mice (P30-40) were transduced with lentiviruses encoding Arl8b-mCh or mCh at DIV0, followed by terminal deoxynucleotidyl transferase dUTP nick end labeling (TUNEL) assays to detect apoptotic neurons at DIV7 and DIV10. *Npc1*$^{-/-}$ neurons showed increased TUNEL-positive neuron death compared to WT at DIV7 (WT: 18.81 ± 0.64%; *Npc1*$^{-/-}$: 26.96 ± 0.80%; $p < 0.0001$) and a further increase at DIV10 (WT:

22.55 ± 0.45%; *Npc1*$^{-/-}$: 35.62 ± 0.67%; $p < 0.0001$), indicating progressive apoptosis with age in culture. However, elevated expression of Arl8b reduced *Npc1*$^{-/-}$ neuron death at DIV7 and DIV10, restoring neuron survival to levels observed in WT neurons (**Figures 4.11A and 4.11B**). Taken together, these results support a model in which a lipid-mediated impairment of lysosome transport to distal axons disrupts autophagosome maturation and clearance and thus contributes to altered axonal homeostasis and degeneration in *Npc1*$^{-/-}$ neurons.

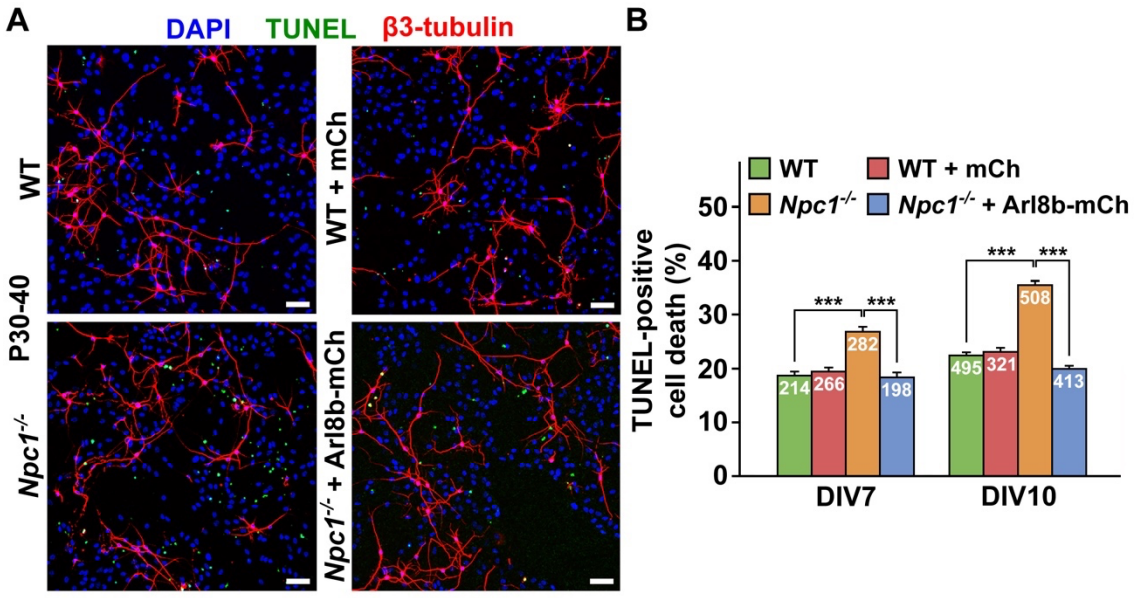


Figure 4.11 – Elevated expression of kinesin-lysosome adaptor Arl8b rescues cell death in neurons from presymptomatic Npc1$^{-/-}$ mice.

*(**A, B**) Representative images (**A**) and quantitative analysis (**B**) showing reduced TUNEL-positive Npc1$^{-/-}$ neuron death following Arl8b overexpression. Cortical neurons isolated from presymptomatic P30-40 mice were transduced at DIV0 with a lentivirus encoding Arl8b-mCh or mCh as a control. TUNEL assays were performed at DIV7 and DIV10, and the percentage of TUNEL-positive cells to total DAPI staining cells was calculated in thresholded images using ImageJ. Note that Npc1$^{-/-}$ neurons show increased apoptosis at DIV7 and further at DIV10, which was reduced with elevated Arl8b expression. Data were collected from the total number of neurons indicated in bars, presented as mean ± SEM, and analyzed by one-way ANOVA. ***p < 0.0001. Scale bars: 50 μm. Experiment carried out in collaboration with T. Sun (NINDS, NIH).*

4.4 – Discussion

Here, we demonstrate the importance of soma-derived axonal lysosomes to the maturation of axonal autophagosomes and maintenance of efficient clearance capacity within axons. We show that reducing lysosomal membrane cholesterol with HPCD, and therefore releasing Arl8/kinesin-1 sequestration on NPC somatic lysosomes, enhances axonal lysosome delivery. We further show that disrupting kinesin-mediated lysosome transport into axons by targeted knockdown of the kinesin-lysosome adaptor Arl8 induces the accumulation of autophagic cargos within axons, consistent for a role of axonal lysosomes in facilitating axonal autophagic flux (143). In line with this notion, we find that elevated Arl8b expression in NPC neurons rescues lysosome transport to distal axons by overcoming Arl8 sequestration, thereby reducing axonal autophagic stress and restoring survival of neurons from presymptomatic NPC mice. Collectively, these observations suggest that alterations in lipid composition within NPC lysosome membranes in the soma impairs their axonal delivery and positioning, thereby disrupting autophagic flux and degradation capacity within axons.

Our recent study in microfluidic devices demonstrated that soma-derived degradative lysosomes are dynamically delivered to distal axons, where they target to autophagosomes, facilitating their maturation into autolysosomes by supplying active lysosomal hydrolases (135). We propose that both the anterograde delivery of lysosomes from the soma to distal axons, as well as the retrograde trafficking of autophagic organelles that are generated at axon terminals, are essential to achieve effective maturation by organelle fusion and then clearance of autophagic organelles from axons. Consistent with this concept, we observed that NPC neurons display a reduced number of lysosomes delivered into distal axons, thus impairing maturation

and turnover of autophagic organelles during their retrograde transport route. Therefore, both the anterograde transport of lysosomes to distal axons and the retrograde transport of autophagic intermediates towards proximal regions are important to maintain axonal degradation/clearance capacity and cellular homeostasis. This concept is supported by several studies showing that impairments in either transport process lead to axonal autophagic stress and neurodegeneration (135, 136, 143, 161, 170). Together, our findings highlight that efficient clearance of axonal autophagosomes requires coordination between their retrograde transport and the anterograde delivery of soma-derived lysosomes to distal axons. This bidirectional transport model facilitates both organelles to meet and fuse during their opposing trafficking routes for efficient autophagosome maturation and removal from axons.

CHAPTER 5 – DISCUSSION

5.1 – Concluding Remarks

In this study, we reveal a lipid-mediated mechanism contributing to altered axonal homeostasis in NPC neurons. We show that abnormal lipid composition within NPC lysosome membranes in the soma sequesters motor/adaptors of axonal lysosome delivery, resulting in impaired lysosome transport into axons, leading to axonal autophagosome accumulation (**Figure 5.1**).

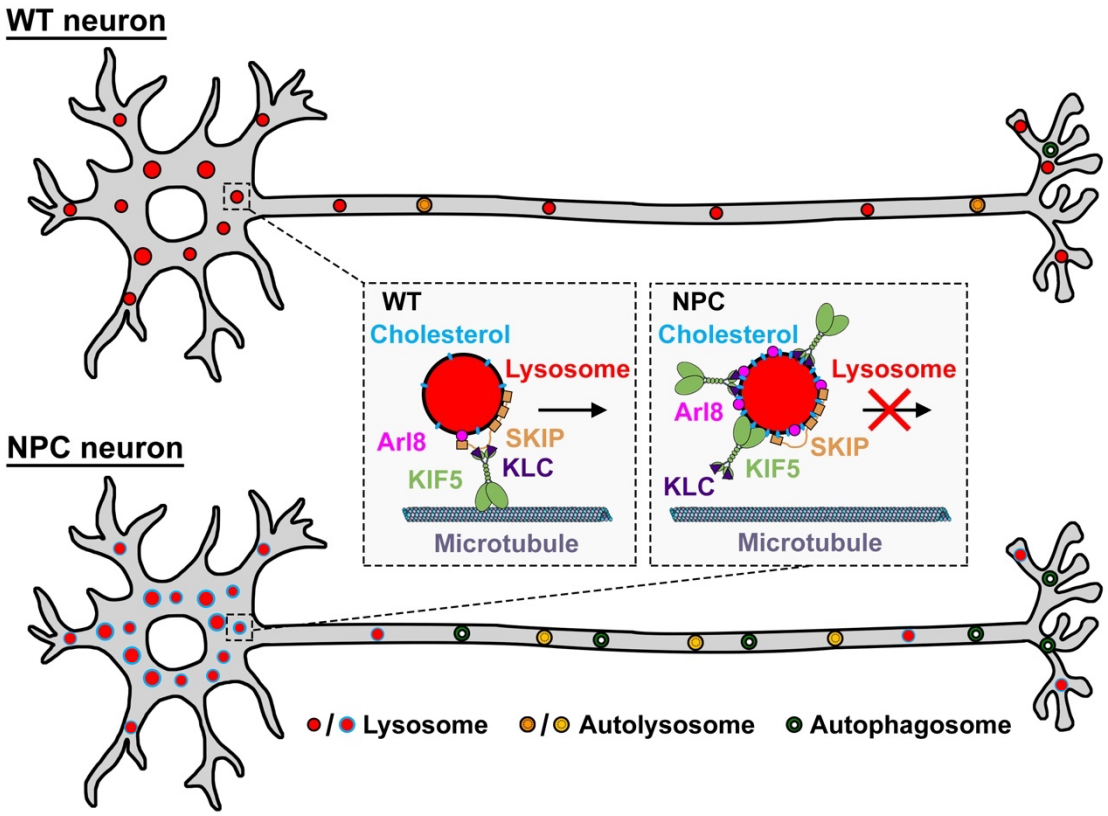


Figure 5.1 – Proposed model showing lipid-mediated sequestration of motor-adaptor proteins impairs axonal lysosome delivery, leading to autophagic stress in Npc1$^{-/-}$ axons. *In WT neurons, the Arl8/SKIP/Kinesin-1 complex is appropriately recruited to and assembled on lysosome membranes in the soma, resulting in a continuous supply of lysosomes transported into axons to facilitate axonal autophagosome maturation and clearance. In NPC neurons, altered membrane lipid composition within somatic lysosomes sequesters Arl8 and kinesin-1 but not SKIP, disrupting lysosome transport to distal axons. Inefficient lysosome delivery impairs axonal autophagosome maturation without affecting their retrograde motility, resulting in increased autophagic stress in presymptomatic NPC axons. Reducing membrane cholesterol with HPCD treatment releases*

Arl8/kinesin-1 sequestration, thereby rescuing lysosome transport into axons and reducing axonal autophagic stress in NPC.

5.1.1 – Coordinated Bidirectional Transport Maintains Axonal Homeostasis

Axonal dystrophy is a major pathological feature of common neurodegenerative diseases and LSDs associated with altered lysosome function (44, 139, 142, 186-193). In NPC mice, dystrophic axons appear early before the onset of symptoms and neurodegeneration, suggesting their active contribution to neuronal dysfunction and disease progression (44, 49). Consistent with previous studies (39, 44, 51), axonal swellings in NPC did not contain the characteristic lysosome inclusions typical of NPC lysosomes. Instead, these organelle accumulations belonged to the endo-lysosomal-autophagic pathways (51), and predominantly included multivesicular bodies, multilamellar vesicles, and autophagic vacuoles, largely representing intermediates of the endocytic and autophagic pathways. Because a global failure in axonal transport would lead to more diverse organelle accumulations, these findings suggested that impaired maturation and clearance of lysosomal substrates likely underlies early axonal pathology in NPC.

Degradation of endocytic and autophagic cargos depend on their dynamic interactions with lysosomes, which provide the acid hydrolases required for substrate degradation (60). In axons, these cargos mature as they move along a retrograde transport route toward the cell soma, where degradative lysosomes are relatively enriched (142, 154, 155, 158). Indeed, defects in retrograde transport have previously been observed to lead to impaired autophagosome clearance and buildup within dystrophic axons (136, 142, 161, 162, 170). Consistent with a defect in autophagosome maturation, we observed significant autophagosome accumulation in presymptomatic NPC axons. However, unexpectedly, these axonal

autophagosomes displayed similar motility patterns compared to control, moving predominantly in the retrograde direction toward the cell body. Because axonal autophagosome maturation is linked to their retrograde transport (142, 158), this was a surprising finding and suggested other factors contribute to the accumulation of autophagosomes in NPC axons.

Dynein-mediated autophagosome transport promotes encounters with lysosomes to facilitate efficient clearance capacity (159). Both endocytic and autophagic cargos are degraded through transient and complete fusion events with lysosomes (59, 60, 63-65, 157). Our recent study revealed that lysosomes containing active lysosomal hydrolases are continuously delivered from the cell body to distal axons, where they target to axonal autophagic cargo (135). This dynamic process facilitates autophagosome maturation into autolysosomes (135), which contain degraded substrates (135, 144, 161). Here, we observed that NPC neurons display a progressive defect in the number of lysosomes transported into axons, leading to impaired maturation of autophagic organelles traveling retrogradely along the axon. These results suggest that both the anterograde transport of lysosomes and retrograde transport of autophagosomes are coordinated to facilitate efficient autophagic flux in axons. This model is consistent with previous observations showing that retrograde (98) and anterograde (251) lysosome motility are both important for autophagic clearance. This may be particularly important in neuronal axons, which span several tens to hundreds of microns away from the cell body. Therefore, this bidirectional transport model allows efficient degradation and removal of axonal cargos during their opposing trafficking routes.

5.1.2 – Altered Membrane Lipid Composition Impairs Lysosome Delivery to NPC Axons

Impaired axonal lysosome delivery suggested a disruption to the Arl8/SKIP/kinesin-1 complex (**Figure 1.8**), which was recently demonstrated to drive lysosome transport specifically into axons (143). To elucidate mechanisms underlying altered axonal lysosome distribution, we investigated recruitment of this complex to lysosomes using STED super-resolution imaging and biochemical endolysosomal isolations. We unexpectedly observed that Arl8 and kinesin-1, but not SKIP, were aberrantly sequestered on NPC lysosomes, reflecting accumulation of improperly assembled motor-adaptor complexes on NPC lysosome membranes in the soma. Kinesin-1 requires SKIP to promote lysosome transport into axons (143), and SKIP requires Arl8 in its active GTP-bound state for binding (107). Therefore, Arl8 and kinesin-1 are likely sequestered non-functionally on NPC lysosome membranes. These observations are consistent with previous studies showing disrupted function of membrane-associated proteins in LSDs (236) including NPC (17, 218).

The stabilization of Arl8 and kinesin-1 on NPC lysosome membranes occurred in the absence of significant changes to their total protein levels, suggesting these changes were mediated locally at the lysosome membrane. Consistent with a previous study (221), we observed that NPC neuronal lysosomes show elevated membrane cholesterol levels, suggesting that altered membrane lipid composition may be driving motor-adaptor sequestration. This lipid-mediated mechanism was supported by treatment with HPCD, which reduced membrane cholesterol and released Arl8/kinesin-1 sequestration, thereby rescuing axonal lysosome delivery and reducing autophagic stress in presymptomatic NPC neurons. Given HPCD was previously reported to reduce sphingolipid accumulation in NPC1-null lysosomes

(237), it is possible that elevated sphingolipid content may also contribute to the lipid-mediated sequestration of motor-adaptors on NPC lysosome membranes.

5.1.3 – Lysosomal Dysfunction and Axonal Autophagic Stress in NPC Neurons

Inhibition of lysosomal proteolytic function by leupeptin or bafilomycin A1 treatment results in the accumulation of autophagosomes in axons, neurites, and/or the soma (142, 211, 212). These studies suggest that reduced lysosomal degradative function previously observed in NPC cells (213) may also contribute to autophagic stress in NPC axons. In addition, impaired autophagosome-late endosome fusion with intact lysosomal proteolytic function was also observed to lead to autophagosome accumulation in NPC1-deficient cells (37, 214).

While progressive lipid storage in the lysosomal lumen of NPC neurons alters lysosomal degradation capacity with disease progression, we observed a reduction in the density of degradative lysosomes but an expanded lysosomal system in the cell body in embryonic NPC cortical neurons at DIV7-8, which preceded axonal autophagosome accumulation. Subsequently, in DRG neurons isolated from adult presymptomatic NPC mice, decreased axonal lysosome density was associated with a further reduction in active lysosome density and a robust increased in axonal autophagosome density. Consistent with these observations, rescuing lysosome delivery to distal axons with elevated Arl8b expression reduced, but did not eliminate, autophagic stress in presymptomatic NPC axons. Therefore, proper lysosome positioning and function are both important to maintain axonal homeostasis.

In summary, our study supports a model in which alterations in lipid composition within lysosome membranes in the soma impairs their axonal trafficking and positioning, leading to altered axonal homeostasis in NPC (**Figure 5.1**). These

findings highlight the role of soma-derived axonal lysosomes in supporting axonal health and reveal that reducing lipid levels rescues lysosome transport into axons, thereby reducing axonal autophagosome accumulation at early stages of NPC disease.

5.2 – Future Studies

While our observations suggest that alterations within the membrane of NPC lysosomes sequester motor-adaptors of axonal lysosome delivery, the specific lipid mediating this change remains unclear. Lysosome membranes are composed of diverse lipid species classified into structural glycerosphingolipids, sphingolipids, and cholesterol (252, 253). To study lipids within the lysosome membrane, we plan to expand and adapt the biochemical strategy used to analyze the distribution of motor-adaptors on NPC lysosomes by incorporating high performance liquid chromatography (HPLC) to quantitatively profile lipid species specifically within the endolysosome population. By selectively modulating lysosomal lipid levels both pharmacologically and exogenously, this approach can be used to help broadly determine the lipid environment leading to Arl8/kinesin-1 sequestration that results in defective lysosome transport to distal axons in NPC neurons.

In addition, our results show that HPCD treatment reduces both luminal and membrane cholesterol, suggesting that stored cholesterol may also be driving the sequestration of motor-adaptor proteins on NPC lysosome membranes. A previous study observed that OSBP (oxysterol-binding protein) inhibition selectively reduces membrane cholesterol but not luminal cholesterol in NPC lysosomes (221). Therefore, determining whether OSBP inhibition impacts Arl8/kinesin-1 sequestration on NPC lysosomes will help resolve the relative contribution of luminal

versus membrane cholesterol in mediating impaired axonal lysosome delivery that contributes to altered axonal homeostasis in NPC.

Furthermore, our results show that expression of the lysosome-kinesin adaptor Arl8b rescues lysosome transport into axons, reduces axonal autophagic stress, and improves survival in neurons isolated from presymptomatic NPC mice. However, whether elevated Arl8b expression delays disease progression and neurodegeneration in NPC mice remains unknown. Given that *Npc1* null mice represent a well-characterized model with defined disease manifestations (**Figure 1.3**), this makes it an ideal candidate for an *in vivo*, proof-of-concept study. Therefore, it will be of interest to evaluate the impact of AAV9-Arl8b on disease-onset and lifespan in this mouse model. This may help determine the importance of soma-derived axonal lysosomes to the maintenance of axonal homeostasis in NPC *in vivo*.

APPENDICES

Appendix 1

Genotyping Primer Sequences

GENE	DIRECTION	SEQUENCE (5' to 3')
Npc1	Forward	GGTGCTGGACAGCCAAGTA
	Reverse	GATGGTCTGTTCTCCCATG

Cloning Primer Sequences

GENE INSERT	DIRECTION	SEQUENCE (5' to 3')
Arl8b-mCh	Forward	ATAAGAATGCGGCCGCGCCAAAA TGCTGGCGCTCATCTCCCGCC
	Reverse	CGACGCGTCGCTACTTGTACAGC TCGTCCATGCC
mCh	Forward	ATAAGAATCGGCCGCGCCAAAAT GGTGAGCAAGGGCGAGGAG
	Reverse	CGACGCGTCGCTACTTGTACAGC TCGTCCATGCC

siRNA Oligonucleotide Sequences

TARGET	SEQUENCE (5' to 3')
Arl8a	GCAUCCCGGUCUUAGUCCUUGGUAA
Arl8b	CAGGAUAGAGAAAUUUGCUGCUAUU

Appendix 2

Primary Antibodies

PRIMARY ANTIBODY	SUPPLIER	CATALOG NUMBER
Mouse monoclonal anti-β3-tubulin	Sigma-Aldrich	Cat#T8578; RRID: AB_1841228
Mouse monoclonal anti-beta-actin	Novus	Cat#NB600-501; RRID: AB_10077656
Mouse monoclonal anti-GAPDH	Millipore	Cat#CB1001; RRID: AB_2107426
Mouse monoclonal anti-Kinesin Heavy Chain	Millipore	Cat#MAB1614; RRID: AB_94284
Mouse monoclonal anti-LAMP1	Cell Signaling Technology	Cat#15665; RRID: AB_2798750
Mouse monoclonal anti-MAP2	BD Biosciences	Cat#556320; RRID: AB_396359
Rabbit polyclonal anti-Arl8	Proteintech	Cat#13049-1-AP; RRID: AB_2059000
Rabbit polyclonal anti-GFP	Abcam	Cat# ab6556; RRID: AB_305564
Rabbit polyclonal anti-Glucocerebrosidase	Sigma-Aldrich	Cat#G4171; RRID: AB_1078958
Rabbit polyclonal anti-LAMP1	Abcam	Cat#ab24170; RRID: AB_775978
Rabbit monoclonal anti-Niemann-Pick C1	Abcam	Cat#ab134113; RRID: AB_2734695
Rabbit polyclonal anti-SKIP (PLEKHM2)	Abcam	Cat#ab91581; RRID: AB_2050192
Rabbit polyclonal anti-SKIP (PLEKHM2)	Thermo Fisher Scientific	Cat#PA5-20850; RRID: AB_11153975
Rat monoclonal anti-LAMP1	Developmental Studies Hybridoma Bank	Cat#1D4B; RRID: AB_2134500

Secondary Antibodies

SECONDARY ANTIBODY	SUPPLIER	CATALOG NUMBER
Donkey polyclonal anti-rabbit IgG, highly cross-adsorbed secondary antibody, Alexa Fluor 488	Thermo Fisher Scientific	Cat# A-21206, RRID: AB_2535792
Goat polyclonal anti-mouse IgG, cross-adsorbed secondary antibody, Alexa Fluor 488	Thermo Fisher Scientific	Cat#A-11017; RRID: AB_2534084
Goat polyclonal anti-mouse IgG, cross-adsorbed secondary antibody, Alexa Fluor 546	Thermo Fisher Scientific	Cat#A-11018; RRID: AB_2534085
Goat polyclonal anti-mouse IgG, cross-adsorbed secondary antibody, Alexa Fluor 594	Thermo Fisher Scientific	Cat# A-11005; RRID: AB_2534073
Goat polyclonal anti-rabbit IgG, cross-adsorbed secondary antibody, Alexa Fluor 555	Thermo Fisher Scientific	Cat#A-21428; RRID: AB_2535849
Goat polyclonal anti-rabbit IgG, highly cross-adsorbed secondary antibody, Alexa Fluor 594	Thermo Fisher Scientific	Cat# A-11037; RRID: AB_2534095
Goat polyclonal anti-mouse IgG, highly cross-adsorbed secondary antibody, Alexa Fluor 647	Thermo Fisher Scientific	Cat#A-21236; RRID: AB_2535805
Goat polyclonal anti-rabbit IgG, highly cross-adsorbed secondary antibody, Alexa Fluor 647	Thermo Fisher Scientific	Cat#A-21245; RRID: AB_2535813
Goat polyclonal anti-rat IgG, cross-adsorbed secondary antibody, Alexa Fluor 488	Thermo Fisher Scientific	Cat#A-11006; RRID: AB_2534074
Sheep anti-mouse IgG, HRP-linked	GE Healthcare	Cat#NA931; RRID: AB_772210
Donkey anti-rabbit IgG, HRP-linked	GE Healthcare	Cat#NA934; RRID: AB_772206

PEER-REVIEWED PUBLICATIONS

1. Farfel-Becker T, **Roney JC**, Cheng XT, Li S, Cuddy SR, Sheng ZH. Neuronal soma-derived degradative lysosomes are continuously delivered to distal axons to maintain local degradation capacity. *Cell Reports* 2019 Jul 2;28(1):51-64.e4.

2. Farfel-Becker T, **Roney JC**, Cheng XT, Li S, Cuddy SR, Sheng ZH. The secret life of degradative lysosomes in axons: delivery from the soma, enzymatic activity, and local autophagic clearance. *Autophagy* 2020 Jan;16(1):167-168.

3. **Roney JC**, Farfel-Becker T, Li S, Sun T, Huang N, Xie Y, Lin MY, Platt FM, Sheng ZH. Lipid-mediated sequestration of motor-adaptor proteins impairs axonal lysosome delivery leading to autophagic stress and axonal dystrophy in Niemann-Pick disease type C neurons. *Under review.*

REFERENCES

1. Platt FM, d'Azzo A, Davidson BL, Neufeld EF, Tifft CJ. Lysosomal storage diseases. Nat Rev Dis Primers. 2018;4(1):27.
2. Cox TM, Cachon-Gonzalez MB. The cellular pathology of lysosomal diseases. J Pathol. 2012;226(2):241-54.
3. Platt FM, Boland B, van der Spoel AC. The cell biology of disease: lysosomal storage disorders: the cellular impact of lysosomal dysfunction. J Cell Biol. 2012;199(5):723-34.
4. Ferreira CR, Gahl WA. Lysosomal storage diseases. Transl Sci Rare Dis. 2017;2(1-2):1-71.
5. Platt FM. Emptying the stores: lysosomal diseases and therapeutic strategies. Nat Rev Drug Discov. 2018;17(2):133-50.
6. Futerman AH, van Meer G. The cell biology of lysosomal storage disorders. Nat Rev Mol Cell Biol. 2004;5(7):554-65.
7. Parenti G, Andria G, Ballabio A. Lysosomal storage diseases: from pathophysiology to therapy. Annu Rev Med. 2015;66:471-86.
8. Fuller M, Meikle PJ, Hopwood JJ. Epidemiology of lysosomal storage diseases: an overview. In: Mehta A, Beck M, Sunder-Plassmann G, editors. Fabry Disease: Perspectives from 5 Years of FOS. Oxford2006.
9. Meikle PJ, Hopwood JJ, Clague AE, Carey WF. Prevalence of lysosomal storage disorders. JAMA. 1999;281(3):249-54.
10. Vanier MT. Niemann-Pick disease type C. Orphanet J Rare Dis. 2010;5:16.
11. Wraith JE. Lysosomal disorders. Semin Neonatol. 2002;7(1):75-83.
12. Boustany RM. Lysosomal storage diseases--the horizon expands. Nat Rev Neurol. 2013;9(10):583-98.
13. Borger DK, McMahon B, Roshan Lal T, Serra-Vinardell J, Aflaki E, Sidransky E. Induced pluripotent stem cell models of lysosomal storage disorders. Dis Model Mech. 2017;10(6):691-704.
14. Pastores GM, Torres PA, Zeng BJ. Animal models for lysosomal storage disorders. Biochemistry (Mosc). 2013;78(7):721-5.
15. Hemsley KM, Hopwood JJ. Lessons learnt from animal models: pathophysiology of neuropathic lysosomal storage disorders. J Inherit Metab Dis. 2010;33(4):363-71.
16. Platt FM. Sphingolipid lysosomal storage disorders. Nature. 2014;510(7503):68-75.
17. te Vruchte D, Lloyd-Evans E, Veldman RJ, Neville DC, Dwek RA, Platt FM, et al. Accumulation of glycosphingolipids in Niemann-Pick C disease disrupts endosomal transport. J Biol Chem. 2004;279(25):26167-75.
18. Butler JD, Vanier MT, Pentchev PG. Niemann-Pick C disease: cystine and lipids accumulate in the murine model of this lysosomal cholesterol lipidosis. Biochem Biophys Res Commun. 1993;196(1):154-9.
19. Vanier MT, Millat G. Niemann-Pick disease type C. Clin Genet. 2003;64(4):269-81.
20. Wassif CA, Cross JL, Iben J, Sanchez-Pulido L, Cougnoux A, Platt FM, et al. High incidence of unrecognized visceral/neurological late-onset Niemann-Pick disease, type C1, predicted by analysis of massively parallel sequencing data sets. Genet Med. 2016;18(1):41-8.
21. Mengel E, Klunemann HH, Lourenco CM, Hendriksz CJ, Sedel F, Walterfang M, et al. Niemann-Pick disease type C symptomatology: an expert-based clinical description. Orphanet J Rare Dis. 2013;8:166.

22. Carstea ED, Morris JA, Coleman KG, Loftus SK, Zhang D, Cummings C, et al. Niemann-Pick C1 disease gene: homology to mediators of cholesterol homeostasis. Science. 1997;277(5323):228-31.
23. Loftus SK, Morris JA, Carstea ED, Gu JZ, Cummings C, Brown A, et al. Murine model of Niemann-Pick C disease: mutation in a cholesterol homeostasis gene. Science. 1997;277(5323):232-5.
24. Naureckiene S, Sleat DE, Lackland H, Fensom A, Vanier MT, Wattiaux R, et al. Identification of HE1 as the second gene of Niemann-Pick C disease. Science. 2000;290(5500):2298-301.
25. Carstea ED, Polymeropoulos MH, Parker CC, Detera-Wadleigh SD, O'Neill RR, Patterson MC, et al. Linkage of Niemann-Pick disease type C to human chromosome 18. Proc Natl Acad Sci U S A. 1993;90(5):2002-4.
26. Neufeld EB, Wastney M, Patel S, Suresh S, Cooney AM, Dwyer NK, et al. The Niemann-Pick C1 protein resides in a vesicular compartment linked to retrograde transport of multiple lysosomal cargo. J Biol Chem. 1999;274(14):9627-35.
27. Higgins ME, Davies JP, Chen FW, Ioannou YA. Niemann-Pick C1 is a late endosome-resident protein that transiently associates with lysosomes and the trans-Golgi network. Mol Genet Metab. 1999;68(1):1-13.
28. Infante RE, Wang ML, Radhakrishnan A, Kwon HJ, Brown MS, Goldstein JL. NPC2 facilitates bidirectional transfer of cholesterol between NPC1 and lipid bilayers, a step in cholesterol egress from lysosomes. Proc Natl Acad Sci U S A. 2008;105(40):15287-92.
29. Ioannou YA. The structure and function of the Niemann-Pick C1 protein. Mol Genet Metab. 2000;71(1-2):175-81.
30. Davies JP, Chen FW, Ioannou YA. Transmembrane molecular pump activity of Niemann-Pick C1 protein. Science. 2000;290(5500):2295-8.
31. Lloyd-Evans E, Morgan AJ, He X, Smith DA, Elliot-Smith E, Sillence DJ, et al. Niemann-Pick disease type C1 is a sphingosine storage disease that causes deregulation of lysosomal calcium. Nat Med. 2008;14(11):1247-55.
32. Lu F, Liang Q, Abi-Mosleh L, Das A, De Brabander JK, Goldstein JL, et al. Identification of NPC1 as the target of U18666A, an inhibitor of lysosomal cholesterol export and Ebola infection. Elife. 2015;4.
33. Morgan AJ, Platt FM, Lloyd-Evans E, Galione A. Molecular mechanisms of endolysosomal Ca2+ signalling in health and disease. Biochem J. 2011;439(3):349-74.
34. Piper RC, Luzio JP. CUPpling calcium to lysosomal biogenesis. Trends Cell Biol. 2004;14(9):471-3.
35. Lloyd-Evans E, Platt FM. Lysosomal Ca(2+) homeostasis: role in pathogenesis of lysosomal storage diseases. Cell Calcium. 2011;50(2):200-5.
36. Goldman SD, Krise JP. Niemann-Pick C1 functions independently of Niemann-Pick C2 in the initial stage of retrograde transport of membrane-impermeable lysosomal cargo. J Biol Chem. 2010;285(7):4983-94.
37. Sarkar S, Carroll B, Buganim Y, Maetzel D, Ng AH, Cassady JP, et al. Impaired autophagy in the lipid-storage disorder Niemann-Pick type C1 disease. Cell Rep. 2013;5(5):1302-15.
38. Baudry M, Yao Y, Simmons D, Liu J, Bi X. Postnatal development of inflammation in a murine model of Niemann-Pick type C disease: immunohistochemical observations of microglia and astroglia. Exp Neurol. 2003;184(2):887-903.
39. Walkley SU, Suzuki K. Consequences of NPC1 and NPC2 loss of function in mammalian neurons. Biochim Biophys Acta. 2004;1685(1-3):48-62.

40. Morris MD, Bhuvaneswaran C, Shio H, Fowler S. Lysosome lipid storage disorder in NCTR-BALB/c mice. I. Description of the disease and genetics. Am J Pathol. 1982;108(2):140-9.
41. Voikar V, Rauvala H, Ikonen E. Cognitive deficit and development of motor impairment in a mouse model of Niemann-Pick type C disease. Behav Brain Res. 2002;132(1):1-10.
42. Platt N, Speak AO, Colaco A, Gray J, Smith DA, Williams IM, et al. Immune dysfunction in Niemann-Pick disease type C. J Neurochem. 2016;136 Suppl 1:74-80.
43. Pressey SN, Smith DA, Wong AM, Platt FM, Cooper JD. Early glial activation, synaptic changes and axonal pathology in the thalamocortical system of Niemann-Pick type C1 mice. Neurobiol Dis. 2012;45(3):1086-100.
44. Walkley SU, Sikora J, Micsenyi M, Davidson C, Dobrenis K. Lysosomal compromise and brain dysfunction: examining the role of neuroaxonal dystrophy. Biochem Soc Trans. 2010;38(6):1436-41.
45. Walkley SU. Cellular pathology of lysosomal storage disorders. Brain Pathol. 1998;8(1):175-93.
46. Sleat DE, Wiseman JA, El-Banna M, Price SM, Verot L, Shen MM, et al. Genetic evidence for nonredundant functional cooperativity between NPC1 and NPC2 in lipid transport. Proc Natl Acad Sci U S A. 2004;101(16):5886-91.
47. Weintraub H, Abramovici A, Sandbank U, Pentchev PG, Brady RO, Sekine M, et al. Neurological mutation characterized by dysmyelination in NCTR-Balb/C mouse with lysosomal lipid storage disease. J Neurochem. 1985;45(3):665-72.
48. Karten B, Vance DE, Campenot RB, Vance JE. Cholesterol accumulates in cell bodies, but is decreased in distal axons, of Niemann-Pick C1-deficient neurons. J Neurochem. 2002;83(5):1154-63.
49. Walkley SU, Baker HJ, Rattazzi MC, Haskins ME, Wu JY. Neuroaxonal dystrophy in neuronal storage disorders: evidence for major GABAergic neuron involvement. J Neurol Sci. 1991;104(1):1-8.
50. Ohara S, Ukita Y, Ninomiya H, Ohno K. Axonal dystrophy of dorsal root ganglion sensory neurons in a mouse model of Niemann-Pick disease type C. Exp Neurol. 2004;187(2):289-98.
51. Boland B, Platt FM. Bridging the age spectrum of neurodegenerative storage diseases. Best Pract Res Clin Endocrinol Metab. 2015;29(2):127-43.
52. Settembre C, Fraldi A, Medina DL, Ballabio A. Signals from the lysosome: a control centre for cellular clearance and energy metabolism. Nat Rev Mol Cell Biol. 2013;14(5):283-96.
53. Perera RM, Zoncu R. The Lysosome as a Regulatory Hub. Annu Rev Cell Dev Biol. 2016;32:223-53.
54. Ballabio A, Bonifacino JS. Lysosomes as dynamic regulators of cell and organismal homeostasis. Nat Rev Mol Cell Biol. 2020;21(2):101-18.
55. Wartosch L, Bright NA, Luzio JP. Lysosomes. Curr Biol. 2015;25(8):R315-6.
56. Bright NA, Davis LJ, Luzio JP. Endolysosomes Are the Principal Intracellular Sites of Acid Hydrolase Activity. Curr Biol. 2016;26(17):2233-45.
57. Gruenberg J. The endocytic pathway: a mosaic of domains. Nat Rev Mol Cell Biol. 2001;2(10):721-30.
58. Mellman I. Endocytosis and molecular sorting. Annu Rev Cell Dev Biol. 1996;12:575-625.
59. Huotari J, Helenius A. Endosome maturation. EMBO J. 2011;30(17):3481-500.
60. Luzio JP, Pryor PR, Bright NA. Lysosomes: fusion and function. Nat Rev Mol Cell Biol. 2007;8(8):622-32.

61. Saftig P, Klumperman J. Lysosome biogenesis and lysosomal membrane proteins: trafficking meets function. Nat Rev Mol Cell Biol. 2009;10(9):623-35.
62. Luzio JP, Hackmann Y, Dieckmann NM, Griffiths GM. The biogenesis of lysosomes and lysosome-related organelles. Cold Spring Harb Perspect Biol. 2014;6(9):a016840.
63. Bright NA, Gratian MJ, Luzio JP. Endocytic delivery to lysosomes mediated by concurrent fusion and kissing events in living cells. Curr Biol. 2005;15(4):360-5.
64. Futter CE, Pearse A, Hewlett LJ, Hopkins CR. Multivesicular endosomes containing internalized EGF-EGF receptor complexes mature and then fuse directly with lysosomes. J Cell Biol. 1996;132(6):1011-23.
65. Bright NA, Reaves BJ, Mullock BM, Luzio JP. Dense core lysosomes can fuse with late endosomes and are re-formed from the resultant hybrid organelles. J Cell Sci. 1997;110 (Pt 17):2027-40.
66. Woodman PG, Futter CE. Multivesicular bodies: co-ordinated progression to maturity. Curr Opin Cell Biol. 2008;20(4):408-14.
67. Rink J, Ghigo E, Kalaidzidis Y, Zerial M. Rab conversion as a mechanism of progression from early to late endosomes. Cell. 2005;122(5):735-49.
68. Poteryaev D, Datta S, Ackema K, Zerial M, Spang A. Identification of the switch in early-to-late endosome transition. Cell. 2010;141(3):497-508.
69. Klionsky DJ, Emr SD. Autophagy as a regulated pathway of cellular degradation. Science. 2000;290(5497):1717-21.
70. Levine B, Klionsky DJ. Development by self-digestion: molecular mechanisms and biological functions of autophagy. Dev Cell. 2004;6(4):463-77.
71. Shibutani ST, Yoshimori T. A current perspective of autophagosome biogenesis. Cell Res. 2014;24(1):58-68.
72. De Duve C, Wattiaux R. Functions of lysosomes. Annu Rev Physiol. 1966;28:435-92.
73. Klionsky DJ, Abdelmohsen K, Abe A, Abedin MJ, Abeliovich H, Acevedo Arozena A, et al. Guidelines for the use and interpretation of assays for monitoring autophagy (3rd edition). Autophagy. 2016;12(1):1-222.
74. Sardiello M, Palmieri M, di Ronza A, Medina DL, Valenza M, Gennarino VA, et al. A gene network regulating lysosomal biogenesis and function. Science. 2009;325(5939):473-7.
75. Martina JA, Diab HI, Lishu L, Jeong AL, Patange S, Raben N, et al. The nutrient-responsive transcription factor TFE3 promotes autophagy, lysosomal biogenesis, and clearance of cellular debris. Sci Signal. 2014;7(309):ra9.
76. Braulke T, Bonifacino JS. Sorting of lysosomal proteins. Biochim Biophys Acta. 2009;1793(4):605-14.
77. Kornfeld S, Mellman I. The biogenesis of lysosomes. Annu Rev Cell Biol. 1989;5:483-525.
78. Reczek D, Schwake M, Schroder J, Hughes H, Blanz J, Jin X, et al. LIMP-2 is a receptor for lysosomal mannose-6-phosphate-independent targeting of beta-glucocerebrosidase. Cell. 2007;131(4):770-83.
79. Lefrancois S, Zeng J, Hassan AJ, Canuel M, Morales CR. The lysosomal trafficking of sphingolipid activator proteins (SAPs) is mediated by sortilin. EMBO J. 2003;22(24):6430-7.
80. Dittmer F, Ulbrich EJ, Hafner A, Schmahl W, Meister T, Pohlmann R, et al. Alternative mechanisms for trafficking of lysosomal enzymes in mannose 6-phosphate receptor-deficient mice are cell type-specific. J Cell Sci. 1999;112 (Pt 10):1591-7.

81. Hunziker W, Geuze HJ. Intracellular trafficking of lysosomal membrane proteins. Bioessays. 1996;18(5):379-89.
82. Desjardins M, Huber LA, Parton RG, Griffiths G. Biogenesis of phagolysosomes proceeds through a sequential series of interactions with the endocytic apparatus. J Cell Biol. 1994;124(5):677-88.
83. Kinchen JM, Ravichandran KS. Phagosome maturation: going through the acid test. Nat Rev Mol Cell Biol. 2008;9(10):781-95.
84. Flannagan RS, Jaumouille V, Grinstein S. The cell biology of phagocytosis. Annu Rev Pathol. 2012;7:61-98.
85. Chow A, Toomre D, Garrett W, Mellman I. Dendritic cell maturation triggers retrograde MHC class II transport from lysosomes to the plasma membrane. Nature. 2002;418(6901):988-94.
86. Vyas JM, Kim YM, Artavanis-Tsakonas K, Love JC, Van der Veen AG, Ploegh HL. Tubulation of class II MHC compartments is microtubule dependent and involves multiple endolysosomal membrane proteins in primary dendritic cells. J Immunol. 2007;178(11):7199-210.
87. Mrakovic A, Kay JG, Furuya W, Brumell JH, Botelho RJ. Rab7 and Arl8 GTPases are necessary for lysosome tubulation in macrophages. Traffic. 2012;13(12):1667-79.
88. Saric A, Hipolito VE, Kay JG, Canton J, Antonescu CN, Botelho RJ. mTOR controls lysosome tubulation and antigen presentation in macrophages and dendritic cells. Mol Biol Cell. 2016;27(2):321-33.
89. Davis LC, Morgan AJ, Galione A. NAADP-regulated two-pore channels drive phagocytosis through endo-lysosomal Ca(2+) nanodomains, calcineurin and dynamin. EMBO J. 2020;39(14):e104058.
90. Pu J, Guardia CM, Keren-Kaplan T, Bonifacino JS. Mechanisms and functions of lysosome positioning. J Cell Sci. 2016;129(23):4329-39.
91. Matteoni R, Kreis TE. Translocation and clustering of endosomes and lysosomes depends on microtubules. J Cell Biol. 1987;105(3):1253-65.
92. Harada A, Takei Y, Kanai Y, Tanaka Y, Nonaka S, Hirokawa N. Golgi vesiculation and lysosome dispersion in cells lacking cytoplasmic dynein. J Cell Biol. 1998;141(1):51-9.
93. Hollenbeck PJ, Swanson JA. Radial extension of macrophage tubular lysosomes supported by kinesin. Nature. 1990;346(6287):864-6.
94. Vale RD, Milligan RA. The way things move: looking under the hood of molecular motor proteins. Science. 2000;288(5463):88-95.
95. Bonifacino JS, Neefjes J. Moving and positioning the endolysosomal system. Curr Opin Cell Biol. 2017;47:1-8.
96. Zoncu R, Bar-Peled L, Efeyan A, Wang S, Sancak Y, Sabatini DM. mTORC1 senses lysosomal amino acids through an inside-out mechanism that requires the vacuolar H(+)-ATPase. Science. 2011;334(6056):678-83.
97. Sancak Y, Bar-Peled L, Zoncu R, Markhard AL, Nada S, Sabatini DM. Ragulator-Rag complex targets mTORC1 to the lysosomal surface and is necessary for its activation by amino acids. Cell. 2010;141(2):290-303.
98. Korolchuk VI, Saiki S, Lichtenberg M, Siddiqi FH, Roberts EA, Imarisio S, et al. Lysosomal positioning coordinates cellular nutrient responses. Nat Cell Biol. 2011;13(4):453-60.
99. Heuser J. Changes in lysosome shape and distribution correlated with changes in cytoplasmic pH. J Cell Biol. 1989;108(3):855-64.
100. Johnson DE, Ostrowski P, Jaumouille V, Grinstein S. The position of lysosomes within the cell determines their luminal pH. J Cell Biol. 2016;212(6):677-92.

101. Miki H, Setou M, Kaneshiro K, Hirokawa N. All kinesin superfamily protein, KIF, genes in mouse and human. Proc Natl Acad Sci U S A. 2001;98(13):7004-11.
102. Lawrence CJ, Dawe RK, Christie KR, Cleveland DW, Dawson SC, Endow SA, et al. A standardized kinesin nomenclature. J Cell Biol. 2004;167(1):19-22.
103. Hirokawa N, Noda Y. Intracellular transport and kinesin superfamily proteins, KIFs: structure, function, and dynamics. Physiol Rev. 2008;88(3):1089-118.
104. Hirokawa N, Niwa S, Tanaka Y. Molecular motors in neurons: transport mechanisms and roles in brain function, development, and disease. Neuron. 2010;68(4):610-38.
105. Kanai Y, Okada Y, Tanaka Y, Harada A, Terada S, Hirokawa N. KIF5C, a novel neuronal kinesin enriched in motor neurons. J Neurosci. 2000;20(17):6374-84.
106. Pu J, Schindler C, Jia R, Jarnik M, Backlund P, Bonifacino JS. BORC, a multisubunit complex that regulates lysosome positioning. Dev Cell. 2015;33(2):176-88.
107. Rosa-Ferreira C, Munro S. Arl8 and SKIP act together to link lysosomes to kinesin-1. Dev Cell. 2011;21(6):1171-8.
108. Filipek PA, de Araujo MEG, Vogel GF, De Smet CH, Eberharter D, Rebsamen M, et al. LAMTOR/Ragulator is a negative regulator of Arl8b- and BORC-dependent late endosomal positioning. J Cell Biol. 2017;216(12):4199-215.
109. Pu J, Keren-Kaplan T, Bonifacino JS. A Ragulator-BORC interaction controls lysosome positioning in response to amino acid availability. J Cell Biol. 2017;216(12):4183-97.
110. Mannan AU, Krawen P, Sauter SM, Boehm J, Chronowska A, Paulus W, et al. ZFYVE27 (SPG33), a novel spastin-binding protein, is mutated in hereditary spastic paraplegia. Am J Hum Genet. 2006;79(2):351-7.
111. Blackstone C, O'Kane CJ, Reid E. Hereditary spastic paraplegias: membrane traffic and the motor pathway. Nat Rev Neurosci. 2011;12(1):31-42.
112. Raiborg C, Wenzel EM, Pedersen NM, Stenmark H. ER-endosome contact sites in endosome positioning and protrusion outgrowth. Biochem Soc Trans. 2016;44(2):441-6.
113. Matsuzaki F, Shirane M, Matsumoto M, Nakayama KI. Protrudin serves as an adaptor molecule that connects KIF5 and its cargoes in vesicular transport during process formation. Mol Biol Cell. 2011;22(23):4602-20.
114. Raiborg C, Wenzel EM, Pedersen NM, Olsvik H, Schink KO, Schultz SW, et al. Repeated ER-endosome contacts promote endosome translocation and neurite outgrowth. Nature. 2015;520(7546):234-8.
115. Hong Z, Pedersen NM, Wang L, Torgersen ML, Stenmark H, Raiborg C. PtdIns3P controls mTORC1 signaling through lysosomal positioning. J Cell Biol. 2017;216(12):4217-33.
116. Palomo-Guerrero M, Fado R, Casas M, Perez-Montero M, Baena M, Helmer PO, et al. Sensing of nutrients by CPT1C regulates late endosome/lysosome anterograde transport and axon growth. Elife. 2019;8.
117. Karki S, Holzbaur EL. Cytoplasmic dynein and dynactin in cell division and intracellular transport. Curr Opin Cell Biol. 1999;11(1):45-53.
118. Burkhardt JK, Echeverri CJ, Nilsson T, Vallee RB. Overexpression of the dynamitin (p50) subunit of the dynactin complex disrupts dynein-dependent maintenance of membrane organelle distribution. J Cell Biol. 1997;139(2):469-84.
119. Johansson M, Rocha N, Zwart W, Jordens I, Janssen L, Kuijl C, et al. Activation of endosomal dynein motors by stepwise assembly of Rab7-RILP-p150Glued, ORP1L, and the receptor betalII spectrin. J Cell Biol. 2007;176(4):459-71.

120. Muresan V, Stankewich MC, Steffen W, Morrow JS, Holzbaur EL, Schnapp BJ. Dynactin-dependent, dynein-driven vesicle transport in the absence of membrane proteins: a role for spectrin and acidic phospholipids. Mol Cell. 2001;7(1):173-83.
121. Rocha N, Kuijl C, van der Kant R, Janssen L, Houben D, Janssen H, et al. Cholesterol sensor ORP1L contacts the ER protein VAP to control Rab7-RILP-p150 Glued and late endosome positioning. J Cell Biol. 2009;185(7):1209-25.
122. Li X, Rydzewski N, Hider A, Zhang X, Yang J, Wang W, et al. A molecular mechanism to regulate lysosome motility for lysosome positioning and tubulation. Nat Cell Biol. 2016;18(4):404-17.
123. Sun M, Goldin E, Stahl S, Falardeau JL, Kennedy JC, Acierno JS, Jr., et al. Mucolipidosis type IV is caused by mutations in a gene encoding a novel transient receptor potential channel. Hum Mol Genet. 2000;9(17):2471-8.
124. Altarescu G, Sun M, Moore DF, Smith JA, Wiggs EA, Solomon BI, et al. The neurogenetics of mucolipidosis type IV. Neurology. 2002;59(3):306-13.
125. Vergarajauregui S, Martina JA, Puertollano R. Identification of the penta-EF-hand protein ALG-2 as a Ca2+-dependent interactor of mucolipin-1. J Biol Chem. 2009;284(52):36357-66.
126. Maki M, Suzuki H, Shibata H. Structure and function of ALG-2, a penta-EF-hand calcium-dependent adaptor protein. Sci China Life Sci. 2011;54(8):770-9.
127. Willett R, Martina JA, Zewe JP, Wills R, Hammond GRV, Puertollano R. TFEB regulates lysosomal positioning by modulating TMEM55B expression and JIP4 recruitment to lysosomes. Nat Commun. 2017;8(1):1580.
128. Maday S, Twelvetrees AE, Moughamian AJ, Holzbaur EL. Axonal transport: cargo-specific mechanisms of motility and regulation. Neuron. 2014;84(2):292-309.
129. Sleigh JN, Rossor AM, Fellows AD, Tosolini AP, Schiavo G. Axonal transport and neurological disease. Nat Rev Neurol. 2019;15(12):691-703.
130. Sheng ZH. The Interplay of Axonal Energy Homeostasis and Mitochondrial Trafficking and Anchoring. Trends Cell Biol. 2017;27(6):403-16.
131. Nixon RA. The aging lysosome: An essential catalyst for late-onset neurodegenerative diseases. Biochim Biophys Acta Proteins Proteom. 2020;1868(9):140443.
132. Winckler B, Faundez V, Maday S, Cai Q, Guimas Almeida C, Zhang H. The Endolysosomal System and Proteostasis: From Development to Degeneration. J Neurosci. 2018;38(44):9364-74.
133. Xiong GJ, Cheng XT, Sun T, Xie Y, Huang N, Li S, et al. Defects in syntabulin-mediated synaptic cargo transport associate with autism-like synaptic dysfunction and social behavioral traits. Mol Psychiatry. 2020.
134. Cai Q, Gerwin C, Sheng ZH. Syntabulin-mediated anterograde transport of mitochondria along neuronal processes. J Cell Biol. 2005;170(6):959-69.
135. Farfel-Becker T, Roney JC, Cheng XT, Li S, Cuddy SR, Sheng ZH. Neuronal Soma-Derived Degradative Lysosomes Are Continuously Delivered to Distal Axons to Maintain Local Degradation Capacity. Cell Rep. 2019;28(1):51-64 e4.
136. Cheng XT, Zhou B, Lin MY, Cai Q, Sheng ZH. Axonal autophagosomes recruit dynein for retrograde transport through fusion with late endosomes. J Cell Biol. 2015;209(3):377-86.
137. Cai Q, Lu L, Tian JH, Zhu YB, Qiao H, Sheng ZH. Snapin-regulated late endosomal transport is critical for efficient autophagy-lysosomal function in neurons. Neuron. 2010;68(1):73-86.

138. Lin MY, Cheng XT, Tammineni P, Xie Y, Zhou B, Cai Q, et al. Releasing Syntaphilin Removes Stressed Mitochondria from Axons Independent of Mitophagy under Pathophysiological Conditions. Neuron. 2017;94(3):595-610 e6.
139. Gowrishankar S, Yuan P, Wu Y, Schrag M, Paradise S, Grutzendler J, et al. Massive accumulation of luminal protease-deficient axonal lysosomes at Alzheimer's disease amyloid plaques. Proc Natl Acad Sci U S A. 2015;112(28):E3699-708.
140. Gowrishankar S, Wu Y, Ferguson SM. Impaired JIP3-dependent axonal lysosome transport promotes amyloid plaque pathology. J Cell Biol. 2017;216(10):3291-305.
141. Yap CC, Digilio L, McMahon LP, Garcia ADR, Winckler B. Degradation of dendritic cargos requires Rab7-dependent transport to somatic lysosomes. J Cell Biol. 2018;217(9):3141-59.
142. Lee S, Sato Y, Nixon RA. Lysosomal proteolysis inhibition selectively disrupts axonal transport of degradative organelles and causes an Alzheimer's-like axonal dystrophy. J Neurosci. 2011;31(21):7817-30.
143. Farias GG, Guardia CM, De Pace R, Britt DJ, Bonifacino JS. BORC/kinesin-1 ensemble drives polarized transport of lysosomes into the axon. Proceedings of the National Academy of Sciences of the United States of America. 2017;114(14):E2955-E64.
144. Jin EJ, Kiral FR, Ozel MN, Burchardt LS, Osterland M, Epstein D, et al. Live Observation of Two Parallel Membrane Degradation Pathways at Axon Terminals. Curr Biol. 2018;28(7):1027-38 e4.
145. Goo MS, Sancho L, Slepak N, Boassa D, Deerinck TJ, Ellisman MH, et al. Activity-dependent trafficking of lysosomes in dendrites and dendritic spines. J Cell Biol. 2017;216(8):2499-513.
146. Padamsey Z, McGuinness L, Bardo SJ, Reinhart M, Tong R, Hedegaard A, et al. Activity-Dependent Exocytosis of Lysosomes Regulates the Structural Plasticity of Dendritic Spines. Neuron. 2017;93(1):132-46.
147. Cheng XT, Xie YX, Zhou B, Huang N, Farfel-Becker T, Sheng ZH. Characterization of LAMP1-labeled nondegradative lysosomal and endocytic compartments in neurons. J Cell Biol. 2018;217(9):3127-39.
148. Burton PR, Paige JL. Polarity of axoplasmic microtubules in the olfactory nerve of the frog. Proc Natl Acad Sci U S A. 1981;78(5):3269-73.
149. Baas PW, Deitch JS, Black MM, Banker GA. Polarity orientation of microtubules in hippocampal neurons: uniformity in the axon and nonuniformity in the dendrite. Proc Natl Acad Sci U S A. 1988;85(21):8335-9.
150. Berg TO, Stromhaug PE, Lovdal T, Seglen PO, Berg T. Use of glycyl-L-phenylalanine 2-naphthylamide, a lysosome-disrupting cathepsin C substrate, to distinguish between lysosomes and prelysosomal endocytic vacuoles. Biochem J. 1994;300(1):229-36.
151. van Bommel B, Konietzny A, Kobler O, Bar J, Mikhaylova M. F-actin patches associated with glutamatergic synapses control positioning of dendritic lysosomes. EMBO J. 2019;38(15):e101183.
152. Schwenk BM, Lang CM, Hogl S, Tahirovic S, Orozco D, Rentzsch K, et al. The FTLD risk factor TMEM106B and MAP6 control dendritic trafficking of lysosomes. The EMBO Journal. 2013:n/a-n/a.
153. Morris RL, Hollenbeck PJ. Axonal transport of mitochondria along microtubules and F-actin in living vertebrate neurons. J Cell Biol. 1995;131(5):1315-26.
154. Overly CC, Lee KD, Berthiaume E, Hollenbeck PJ. Quantitative measurement of intraorganelle pH in the endosomal-lysosomal pathway in neurons by using

ratiometric imaging with pyranine. Proc Natl Acad Sci U S A. 1995;92(8):3156-60.
155. Deinhardt K, Salinas S, Verastegui C, Watson R, Worth D, Hanrahan S, et al. Rab5 and Rab7 control endocytic sorting along the axonal retrograde transport pathway. Neuron. 2006;52(2):293-305.
156. Ferguson SM. Axonal transport and maturation of lysosomes. Curr Opin Neurobiol. 2018;51:45-51.
157. Jahreiss L, Menzies FM, Rubinsztein DC. The itinerary of autophagosomes: from peripheral formation to kiss-and-run fusion with lysosomes. Traffic. 2008;9(4):574-87.
158. Maday S, Wallace KE, Holzbaur EL. Autophagosomes initiate distally and mature during transport toward the cell soma in primary neurons. J Cell Biol. 2012;196(4):407-17.
159. Kimura S, Noda T, Yoshimori T. Dynein-dependent movement of autophagosomes mediates efficient encounters with lysosomes. Cell Struct Funct. 2008;33(1):109-22.
160. Katsumata K, Nishiyama J, Inoue T, Mizushima N, Takeda J, Yuzaki M. Dynein- and activity-dependent retrograde transport of autophagosomes in neuronal axons. Autophagy. 2010;6(3):378-85.
161. Wong YC, Holzbaur EL. The regulation of autophagosome dynamics by huntingtin and HAP1 is disrupted by expression of mutant huntingtin, leading to defective cargo degradation. J Neurosci. 2014;34(4):1293-305.
162. Fu MM, Nirschl JJ, Holzbaur ELF. LC3 binding to the scaffolding protein JIP1 regulates processive dynein-driven transport of autophagosomes. Dev Cell. 2014;29(5):577-90.
163. Stavoe AK, Hill SE, Hall DH, Colon-Ramos DA. KIF1A/UNC-104 Transports ATG-9 to Regulate Neurodevelopment and Autophagy at Synapses. Dev Cell. 2016;38(2):171-85.
164. Neisch AL, Neufeld TP, Hays TS. A STRIPAK complex mediates axonal transport of autophagosomes and dense core vesicles through PP2A regulation. J Cell Biol. 2017;216(2):441-61.
165. Khobrekar NV, Quintremil S, Dantas TJ, Vallee RB. The Dynein Adaptor RILP Controls Neuronal Autophagosome Biogenesis, Transport, and Clearance. Dev Cell. 2020;53(2):141-53 e4.
166. Tresse E, Salomons FA, Vesa J, Bott LC, Kimonis V, Yao TP, et al. VCP/p97 is essential for maturation of ubiquitin-containing autophagosomes and this function is impaired by mutations that cause IBMPFD. Autophagy. 2010;6(2):217-27.
167. Ravikumar B, Acevedo-Arozena A, Imarisio S, Berger Z, Vacher C, O'Kane CJ, et al. Dynein mutations impair autophagic clearance of aggregate-prone proteins. Nat Genet. 2005;37(7):771-6.
168. Hafezparast M, Klocke R, Ruhrberg C, Marquardt A, Ahmad-Annuar A, Bowen S, et al. Mutations in dynein link motor neuron degeneration to defects in retrograde transport. Science. 2003;300(5620):808-12.
169. LaMonte BH, Wallace KE, Holloway BA, Shelly SS, Ascano J, Tokito M, et al. Disruption of dynein/dynactin inhibits axonal transport in motor neurons causing late-onset progressive degeneration. Neuron. 2002;34(5):715-27.
170. Tammineni P, Ye X, Feng T, Aikal D, Cai Q. Impaired retrograde transport of axonal autophagosomes contributes to autophagic stress in Alzheimer's disease neurons. Elife. 2017;6.
171. Di Giovanni J, Sheng ZH. Regulation of synaptic activity by snapin-mediated endolysosomal transport and sorting. EMBO J. 2015;34(15):2059-77.

172. Tammineni P, Jeong YY, Feng T, Aikal D, Cai Q. Impaired axonal retrograde trafficking of the retromer complex augments lysosomal deficits in Alzheimer's disease neurons. Hum Mol Genet. 2017;26(22):4352-66.
173. Drerup CM, Nechiporuk AV. JNK-interacting protein 3 mediates the retrograde transport of activated c-Jun N-terminal kinase and lysosomes. PLoS Genet. 2013;9(2):e1003303.
174. Cavalli V, Kujala P, Klumperman J, Goldstein LS. Sunday Driver links axonal transport to damage signaling. J Cell Biol. 2005;168(5):775-87.
175. Arimoto M, Koushika SP, Choudhary BC, Li C, Matsumoto K, Hisamoto N. The Caenorhabditis elegans JIP3 protein UNC-16 functions as an adaptor to link kinesin-1 with cytoplasmic dynein. J Neurosci. 2011;31(6):2216-24.
176. Bowman AB, Kamal A, Ritchings BW, Philp AV, McGrail M, Gindhart JG, et al. Kinesin-dependent axonal transport is mediated by the sunday driver (SYD) protein. Cell. 2000;103(4):583-94.
177. Huang SH, Duan S, Sun T, Wang J, Zhao L, Geng Z, et al. JIP3 mediates TrkB axonal anterograde transport and enhances BDNF signaling by directly bridging TrkB with kinesin-1. J Neurosci. 2011;31(29):10602-14.
178. Byrd DT, Kawasaki M, Walcoff M, Hisamoto N, Matsumoto K, Jin Y. UNC-16, a JNK-signaling scaffold protein, regulates vesicle transport in C. elegans. Neuron. 2001;32(5):787-800.
179. Verhey KJ, Meyer D, Deehan R, Blenis J, Schnapp BJ, Rapoport TA, et al. Cargo of kinesin identified as JIP scaffolding proteins and associated signaling molecules. J Cell Biol. 2001;152(5):959-70.
180. Fu MM, Holzbaur EL. Integrated regulation of motor-driven organelle transport by scaffolding proteins. Trends Cell Biol. 2014;24(10):564-74.
181. Tanida I, Ueno T, Uchiyama Y. A super-ecliptic, pHluorin-mKate2, tandem fluorescent protein-tagged human LC3 for the monitoring of mammalian autophagy. PLoS One. 2014;9(10):e110600.
182. Snouwaert JN, Church RJ, Jania L, Nguyen M, Wheeler ML, Saintsing A, et al. A Mutation in the Borcs7 Subunit of the Lysosome Regulatory BORC Complex Results in Motor Deficits and Dystrophic Axonopathy in Mice. Cell Rep. 2018;24(5):1254-65.
183. Zheng Q, Ahlawat S, Schaefer A, Mahoney T, Koushika SP, Nonet ML. The vesicle protein SAM-4 regulates the processivity of synaptic vesicle transport. PLoS Genet. 2014;10(10):e1004644.
184. Niwa S, Tao L, Lu SY, Liew GM, Feng W, Nachury MV, et al. BORC Regulates the Axonal Transport of Synaptic Vesicle Precursors by Activating ARL-8. Curr Biol. 2017;27(17):2569-78 e4.
185. De Pace R, Britt DJ, Mercurio J, Foster AM, Djavaherian L, Hoffmann V, et al. Synaptic Vesicle Precursors and Lysosomes Are Transported by Different Mechanisms in the Axon of Mammalian Neurons. Cell Rep. 2020;31(11):107775.
186. Xie Y, Zhou B, Lin MY, Wang S, Foust KD, Sheng ZH. Endolysosomal Deficits Augment Mitochondria Pathology in Spinal Motor Neurons of Asymptomatic fALS Mice. Neuron. 2015;87(2):355-70.
187. Micsenyi MC, Dobrenis K, Stephney G, Pickel J, Vanier MT, Slaugenhaupt SA, et al. Neuropathology of the Mcoln1(-/-) knockout mouse model of mucolipidosis type IV. J Neuropathol Exp Neurol. 2009;68(2):125-35.
188. Beard H, Hassiotis S, Gai WP, Parkinson-Lawrence E, Hopwood JJ, Hemsley KM. Axonal dystrophy in the brain of mice with Sanfilippo syndrome. Exp Neurol. 2017;295:243-55.

189. Zigdon H, Meshcheriakova A, Farfel-Becker T, Volpert G, Sabanay H, Futerman AH. Altered lysosome distribution is an early neuropathological event in neurological forms of Gaucher disease. FEBS Lett. 2017;591(5):774-83.
190. Yang Y, Coleman M, Zhang L, Zheng X, Yue Z. Autophagy in axonal and dendritic degeneration. Trends Neurosci. 2013;36(7):418-28.
191. Tagliaferro P, Burke RE. Retrograde Axonal Degeneration in Parkinson Disease. J Parkinsons Dis. 2016;6(1):1-15.
192. Haidar M, Timmerman V. Autophagy as an Emerging Common Pathomechanism in Inherited Peripheral Neuropathies. Front Mol Neurosci. 2017;10:143.
193. Bordi M, Berg MJ, Mohan PS, Peterhoff CM, Alldred MJ, Che S, et al. Autophagy flux in CA1 neurons of Alzheimer hippocampus: Increased induction overburdens failing lysosomes to propel neuritic dystrophy. Autophagy. 2016;12(12):2467-83.
194. Van Deerlin VM, Sleiman PM, Martinez-Lage M, Chen-Plotkin A, Wang LS, Graff-Radford NR, et al. Common variants at 7p21 are associated with frontotemporal lobar degeneration with TDP-43 inclusions. Nat Genet. 2010;42(3):234-9.
195. Klein ZA, Takahashi H, Ma M, Stagi M, Zhou M, Lam TT, et al. Loss of TMEM106B Ameliorates Lysosomal and Frontotemporal Dementia-Related Phenotypes in Progranulin-Deficient Mice. Neuron. 2017;95(2):281-96 e6.
196. Luningschror P, Werner G, Stroobants S, Kakuta S, Dombert B, Sinske D, et al. The FTLD Risk Factor TMEM106B Regulates the Transport of Lysosomes at the Axon Initial Segment of Motoneurons. Cell Rep. 2020;30(10):3506-19 e6.
197. Nixon RA, Wegiel J, Kumar A, Yu WH, Peterhoff C, Cataldo A, et al. Extensive involvement of autophagy in Alzheimer disease: an immuno-electron microscopy study. J Neuropathol Exp Neurol. 2005;64(2):113-22.
198. Zhang F, Strom AL, Fukada K, Lee S, Hayward LJ, Zhu H. Interaction between familial amyotrophic lateral sclerosis (ALS)-linked SOD1 mutants and the dynein complex. J Biol Chem. 2007;282(22):16691-9.
199. Sharma J, di Ronza A, Lotfi P, Sardiello M. Lysosomes and Brain Health. Annu Rev Neurosci. 2018;41:255-76.
200. Marques ARA, Saftig P. Lysosomal storage disorders - challenges, concepts and avenues for therapy: beyond rare diseases. J Cell Sci. 2019;132(2).
201. Ferguson SM. Neuronal lysosomes. Neurosci Lett. 2019;697:1-9.
202. Brewer GJ, Torricelli JR. Isolation and culture of adult neurons and neurospheres. Nat Protoc. 2007;2(6):1490-8.
203. Klinman E, Holzbaur EL. Comparative analysis of axonal transport markers in primary mammalian neurons. Methods Cell Biol. 2016;131:409-24.
204. Witte MD, Kallemeijn WW, Aten J, Li KY, Strijland A, Donker-Koopman WE, et al. Ultrasensitive in situ visualization of active glucocerebrosidase molecules. Nat Chem Biol. 2010;6(12):907-13.
205. Westbroek W, Nguyen M, Siebert M, Lindstrom T, Burnett RA, Aflaki E, et al. A new glucocerebrosidase-deficient neuronal cell model provides a tool to probe pathophysiology and therapeutics for Gaucher disease. Dis Model Mech. 2016;9(7):769-78.
206. Untergasser A, Cutcutache I, Koressaar T, Ye J, Faircloth BC, Remm M, et al. Primer3--new capabilities and interfaces. Nucleic Acids Res. 2012;40(15):e115.
207. Koressaar T, Remm M. Enhancements and modifications of primer design program Primer3. Bioinformatics. 2007;23(10):1289-91.

208. Kang JS, Tian JH, Pan PY, Zald P, Li C, Deng C, et al. Docking of axonal mitochondria by syntaphilin controls their mobility and affects short-term facilitation. Cell. 2008;132(1):137-48.
209. Taylor AM, Blurton-Jones M, Rhee SW, Cribbs DH, Cotman CW, Jeon NL. A microfluidic culture platform for CNS axonal injury, regeneration and transport. Nat Methods. 2005;2(8):599-605.
210. Zhou B, Yu P, Lin MY, Sun T, Chen Y, Sheng ZH. Facilitation of axon regeneration by enhancing mitochondrial transport and rescuing energy deficits. J Cell Biol. 2016;214(1):103-19.
211. Maday S, Holzbaur EL. Compartment-Specific Regulation of Autophagy in Primary Neurons. J Neurosci. 2016;36(22):5933-45.
212. Boland B, Kumar A, Lee S, Platt FM, Wegiel J, Yu WH, et al. Autophagy induction and autophagosome clearance in neurons: relationship to autophagic pathology in Alzheimer's disease. J Neurosci. 2008;28(27):6926-37.
213. Elrick MJ, Yu T, Chung C, Lieberman AP. Impaired proteolysis underlies autophagic dysfunction in Niemann-Pick type C disease. Hum Mol Genet. 2012;21(22):4876-87.
214. Maetzel D, Sarkar S, Wang H, Abi-Mosleh L, Xu P, Cheng AW, et al. Genetic and chemical correction of cholesterol accumulation and impaired autophagy in hepatic and neural cells derived from Niemann-Pick Type C patient-specific iPS cells. Stem Cell Reports. 2014;2(6):866-80.
215. Ko DC, Milenkovic L, Beier SM, Manuel H, Buchanan J, Scott MP. Cell-autonomous death of cerebellar purkinje neurons with autophagy in Niemann-Pick type C disease. PLoS Genet. 2005;1(1):81-95.
216. Boland B, Smith DA, Mooney D, Jung SS, Walsh DM, Platt FM. Macroautophagy is not directly involved in the metabolism of amyloid precursor protein. J Biol Chem. 2010;285(48):37415-26.
217. Gurda BL, Bagel JH, Fisher SJ, Schultz ML, Lieberman AP, Hand P, et al. LC3 Immunostaining in the Inferior Olivary Nuclei of Cats With Niemann-Pick Disease Type C1 Is Associated With Patterned Purkinje Cell Loss. J Neuropathol Exp Neurol. 2018;77(3):229-45.
218. Ganley IG, Pfeffer SR. Cholesterol accumulation sequesters Rab9 and disrupts late endosome function in NPC1-deficient cells. J Biol Chem. 2006;281(26):17890-9.
219. Lebrand C, Corti M, Goodson H, Cosson P, Cavalli V, Mayran N, et al. Late endosome motility depends on lipids via the small GTPase Rab7. EMBO J. 2002;21(6):1289-300.
220. Winkler MBL, Kidmose RT, Szomek M, Thaysen K, Rawson S, Muench SP, et al. Structural Insight into Eukaryotic Sterol Transport through Niemann-Pick Type C Proteins. Cell. 2019;179(2):485-97 e18.
221. Lim CY, Davis OB, Shin HR, Zhang J, Berdan CA, Jiang X, et al. ER-lysosome contacts enable cholesterol sensing by mTORC1 and drive aberrant growth signalling in Niemann-Pick type C. Nat Cell Biol. 2019;21(10):1206-18.
222. Wilhelm LP, Wendling C, Vedie B, Kobayashi T, Chenard MP, Tomasetto C, et al. STARD3 mediates endoplasmic reticulum-to-endosome cholesterol transport at membrane contact sites. EMBO J. 2017;36(10):1412-33.
223. Bilgin M, Nylandsted J, Jaattela M, Maeda K. Quantitative Profiling of Lysosomal Lipidome by Shotgun Lipidomics. Methods Mol Biol. 2017;1594:19-34.
224. Diettrich O, Mills K, Johnson AW, Hasilik A, Winchester BG. Application of magnetic chromatography to the isolation of lysosomes from fibroblasts of patients with lysosomal storage disorders. FEBS Lett. 1998;441(3):369-72.

225. Bolte S, Cordelieres FP. A guided tour into subcellular colocalization analysis in light microscopy. J Microsc. 2006;224(Pt 3):213-32.
226. Cabukusta B, Neefjes J. Mechanisms of lysosomal positioning and movement. Traffic. 2018;19(10):761-9.
227. Maekawa M, Fairn GD. Complementary probes reveal that phosphatidylserine is required for the proper transbilayer distribution of cholesterol. J Cell Sci. 2015;128(7):1422-33.
228. Ohno-Iwashita Y, Shimada Y, Waheed AA, Hayashi M, Inomata M, Nakamura M, et al. Perfringolysin O, a cholesterol-binding cytolysin, as a probe for lipid rafts. Anaerobe. 2004;10(2):125-34.
229. Zidovetzki R, Levitan I. Use of cyclodextrins to manipulate plasma membrane cholesterol content: evidence, misconceptions and control strategies. Biochim Biophys Acta. 2007;1768(6):1311-24.
230. Kilsdonk EP, Yancey PG, Stoudt GW, Bangerter FW, Johnson WJ, Phillips MC, et al. Cellular cholesterol efflux mediated by cyclodextrins. J Biol Chem. 1995;270(29):17250-6.
231. Ohvo H, Slotte JP. Cyclodextrin-mediated removal of sterols from monolayers: effects of sterol structure and phospholipids on desorption rate. Biochemistry. 1996;35(24):8018-24.
232. Davidson CD, Ali NF, Micsenyi MC, Stephney G, Renault S, Dobrenis K, et al. Chronic cyclodextrin treatment of murine Niemann-Pick C disease ameliorates neuronal cholesterol and glycosphingolipid storage and disease progression. PLoS One. 2009;4(9):e6951.
233. Liu B, Li H, Repa JJ, Turley SD, Dietschy JM. Genetic variations and treatments that affect the lifespan of the NPC1 mouse. J Lipid Res. 2008;49(3):663-9.
234. Liu B, Turley SD, Burns DK, Miller AM, Repa JJ, Dietschy JM. Reversal of defective lysosomal transport in NPC disease ameliorates liver dysfunction and neurodegeneration in the npc1-/- mouse. Proc Natl Acad Sci U S A. 2009;106(7):2377-82.
235. Ory DS, Ottinger EA, Farhat NY, King KA, Jiang X, Weissfeld L, et al. Intrathecal 2-hydroxypropyl-beta-cyclodextrin decreases neurological disease progression in Niemann-Pick disease, type C1: a non-randomised, open-label, phase 1-2 trial. Lancet. 2017;390(10104):1758-68.
236. Fraldi A, Annunziata F, Lombardi A, Kaiser HJ, Medina DL, Spampanato C, et al. Lysosomal fusion and SNARE function are impaired by cholesterol accumulation in lysosomal storage disorders. EMBO J. 2010;29(21):3607-20.
237. Hoque S, Kondo Y, Sakata N, Yamada Y, Fukaura M, Higashi T, et al. Differential Effects of 2-Hydroxypropyl-Cyclodextrins on Lipid Accumulation in Npc1-Null Cells. Int J Mol Sci. 2020;21(3).
238. Chen FW, Li C, Ioannou YA. Cyclodextrin induces calcium-dependent lysosomal exocytosis. PLoS One. 2010;5(11):e15054.
239. Elson EL, Fried E, Dolbow JE, Genin GM. Phase separation in biological membranes: integration of theory and experiment. Annu Rev Biophys. 2010;39:207-26.
240. Mukherjee S, Maxfield FR. Membrane domains. Annu Rev Cell Dev Biol. 2004;20:839-66.
241. Epand RM. Cholesterol and the interaction of proteins with membrane domains. Prog Lipid Res. 2006;45(4):279-94.
242. Ge Y, Gao J, Jordan R, Naumann CA. Changes in Cholesterol Level Alter Integrin Sequestration in Raft-Mimicking Lipid Mixtures. Biophys J. 2018;114(1):158-67.

243. Rahbek-Clemmensen T, Lycas MD, Erlendsson S, Eriksen J, Apuschkin M, Vilhardt F, et al. Super-resolution microscopy reveals functional organization of dopamine transporters into cholesterol and neuronal activity-dependent nanodomains. Nat Commun. 2017;8(1):740.
244. Peake KB, Vance JE. Normalization of cholesterol homeostasis by 2-hydroxypropyl-beta-cyclodextrin in neurons and glia from Niemann-Pick C1 (NPC1)-deficient mice. J Biol Chem. 2012;287(12):9290-8.
245. Yang DS, Stavrides P, Kumar A, Jiang Y, Mohan PS, Ohno M, et al. Cyclodextrin has conflicting actions on autophagy flux in vivo in brains of normal and Alzheimer model mice. Hum Mol Genet. 2017;26(5):843-59.
246. Nixon RA. The role of autophagy in neurodegenerative disease. Nat Med. 2013;19(8):983-97.
247. Maday S, Holzbaur EL. Autophagosome biogenesis in primary neurons follows an ordered and spatially regulated pathway. Dev Cell. 2014;30(1):71-85.
248. Stavoe AKH, Holzbaur ELF. Autophagy in Neurons. Annu Rev Cell Dev Biol. 2019;35:477-500.
249. Stavoe AKH, Holzbaur ELF. Axonal autophagy: Mini-review for autophagy in the CNS. Neurosci Lett. 2019;697:17-23.
250. Rosa-Ferreira C, Sweeney ST, Munro S. The small G protein Arl8 contributes to lysosomal function and long-range axonal transport in Drosophila. Biol Open. 2018;7(9).
251. Jia R, Guardia CM, Pu J, Chen Y, Bonifacino JS. BORC coordinates encounter and fusion of lysosomes with autophagosomes. Autophagy. 2017;13(10):1648-63.
252. Harayama T, Riezman H. Understanding the diversity of membrane lipid composition. Nat Rev Mol Cell Biol. 2018;19(5):281-96.
253. Casares D, Escriba PV, Rossello CA. Membrane Lipid Composition: Effect on Membrane and Organelle Structure, Function and Compartmentalization and Therapeutic Avenues. Int J Mol Sci. 2019;20(9).